



**University of
Nottingham**
UK | CHINA | MALAYSIA

Advance Control of a Synchronous Reluctance Motor Drive

Thesis submitted to the University of Nottingham for the degree of
Doctor of Philosophy, November 2022.

Jacopo Riccio

Your ID: 20129526

Supervised by

Pericle Zanchetta

Signature:

Date April 15, 2023

Acknowledgements

This PhD has been one of the most exciting experiences of my life. I had the chance to expand my knowledge towards the electrical engineering world, which has been quite challenging because of coming from a completely different background (i.e., mechanical engineering). I was fortunate to have joined the PEMC research group, and I wish to express my gratitude towards Pericle Zanchetta for the chance he gave me to pursue this PhD awareness goal and for believing in me since the period of my master's thesis. I wish to thank Shafiq Odhano for his outstanding professionalism and caring supervision. I learned loads of content from one of the best in the field, and, most of all, a solid method around which I built my skills. Unfortunately, about one year after the start of my PhD, the Covid-19 pandemic started affecting everyone's life with unprecedented challenges and my research activity continued in a worldwide lockdown drastically limiting social life and affecting everyday life's routines. In this scenario, I also want to thank Mauro Di Nardo for stepping into my supervision team and for the professional, sincere and straightforward advice he started giving me during the work-from-home period. His sympathy and experience made such a weird working period pleasant and with useful outcomes. I am very thankful to Petros Karamanakos for his support, the valuable feedback throughout this thesis, and for contributing significantly to my professional and technical growth.

I am also deeply grateful to have met extraordinary people like Antonio and Andrea for making my life in Nottingham extremely pleasant and entertaining.

A huge thank you is also to my girlfriend Francesca for her unwavering support, encouragement, and motivation throughout my academic journey.

Finally, I would like to express my heartfelt appreciation to my parents and my family for their unconditional love, support, and sacrifice throughout

my life. Their unwavering encouragement, guidance, and belief in me have been the foundation of my academic success. This life experience would not have been possible without their support.

List of Publications

1. J. Riccio, P. Karamanakos, S. Odhano, M. Tang, M. D. Nardo and P. Zanchetta, "Direct Model Predictive Control of Synchronous Reluctance Motor Drives," in IEEE Transactions on Industry Applications, 2022, doi: 10.1109/TIA.2022.3213002.
2. J. Riccio, P. Karamanakos, S. Odhano, M. Tang, M. D. Nardo, G. Tresca and P. Zanchetta, "Modulated Model-Predictive Integral Control applied to a Synchronous Reluctance Motor Drive," in IEEE Journal of Emerging and Selected Topics in Power Electronics, doi: 10.1109/JESTPE.2023.3245077.
3. J. Riccio, P. Karamanakos, S. Odhano, M. Tang, M. D. Nardo and P. Zanchetta, "A Direct Model Predictive Control Strategy for High-Performance Synchronous Reluctance Motor Drives," 2021 IEEE Energy Conversion Congress and Exposition (ECCE), 2021, pp. 4704-4710, doi: 10.1109/ECCE47101.2021.9595334.
4. S. R. Di Salvo, M. Bulzi, J. Riccio, R. Leuzzi, P. Zanchetta and N. Anglani, "Model predictive Control of a Double Stage AC-DC Converter for Grid-Interface of Vanadium Flow Batteries," 2021 IEEE Energy Conversion Congress and Exposition (ECCE), 2021, pp. 1895-1901, doi: 10.1109/ECCE47101.2021.9595483.
5. J. Riccio, S. Odhano, M. Tang and P. Zanchetta, "Sensorless Cascaded-Model Predictive Control applied to a Doubly Fed Induction Ma-

- chine,” 2020 IEEE Energy Conversion Congress and Exposition (ECCE), 2020, pp. 3842-3848, doi: 10.1109/ECCE44975.2020.9236318.
6. J. Riccio, S. A. Odhano and P. Zanchetta, ”Sensorless and Modulated Model-Predictive Control for a Doubly Fed Induction Machine,” 2019 21st European Conference on Power Electronics and Applications (EPE '19 ECCE Europe), 2019, pp. P.1-P.10, doi: 10.23919/EPE.2019.8915159.
 7. Jacopo Riccio, Rahul Ranjeev Kumar Kumar, Giansalvo Cirrincione, Maurizio Cirrincione, and Pericle Zanchetta. Fault diagnosis using shallow neural networks for voltage source inverters in synrm drives. In 2022 IEEE Energy Conversion Congress and Exposition (ECCE), 2022.
 8. Jacopo Riccio, Rahul Luca Rovere, Mauro Di Nardo, Shafiq Odhano, and Pericle Zanchetta. Model-predictive control of open-end winding synchronous reluctance drives. In 2022 IEEE Energy Conversion Congress and Exposition (ECCE), 2022.

Contents

Acknowledgements	i
List of Tables	viii
List of Figures	ix
Abbreviations	xviii
Abstract	1
Chapter 1 Motivations and Contributions	3
1.1 First Research Question	4
1.2 Second Research Question	6
Chapter 2 Theoretical Background	8
2.1 Introduction	8
2.2 Magnetic Model Identification Procedures	11
2.2.1 Online Parameters Identification Procedures	12
2.2.2 Offline Parameters Identification Procedures	14
2.3 SyRel Control Techniques: State of the Art	19
2.3.1 Field-oriented Control	21
2.3.2 Direct Torque Control	23
2.3.3 Model Predictive Control	24
2.3.3.1 Finite-Control-Set Model-Predictive Control	25
2.3.3.2 Modulated Model Predictive Control	28
2.3.4 Other Control Techniques on SyRel Motor Drives	30
2.3.4.1 Model-Free Control	30
2.3.4.2 Deviation Model-Based Control	31
2.3.4.3 Sliding Mode Control Technique	32

2.3.4.4	Artificial Intelligence Control Techniques . . .	32
Chapter 3	SyRel Drive Modelling	34
3.1	Two-Level Voltage Source Inverter	34
3.1.1	Modulation Stage: Sinusoidal Pulse-Width Modulation	37
3.1.2	Modulation Stage: Third Harmonic Injection	41
3.1.3	Inverter Non-Linearities	42
3.2	SyRel Motor: Linear Model	43
3.3	Magnetic Model Identification Tests	46
3.4	SyRel Motor: Real Model	50
3.4.1	Inductance Calculation	50
3.4.2	Maximum Torque Per Ampere Trajectory	55
3.5	Chapter Conclusions	57
Chapter 4	FCS-MPC: Case Study	59
4.1	FCS-MPC Design Parameters	60
4.2	Predictions	62
4.3	Cost Function	63
4.3.1	Current Tracking Terms	64
4.3.2	Integral Terms Inclusion	67
4.3.3	Control Effort Inclusion	69
4.3.4	Prediction Saturation	72
4.4	Chapter Conclusions	72
Chapter 5	FCS-MPC: Simulation and Experimental Re-	
	sults	73
5.1	FCS-MPC Simulation Results	76
5.1.0.1	Switching Frequency Calculation	77
5.1.0.2	Integral Terms Inclusion and Robustness Anal-	
	ysis	82
5.1.0.3	Control Effort Weighting Factor Variation	86

5.1.0.4	Current Variations	90
5.1.0.5	Speed Variations	91
5.2	Experimental Results	92
5.2.1	Integral Terms Assessment	93
5.2.2	Control Effort Assessment	97
5.2.2.1	Tests at rated current	97
5.2.2.2	Tests at 20% of the Rated Current	99
5.2.3	Tests over the entire d-q current plane	100
5.2.4	Tests at different speeds	101
5.2.5	Tests at MTPA conditions	102
5.3	Chapter Conclusions	103
Chapter 6	SyRel Drive: Modulated-Model Predictive Control	105
6.1	Evaluation Function	107
6.2	Duty Cycle Calculation	111
6.2.0.1	Steady-state Operation	111
6.2.0.2	Transient Operation	117
6.3	Chapter Conclusions	121
Chapter 7	M-MPC Results	123
7.1	Simulation Results	123
7.1.1	Current Control at constant speed	124
7.2	Experimental Results	127
7.2.1	Linear Modulation: Test 1	128
7.2.2	Linear Modulation: Test 2	131
7.2.3	Overmodulation: Test 3	133
7.2.4	Linear Modulation: Test 4	135
7.2.5	Integrals inclusion and Robustness Analysis	138
7.3	Chapter Conclusions	142

Chapter 8	Conclusions	143
Appendices		147
Chapter A	Experimental Setup	148
A.1	Prime Mover Control	150
A.2	SyRel FOC	151
Bibliography		153

List of Tables

3.1	Switching states of the 2L-VSI.	37
4.1	Control effort list of values for each configuration change. . .	71
A.1	SyRel motor nameplate.	152

List of Figures

2.1	Different types of rotor topologies [1].	9
2.2	Classification of parameters identification procedures applicable to SyRel motor drives.	12
2.3	FOC block diagram.	21
2.4	DTC block diagram.	24
2.5	FCS-MPC block diagram.	27
2.6	M-MPC block diagram.	29
3.1	2L-VSI circuit.	35
3.2	Feasible configurations of a 2L-VSI	35
3.3	2L-VSI switching states.	37
3.4	Modulation index.	39
3.5	S-PWM.	40
3.6	41
3.7	Third harmonic injection scheme.	41
3.8	Dead-time on the leg a	42
3.9	SyRel vector diagram.	44
3.10	SyRel ideal equivalent circuit representation.	45
3.11	L_d and L_q estimation ($L_d = 186.4$ mH, $L_q = 32$ mH).	46
3.12	Experimental test for $i_d = 7$ A, $i_q = 7$ A.	49
3.13	Identified magnetic model.	50
3.14	(a) Evaluated MTPW trajectory in the ψ_d, ψ_q plane. (b) Evaluated MTPW trajectory in the ψ_d, ψ_q plane.	51

3.15	Identified magnetic model.	54
3.16	Identified magnetic model.	54
3.17	Evaluated 3D torque surface.	56
3.18	Evaluated MTPA trajectory in the (a) i_d, i_q plane and (b) $ i_{dq} , T_{em}$ plane.	56
3.19	Evaluated MTPA trajectory in the (a) $\angle i_{dq}, i_{dq} $ plane and (b) $\angle i_{dq}, T_{em}$ plane.	57
4.1	Definition of the control and prediction horizon taken from [2].	61
4.2	Cost function graphical interpretation.	64
5.1	Block diagram of FCS-MPC for a SyRel Motor drive.	74
5.2	FCS-MPC dynamic performance comparison ($f_s = 48$ kHz, $\omega_r = 400$ rpm, $V_{dc} = 300$ V)(a) d -current tracking. (b) q -current tracking.	77
5.3	Switching frequency calculation. (a) Switching frequency. (b) a -phase current tracking. (c) Switching state. (d) b -phase current tracking. (e) Optimum vector. (f) c -phase current tracking.	78
5.4	TDD _{<i>i</i>} versus \bar{f}_{sw} trend for $T_{em} = 14$ Nm MTPA.	80
5.5	(a) dq -current tracking transient response at $f_s = 25$ kHz. (b) dq -current tracking transient response at $f_s = 50$ kHz. (c) dq -current tracking at $f_s = 25$ kHz. (d) dq -current tracking at $f_s = 50$ kHz. (e) abc -current tracking at $f_s = 25$ kHz. (f) abc -current tracking at $f_s = 50$ kHz. (g) Harmonic spectra at $f_s = 25$ kHz (h) Harmonic spectra at $f_s = 50$ kHz . . .	81

5.6	Effects of the flux vector variations on (a) d -current tracking during transient, (b) q -current tracking during transient, (c) d -current tracking at steady-state, (d) integral of the d -current tracking over time, (e) q -current tracking at steady-state, and (f) integral of the q -current tracking over time, (g) a -current tracking for the three cases, and (h) the corresponding harmonic spectra.	84
5.7	Effects of the flux vector variations on (a) d -axis current step response curve, (b) q -axis current step response curve, (c) integral of the d -current tracking over time, (d) integral of the q -current tracking over time, (e) a -phase current tracking, and (f) the corresponding harmonic spectra.	85
5.8	Trade-off curve between TDD_i and switching frequency at various λ_u and full-load ($i_d = i_q = 5.5$ A; $\omega_m = 1500$ rpm, $0 < \lambda_u < 0.056$).	87
5.9	(a) dq -current reference tracking ($f_s = 40$ kHz, $\bar{f}_{sw} \approx 4020$ Hz, and $\lambda_u = 0.0384$). (b) dq -current reference tracking transients. (c) b -, c -phase currents reference tracking. (d) b -, c -phase current harmonic spectra.	87
5.10	Comparative analysis between the FCS-MPC and the PI-based FOC control method.	88
5.11	Comparative analysis of FCS-MPC versus PI-based FOC control at $\bar{f}_{sw} = 8.2$ kHz (a) d -current reference tracking. (b) q -current reference tracking. (c) Phase current reference tracking achieved by the FCS-MPC. (d) Phase current reference tracking achieved by the PI-based FOC control. (e) a -phase current harmonic spectra comparison.	89
5.12	Steady-state performance variations due to changing the current command.	90

5.13	(a) dq -current reference tracking ($f_s = 40$ kHz, $\bar{f}_{sw} \approx 4020$ Hz, and $\lambda_u = 0.0384$). (b) dq -current reference tracking transients. (c) b -, c -phase currents reference tracking. (d) b -, c -phase current harmonic spectra.	92
5.14	(a) d -current tracking with and without integral (b) q -current tracking with and without integral. (c) Numerical integration of the d -current error over time with and without integral. (d) Numerical integration of the q -current error over time with and without integral.	93
5.15	Assessment of the effectiveness of the integrating action of the proposed FCS-MPC scheme and its comparison with the method described in [3].	97
5.16	Trade-off curve between TDD_i and switching frequency ($i_d = i_q = 5.5$ A; $\omega_m = 100$ rpm, $0 < \lambda_u < 0.032$).	98
5.17	(a) dq -current reference tracking ($f_s = 48$ kHz, $\bar{f}_{sw} \approx 3.2$ kHz, and $\lambda_u = 0.0160$). (b) dq -current reference tracking transients. (c) b -, c -phase currents reference tracking. (d) b -, c -phase current harmonic spectra.	98
5.18	Trade-off curve between TDD_i and switching frequency at various λ_u ($i_d = i_q = 1.1$ A; $\omega_m = 400$ rpm, $0 < \lambda_u < 0.08$).	99
5.19	(a) dq -current reference tracking ($f_s = 24$ kHz, $\bar{f}_{sw} \approx 2$ kHz, and $\lambda_u = 0.0160$). (b) dq -current reference tracking transients. (c) a -, b -, c -phase currents reference tracking. (d) b -, c -phase current harmonic spectra.	100
5.20	(a) Overall steady-state performance over the current domain given $\omega_m = 100$ rpm, $f_s = 48$ kHz, $\lambda_u = 0$. (b) Overall steady-state performance over the current domain for $\omega_m = 100$ rpm, $f_s = 48$ kHz, $\lambda_u = 0.016$	101

5.21	(a) TDD_i and \bar{f}_{sw} trends with respect to the speed for a fixed $\lambda_u = 0$. (b) TDD_i and \bar{f}_{sw} trends with respect to the speed for a fixed $\lambda_u = 0.016$	102
5.22	TDD_i and switching frequency trade-off for two torque references ($\omega_m = 100$ rpm, $0 < \lambda_u < 0.032$).	103
6.1	Block diagram of M-MPC for SyRel motor drive.	108
6.2	Optimum vector selection by means of (a) the proposed M-MPC (b) and [4].	110
6.3	(a) Evaluation function g_d, g_q coordinates for the feasible configurations of a 2L-VSI during steady state operation; (b) duty cycle representation.	113
6.4	(a) Evaluation function g_d, g_q coordinates for the feasible configurations of a 2L-VSI during steady state operation; (b) duty cycle representation.	115
6.5	Distance from voltage actuation to the target at steady state.	116
6.6	Evolution of (6.6) over time.	116
6.7	Optimum voltage vector selected.	116
6.8	(a) Evaluation function g_d, g_q coordinates for the feasible configurations of a 2L-VSI during transient; (b) duty cycle representation.	117
6.9	(a) Evaluation function g_d, g_q coordinates for the feasible configurations of a 2L-VSI during steady state operation; (b) duty cycle representation.	119
6.10	Distance from voltage actuation to the target during transient.	121
6.11	Evolution of (6.6) over time.	121
6.12	Optimum voltage vector selected.	121
6.13	Turnaround time of the M-MPC implementation.	121
6.14	M-MPC flowchart.	122

7.1	Simulation results of the d - q -current step response. (a) d -current tracking. (b) q -current tracking.	124
7.2	Duty cycles trend over time. (a) Transient operation. (b) Steady-state operation.	125
7.3	Target trend over time during transient. (a) d -component target. (b) q -component target.	125
7.4	Hexagon evolution over time during transient.	126
7.5	M-MPC Simulation results. (a) d -current predictions for each feasible voltage vector. (b) q -current predictions for each feasible voltage vector. (c) Phase-voltages. (d) Rotational speed.	127
7.6	Experimental results of the d -, q -current step response at 900 rpm. (a) d -current step response M-MPC versus PI. (b) q -current step response M-MPC versus PI. (c) Rotational speed transient. (d) Line-to-line computed voltages.	129
7.7	Duty cycles trend over time. (a) Transient operation. (b) Steady-state operation. (c) Optimum vectors selection during transient. (d) Optimum vectors selection during steady state.	130
7.8	(a) M-MPC a -, b -, c -phase measures at 900 rpm. (b) b - c -phase currents harmonic spectra M-MPC (THD= 0.57%). (c) b - c -phase currents harmonic spectra PI (THD= 1.48%).	131
7.9	Experimental results of the d -, q -current step response at 300 rpm. (a) d -current step response M-MPC versus PI. (b) q -current step response M-MPC versus PI.	132
7.10	(a) M-MPC, b -, c -phase measures at 300 rpm. (b) a -, b -, c -phase currents harmonic spectra M-MPC (THD= 0.30%). (c) a -, b -, c -phase currents harmonic spectra PI (THD= 0.65%).	132

7.11	Overmodulation test results. (a) <i>abc</i> -current tracking. (b) <i>abc</i> -current harmonic spectra. (c) Voltage actuation hexagon. (d) Target coordinates evolution over time.	133
7.12	Experimental results of the <i>d</i> - <i>q</i> -current behavior in overmodulation with the proposed M-MPC method. (a) <i>d</i> -current tracking. (b) <i>q</i> -current tracking.	134
7.13	Experimental results with deadbeat control in linear modulation region. (a) <i>dq</i> -current tracking. (b) <i>abc</i> -reference voltage.	135
7.14	Experimental results with FOC control in linear modulation region. (a) <i>dq</i> -current tracking. (b) <i>abc</i> -reference voltage. . .	136
7.15	Experimental results with the proposed M-MPC method. (a) <i>abc</i> -current tracking. (b) <i>abc</i> -current harmonic spectra. (c) <i>abc</i> -reference voltage. (d) <i>dq</i> -current tracking reference. .	137
7.16	Experimental results. (a) deadbeat <i>abc</i> -current tracking. (b) deadbeat <i>abc</i> -current harmonic spectra. (c) deadbeat <i>abc</i> -reference voltage. (d) deadbeat <i>dq</i> -current tracking reference.	138
7.17	(a) FOC <i>abc</i> -current tracking. (b) FOC <i>abc</i> -current harmonic spectra. (c) FOC <i>abc</i> -reference voltage. (d) FOC <i>dq</i> -current tracking reference.	139
7.18	Dynamic current errors' correction for 50% overestimated magnetic flux for various correction weights' pair. (a) <i>d</i> -current component. (b) <i>q</i> -current component.	140
7.19	Steady-state errors with a 50% overestimated magnetic flux. (a) <i>d</i> -axis current error. (b) <i>q</i> -axis current error.	141
A.1	Test bench configuration.	149
A.2	Ucube control Platform.	149

A.3	PM speed control scheme.	150
A.4	Rotor-oriented FOC block diagram for SyRel motor.	152

Abbreviations

- 2L-VSI** Two-Level Voltage Source Inverter.
- ADC** analogue-to-digital-converters.
- ANN** Artificial Neural Network.
- ARFNN** Adaptive Recurrent Fuzzy Neural Network.
- ARX** auto-regressive exogenous.
- CCS-MPC** Continuous Control Set Model Predictive Control.
- DFVC** Direct-Flux Vector Control.
- DMBC** Deviation Model-Based Control.
- DSP** Digital Signal Processing.
- DTC** Direct Torque Control.
- EKF** Extended Kalman Filter.
- FCS-MPC** Finite Control Set Model Predictive Control.
- FL** Fuzzy Logic.
- FOC** Field-Oriented Control.
- FPGA** Field Programmable Gate Array.
- HF** High Frequency.
- IE** Incremental Encoder.
- IM** Induction Motor.
- LMS** Least Mean Square.
- LPF** Low-Pass Filter.
- LUT** Look-up Table.

M-MPC Dead beat current control.

M-MPC Modulated Model-Predictive Control.

MPC model predictive control.

MTPA Maximum Torque per Ampere.

MTPV Maximum Torque per Voltage.

MTPW Maximum Torque per Weber.

PI Proportional-Integral.

PM Permanent Magnet.

PMSM Permanent Magnet Synchronous Machine.

RLS Recursive Least Square.

SiC Silicone-Carbide.

SMC sliding mode control.

S-PWM Sinusoidal Pulse-Width Modulation.

SoC system-on-chip.

SyRel Synchronous Reluctance.

TDD Total Demand Distortion.

THD Total Harmonic Distortion.

ULM Ultra-local Modeling.

VFD Variable Frequency Drive.

Abstract

This thesis investigates two predictive control algorithms designed to enhance the performance of a synchronous reluctance motor drive. In particular, a finite-control set solution approach has been followed. In particular, this thesis proposes the inclusion of integral terms into the cost function to ensure zero steady-state errors thus compensating for any model inaccuracy. In addition, a control effort term is also considered in the online optimization definition to achieve a quasi-continuous time digital controller given the high achievable ratio between the sampling frequency and the average switching frequency. After a comprehensive simulation study showing the advantages of the proposed approach over the conventional predictive controller solution over a wide range of operating conditions, several experimental test results are reported. The effectiveness of the proposed control approach, including a detailed analysis of the effect of the load and speed variations, is thus fully verified providing useful guidelines for the design of a direct model predictive controller of synchronous reluctance motor drives.

In addition, this thesis investigates an innovative duty cycle calculation method for a continuous-control set model predictive control. The formulation of the duty cycles, as well as the introduction of integral terms, enable good reference tracking performance with zero steady-state error at fixed switching frequency over the whole current operating range. Low

current ripple with smooth and fast dynamics are achievable, making the proposed control algorithm suitable as a valid alternative in synchronous reluctance motor drives over the established control methods. Simulations and experimental results show the effectiveness and the advantages of the proposed control algorithm over the benchmark.

Chapter 1

Motivations and Contributions

Nowadays SyRel motors are widely used in numerous applications such as industrial drives, traction applications, aerospace, etc. SyRel motor drives present economical advantages over other motor topologies. The rotor structure is an iron core shaped such that the reluctance phenomenon, whose working principle of the SyRel is based on, is maximized. Despite this advantage, the system complexity increases, and subsequently the control design is not trivial. This thesis aims at tackling the difficulty to design a controller of such an intricate motor drive.

In particular, the method that has been widely established as a benchmark for the system under investigation is the Field-Oriented Control (FOC) method. Given the non-linear nature of the SyRel motor, this technique requires the flux-versus-current maps to tune the controller gains in the whole operating area. The model predictive control (MPC) approach is investigated in this thesis to bypass the tuning procedure acknowledging the non-linear nature of the MPC. In addition, further advancement will be studied to reduce the torque ripple and augment the robustness of the system against parameter variations.

1.1 First Research Question

The first goal is to define a controller capable of guaranteeing the same dynamic performance in the whole operating region without a complex tuning procedure. Furthermore, the controller has to be robust over parameter mismatches and perform better than standard solutions.

The main difficulty resides in the non-linear magnetic characteristics of SyRel motors. Standard proportional-integral-based controllers vary the system's performance according to the operating point. Accurate magnetic model identification procedures are necessary to design the controller and guarantee the same stability margins and performance in the entire operating region. Each analyzed operating point is characterized by a unique pair of proportional and integral gains whose values need to be calculated and stored for the hardware implementation. This concept is known as gain scheduling, and it requires a significant portion of the available memory as well as time-consuming controller designing procedures. The identification procedures are essential when linear controllers are considered with non-linear plants such as the SyRel motor. Another fundamental aspect necessary to run FOC algorithms is the requirement of high-computational devices to implement the sinusoidal pulse-width modulation aimed at generating the control command in motor drive applications. Such difficulty is typically addressed by employing powerful system-on-chip system-on-chip (SoC) solutions augmenting the complexity of the system.

To guarantee consistent performance over the whole operating region without the need for complex tuning procedures, non-linear controllers such as the Finite Control Set Model Predictive Control (FCS-MPC) are more suitable for the case study. The system identification is still required though because the FCS-MPC is a model-based controller. The identified mag-

netic characteristics can be included in the implementation to guarantee accurate reference tracking with no performance variation when varying the operating point.

Typically, standard FCS-MPCs are not robust to parameter variations. Poor steady-state performance is observable when the model has not been accurately identified. Thus to improve the system's robustness, an integral of the error term has been introduced in this work. Even though the considered system is highly non-linear, the integral of the error gains can be easily tuned regardless of the operating point. The computational complexity introduced due to the integral terms included did not increase the computational overhead compared to other approaches found in the literature. The associated computational cost resulted as less demanding than other existing solutions in literature, mainly based on the augmented state of the systems.

Standard FCS-MPCs are prone to a low sampling-to-switching frequency ratio leading to a coarsely sampled time axis. The introduction of the control effort in the online optimization problem enables higher granularity of switching operations and, consequently, more favorable steady-state performance. When low sampling frequencies are used, then low granularity of switching results. If a low-cost microprocessor is used—which does not have sufficient computational resources—then such an inferior performance can result. This typically leads to inferior steady-state and transient performance. If, on the other hand, more powerful microprocessors are used, or an Field Programmable Gate Array (FPGA), or a system-on-chip solution (as in this work) to undertake all the implementation tasks, then a higher sampling frequency can be used. This increases the granularity of switching and thus the system performance. As the cost of microprocessors decreases and the available computational power increases, the potential of

more computationally demanding control methods, such as the FCS-MPC proposed in this work, will be fully harvested.

1.2 Second Research Question

A further investigation was carried out on the same SyRel motor drive aimed at identifying a predictive controller featuring a constant switching frequency, capable to operate in the overmodulation region without losing the reference tracking, and robust to parameter mismatch.

FCS-MPC algorithms are prone to non-constant switching patterns. This aspect is not desirable when output filters have to be included and designed. To this end, a M-MPC, was considered. The control approach followed the geometric criteria inherently applicable for the considered configuration (i.e., a SyRel driven by a 2L-VSI) to facilitate a greater controller design simplicity by avoiding the use of weighting factors. The classical formulation of the cost function does not allow for such flexibility unless additional hard and soft constraints are included in the optimization problem.

Furthermore, the designed controller can achieve enhance reference tracking performance than standard controllers such as PI-based FOC and deadbeat control techniques in the overmodulation region. That has been achieved thanks to a self-saturation mechanism based on the closest achievable target that enables the full utilization of the dc-link. In addition, the system's robustness against parameter variations was improved by adding integral terms with an anti-windup mechanism based on the target coordinates to mitigate the overshoots when the input command saturates. The corresponding integral gains are enabled without the need for significant tuning procedures, as is the case with PI controllers.

Overall, the benchmark control algorithms have been challenged by the proposed M-MPC and the results showed how the control approach considered performs better than traditional methods with a reduced current distortion in SyRel drive applications.

Chapter 2

Theoretical Background

2.1 Introduction

The global electric motor market is worth USD 113.14 billion in 2021 and is projected to grow to USD 181.89 billion by 2028 at a compound annual growth rate of 7.0%. The AC motor segment is projected to hold a significant market share (59.7%) owing to the extensive use of AC motors in numerous applications [5]. The global electricity demand and consumption are continuously growing, and policies that boost energy efficiency are vital to meet global climate ambitions in terms of reducing CO² emissions, and consumers would still benefit from lower overall costs.

Nowadays, Permanent Magnet Synchronous Machine (PMSM) are the dominant motors employed in many applications acknowledged for their high efficiency, high torque density, and desirable wide speed range performance. Permanent Magnet (PM) materials are the most important elements of PMSMs and their dramatic rise in price have directed the research towards rare-earth-free machines. Furthermore, the design challenge of the magnets





Motor Type	Stator and Rotor Structure Sample	Different Types	Main Applications	Superiorities	Drawback(s)
IM		<ul style="list-style-type: none"> • copper rotor • aluminum rotor • wound rotor • rotor skewing 	Industrial applications (pump, fan, traction, etc.)	+ low cost of material and manufacturing process + line-start capability	– low power factor – highly probable bearing fault
PMSM		<ul style="list-style-type: none"> • interior PM [42] • surface-mounted PM [43] • line-start PMSM 	precise control and high-speed performance (traction, robotics, aerospace, medical, etc.)	+ high performance in wide speed range operation	– rare-earth material usage
SynRM		<ul style="list-style-type: none"> • line-start SynRM • skewed rotor • rotor with asymmetric flux barriers 	Industrial applications (pump, fan, traction, etc.)	+ reliable and highly efficient due to cold rotor operation + high dynamic + high overloadability + very high-speed capability	– high torque ripple – severe low power factor
PMSynRM		<ul style="list-style-type: none"> • rotor skewing • asymmetric rotor structure • different barrier structure and PM material 	Traction applications	+ very high performance without rare-earth PMs	– hard manufacturing and installment process

Figure 2.1: Different types of rotor topologies [1].

is not trivial. A PM-free alternative resides in the Synchronous Reluctance (SyRel) motor. The rotor design of a SyRel motors distinguishes it from its Induction Motor (IM)s and PMSM counterparts although it is widely considered a PMSM subcategory.

In Fig. 2.1 are shown some of the aforementioned electrical machine types with the corresponding rotor structure, the main applications and the main features of each [1].

The rotor design of Synchronous Reluctance (SyRel) distinguishes it from its IM and PMSM counterparts. Indeed, lack of winding and PMs result in the lower core and bearing temperature with negligible rotor losses [6]. As its name suggests, the SyRel rotor structure is made by an iron core and shaped such that it produces reluctance torque resulting from changing the magnetic reluctance. The magnetic flux produced by the stator current flows into the lowest reluctance path. Hence, if the rotor is not aligned with the flux, the reluctance torque will turn the rotor in the direction with minimum magnetic resistance.

In comparison with PMSM and IM, Synchronous Reluctance (SyRel) attains higher reliability, higher speed range, comparable efficiency in the same power range with the same frame size, higher power density and higher torque-per-ampere ratio [1]. In this sense, SyRel offers the high performance of PMSM, while it can be as cheap, simple, and as service-friendly as IM. These specifications are notable reasons to consider SyRel as a cost-efficient alternative to be employed in many industrial applications.

On the other hand, the SyRel motors have a few drawbacks. The power factor is low and it depends on the saliency ratio. Higher saliency ratios enable higher electromagnetic torques. In applications where the reactive power exchanged with the source has to be limited, the mitigation of the reactive power is essential. An open-end winding configuration with a dual-inverter and a floating capacitor solution has been investigated in [7] to suppress the reactive power of the drive with the plus benefit of extending the torque-versus-speed characteristic compared to the single-inverter solution. Given the anisotropic nature of the rotor, the torque ripple can be significant and considered as one of the main difficulty to take into account. In particular, advanced rotor design has permitted the enhancement of the saliency ratio to address the reduction of the torque ripples through optimization of the rotor structure. Among proposed design solutions, rotor skewing can halve the torque ripples of SyRel, and asymmetric rotor flux barriers decrease the torque ripples significantly.

Another downside of SyRel motors resides in the highly non-linear magnetic behavior to be considered in the modeling [8]. The most critical aspect of an accurate representation of SyRel motors employs laborious identification procedures aimed to identify the relation between flux linkage and stator current. High and predictable control performance is achievable when accurate knowledge of inductance and stator resistance is available.

SyRel machines can have poor low-speed performance, which means they may not be suitable for applications that require high torque at low speeds. SyRel machines may produce more noise and vibration than PMSMs, which can be a disadvantage in applications where low noise and vibration are important. Overall, the choice of electric motor depends on the specific application and the requirements for efficiency, power density, control complexity, and other factors. Each type of motor has its strengths and weaknesses, and the best choice depends on the specific needs of the application

2.2 Magnetic Model Identification Procedures

The magnetic model is the relation between the machine flux linkage and current usually chosen in a rotor reference frame. The self-axis saturation phenomenon in Synchronous Reluctance (SyRel) motors consists of the d and q machine flux linkage components assumed as non linear function of both d - and q -axis current components. As far as the so-called “cross-saturation” phenomenon, the d - and q -axis flux linkage is affected by q - and d -axis current, respectively. So d -axis flux paths become more saturated as a consequence of larger i_q . Therefore, the flux linkages are usually two-dimensional (2-D) functions of d - and the q -axis currents.

Given the importance of having an accurate representation of the magnetic flux maps, follows a description of the existing identification procedures aimed to identify the flux-versus-current characteristics and other significant parameters of SyRel motor drives. Two main categories can be found in literature based on online and offline identification procedures and a classification of the experimental approaches is depicted in Fig. 2.2. The former was recently outlined in [9] for PMSM, and they rely on real-time

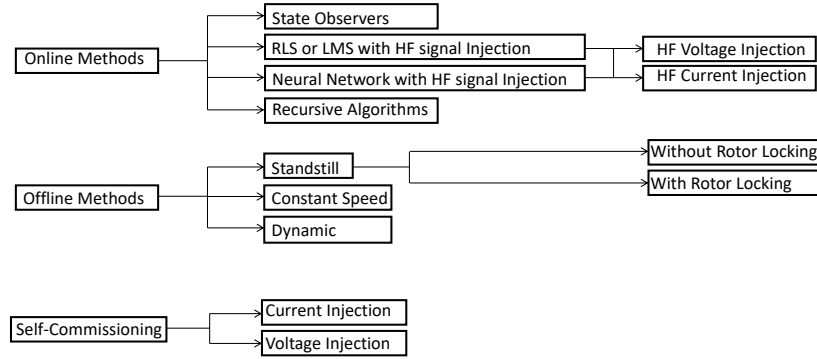


Figure 2.2: Classification of parameters identification procedures applicable to SyRel motor drives.

estimation methods primarily concerned with acquiring electrical and mechanical parameters. The latter was surveyed by [10] and the basic concept is to run specific preoperative tests aimed at identifying system parameters needed to enhance the performance during ordinary operations.

2.2.1 Online Parameters Identification Procedures

The online parameter identification procedures are methods aimed at estimating and updating the parameters of the systems in real time. One of the most straightforward approaches to evaluate the system's parameters reside in state observers, such as Luenberger observer [9]. However, the performance of the Luenberger observer drastically drops when employed with non-linear systems. For this reason, more complex techniques such as recursive least square RLS and LMS algorithms come into place and combine state observers with high frequency (HF) signals injection. Other methods based on artificial intelligence and Adaline Neural network ANN, combined with HF signals injection and optimization processes, can also be found in the literature (i.e., see [9]). In other cases, powerful recursive observers such as extended Kalman filter (EKF) [11] or model reference adaptive system [12] are employed.

Most online parameter estimation methods are based on the system's equations and they suffer from several issues. First of all, if the rank of the matrix based on the dynamic equations of the system is less than the number of parameters to be identified, then the matrix results are rank-deficient. In that case, the estimations are not accurate. Another common limit of these algorithms is the high computational burden due to inverse matrix computation. For this reason, sometimes the full-order EKF are divided into two independent reduced-order EKF [13].

To solve the ill-convergence problem and realize the simultaneous estimation of multiple parameters, some online estimation methods propose to fix one or two parameters to their nominal value and evaluate the missing ones online. It reduces the number of estimates and allows them to address the rank-deficient problem [14]. The precision of the estimated parameters suffers from the variations of the fixed and unidentified quantities. Other research works propose to employ some online parameter estimation algorithms to identify a subset of the machine parameters while using offline measurements for the remaining parameters [15]. Other researchers suggested introducing additional devices, i.e. thermal sensors, and power/torque meters to solve the ill-convergence problem [16]. It increases the cost and the complexity of the overall system as it requires additional devices or constructional changes.

In addition, model uncertainties and measurement noise deteriorate the estimates. This so-called ill-condition implies that the estimations are very sensitive to perturbations in the input and output data. Small changes in the measurements result in large changes in the estimations. Since the voltage measurements of the terminal voltage are difficult, reference voltages are often employed for the estimation, but they suffer from inverter nonlinearities.

Other online identification methods rely on injecting disturbance signals allowing the full-rank reference model. In this case, the injected signal will introduce additional reluctance torque with subsequent ripple.

Besides the described issues among the online parameter estimation algorithms, these techniques rely on offline methods for validations, the reason why more attention was paid to offline approaches.

2.2.2 Offline Parameters Identification Procedures

The offline identification methods rely on preoperation tests conducted at specific conditions to highlight the desired parameter of interest. The most common operations through which those tests are performed include standstill operations with and without rotor locking [17, 18], constant speed tests [19, 20] (or emf-method), and dynamic tests [21, 22]. In the case of SyRel drives, the parameters of interest include stator resistance, inductances, and flux-versus-current maps. For instance, stator resistance can be estimated at standstill through d -axis close loop current control for two different current levels of the same sign [23]. The resistance is obtained from the ratio of the voltage reference and measured current differences with the controller roughly tuned as only steady-state values of voltages and current are needed. Among several acknowledged procedures, the d - and q -axis inductances' can be evaluated through standstill tests by injecting sinusoidal current signals along the respective axes [23]. The standstill operations during these kinds of tests require a sufficiently high frequency of the injected AC signals in order to have the generated force filtered out by the moving mass. The voltage reference and the measured currents are used to evaluate the total impedance along each axis, whose the inductive component can be derived from. The d - and q -axis flux maps can be attained,

i.e, by using constant speed tests by injecting the respective current axis component. These tests consider the steady state voltage equation with voltage references, measured current, and estimated rotational speed for the evaluation [24]. In the following, particular attention was focused on the identification of the flux versus current characteristics. The standstill tests' main idea relies on the excitation of the system with DC, AC, or HF signals and observing and monitoring the system response. Since the tests run at a standstill or quasi-standstill, the speed-dependent term in the voltage balance equation can be neglected. For a given voltage signal, the stator current is measured and the time-derivative of the stator current in rotor coordinates is computed. The inductance along the axis can be achieved from the calculated flux linkage. Standstill operations are guaranteed by physically locking the rotor in a fixed position, injecting signals in a way to avoid torque-generating current components, or injecting HF signal whose resulting torque oscillations around the initial position are filtered out by the moving mass.

In [21], a capacitor discharge method enables the calculation of the self-axis inductance but it does not take into account the cross-magnetization effects. In [25] a DC decay test is used to estimate both the self- and cross-axis saturation phenomenon. The aforementioned methods rely on the availability of testing facilities with expensive laboratory equipment, i.e., signal generators, power analyzers under prescribed supply and ambient conditions, and qualified personnel.

These methods become impracticable when the machine cannot be detached from its load. Under such conditions, self-commissioning [26] of the drive system thus comes into play, consisting of an automatic determination of machine electrical parameters before the drive is put in continuous operation. These techniques employ computational algorithms executable on

low-cost microcontrollers, a power converter, and available sensors with the least operator intervention and practically no available information about the machine. These procedures are executed in an as short time as possible without rotor locking or at standstill. The recorded data is post-processed to obtain the parameters of interest. However, when a power electronics converter is used for characterizations, the knowledge of the actual voltage applied to the machine becomes imperative and any error caused by the inverter dead-time or the ON-state resistance must be addressed or compensated. It has also to be remarked that the accuracy of these procedures is poor due to a lack of accurate measurement and analysis tools. Among the self-commissioning methods, in [23] alternating d - and q -axis sinusoidal current signals are injected without rotor locking mechanisms; the impedance along each axis and subsequently the inductance is estimated through the controller computed voltage references, and the measured currents. In [27] the same concepts are tested considering a dc-biased AC test current. In [28, 29, 30, 31] the transient current response to HF voltage steps is used to evaluate the motor inductances and the flux linkage maps. However, the estimation of the flux-linkage based on integral calculations might lead to large drifts due to noise and DC offsets in the current measurements. Furthermore, the effect of the inverter nonlinearities should be taken into account as reference voltages are considered in the estimation instead of the actual voltages.

As far as the constant speed tests, also known as the emf-method, require an additional machine mechanically coupled to the machine under test acting as a dynamometer that maintains the shaft at a constant speed. Contrary to standstill tests, the flux estimation relies on the speed-dependent term at steady-state [32, 20, 19]. During the test, constant current on the d - and q -axis are applied and the flux is computed using the feedback current and

the reference voltage vector. The inductances can be evaluated from the estimated flux-versus-current maps. The value of the resistance and its thermal effect are important to consider, even though the term has a lower weight concerning the emf-voltage when compared to the standstill methods. Also, in this case, the distortion introduced by the inverter nonlinearities [23] alter the estimation due to the dead time switching events and voltage drops across the semiconductors. This effect can be compensated within the measurements. The noise during measurements and periodic disturbances are minimized throughout the identification process by averaging the measurements over one mechanical rotor revolution. Dynamic tests without additional brake or prime mover, when the machine accelerates or brakes have also been considered such as in [22]. In this case, the dyno is not needed and the method does not require information about the stator phase resistance, and no open-loop integrator is used for the flux estimation which makes this method robust against temperature and measurements drift effects even though is considered the least established method for validation.

Once the flux maps are identified, they can be included in control algorithms via look-up tables or explicit functions [20, 33]. The LUT is a simple way to model the saturation characteristics but it needs a large memory to save the data acquired. Furthermore, the LUT is discontinuous and defined only in the acquired range, and the interpolation may not be very efficient. On the other hand, the explicit continuous functions are preferable to avoid storing loads of measurement data in a continuous and differentiable manner. For simplicity, in this work, the LUT solution has been considered.

Among the offline identification procedures, other stand-alone criteria can be found. Analytical and Numerical methods rely on finite element mod-

eling of the electrical machines such as in [34] and [32] where winding functions are used to evaluate the flux maps. However, such tools require confidential information such as material properties, shape, and manufacturing tolerance held by motor designers. A practical approach employs analytical equations as well as the machine's nameplate data. However, it can serve as a preliminary source of information although the parameters thus obtained are grossly approximated and provide valuable input for further identifications. The described methods can accurately serve parameter identification purposes. Nevertheless, as well as for the online identification methods, it is worth to remark the limits of the flux maps procedures. First of all, it is not computationally free the implementation of LUT or explicit functions of several variables. In addition, the offline methods also fail to deal with any changes in the machine parameters during operation such as temperature hikes, magnetic saturation, and aging factors. However, the procedure given by [19] was the one followed in this thesis to characterize the studied SyRel drive and it will be further described in Sect. 3.3. This procedure falls into the constant speed test group and it acknowledges that stator voltage drop is inherently compensated, and given the numerous applications of such method, it can be considered the state-of-the-art for PMSM motors magnetic model identification.

Once the flux linkages versus current characteristics are known, favorable operating points such as maximum torque per ampere Maximum Torque per Ampere (MTPA) and maximum torque per voltage MTPV trajectory can be identified and imposed to minimize the power losses.

2.3 SyRel Control Techniques: State of the Art

The advent of powerful microcontrollers and microprocessors at low cost gives to researchers the flexibility to test numerous control approaches to reach the desired performance. The control techniques are aimed at finding the actuation command to control the torque, speed, and position of the electric motors.

The stability over the whole operating region is the key feature the controller has to guarantee. The first goal of the control algorithms in electric drive applications is to achieve the desired performance at steady-state and during transients. A good control design allows tracking the reference signals while minimizing the torque ripple, which leads to lower acoustic noise and higher efficiency of the system. Linked to the torque ripple is the overall current harmonic content to be reduced, or specific harmonics to be suppressed.

Another essential feature worth mentioning is the robustness against parameter variation (e.g., stator resistance and inductance), external disturbances (e.g., load), and measurements noise are one of the main features investigated by the researchers to achieve high-performance control systems. Variations due to the temperature and saturation phenomena are likely to degrade control accuracy leading to instability.

In VFD applications, high performance at high speeds in the flux weakening region is of paramount importance, especially in traction applications. The selection of specific operation trajectories such as the MTPA or the Maximum Torque per Voltage (MTPV) is aimed to minimize the power losses guaranteeing the maximum achievable torque at high speed. The practical

difficulty of implementing the control algorithm is another feature to be considered. The simplicity of a control method denotes less computational burden, thus preferable to low-cost control platforms. The performance of the control methods in transient mode is also crucial to pay attention to. Ideally, a control system should guarantee as fast a dynamic response as possible in terms of rising time and settling time while mitigating the overshoots. The rest of this section describes the main control methods and the achievements in this area that have been recently presented in the literature.

In practice, control strategies for motors including SyRel are classified as scalar and vector control methods. Scalar control methods are by far the simplest control techniques, mainly known as V/f control methods. Therefore, if a simple control algorithm is looked for, scalar control can be a desirable choice. They can be applied in open-loop or closed-loop control systems with current and speed sensors or with a sensorless control approach. These techniques consist of generating the voltages with a certain amplitude and frequency whose ratio is kept constant. This simple concept makes the methods applicable to many low-cost-demanding purposes. However, the tracking of the commanded signals is not guaranteed and poor dynamic performance is observable.

Field-Oriented Control (FOC), Direct Torque Control (DTC), and model predictive control (MPC) methods belong to the vector control category and they result significantly more effective than scalar approaches. These methods have been described in tons of papers in the last decades and they are widely established in the industry as well. The next subsection presents this methods in detail to report the most recent developments.

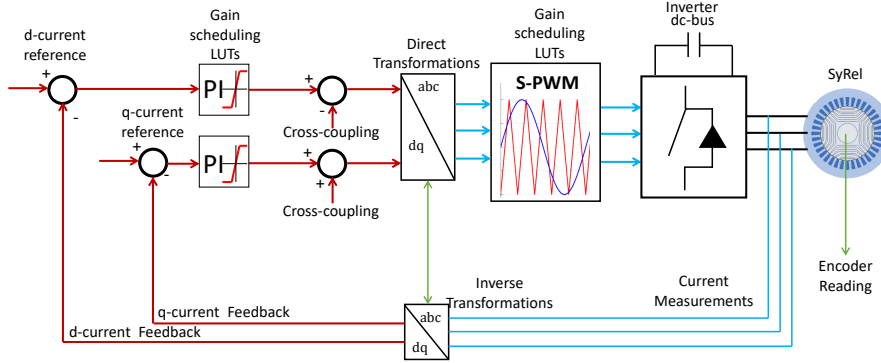


Figure 2.3: FOC block diagram.

2.3.1 Field-oriented Control

The FOC method is one of the most widely used control techniques in VFD applications. Acknowledging the effectiveness of this control method, low ripple, and the constant switching frequency features, it can be considered one of the most established benchmark for SyRel drive applications. This method is based on Proportional-Integral (PI) controllers in the synchronous reference frame (see Fig. 2.3). The advantages of FOC are as follows: 1) high steady-state performance; 2) precise current control; 3) simple implementation of the method; 4) simple compatibility with many AC motors; 5) simple modulation system implementation; 6) constant switching frequency.

To achieve superior performance, some hybrid control methods are developed, such as Direct-Flux Vector Control (DFVC) [35, 36]. DFVC is a combination of FOC and DTC, regulating the stator flux amplitude directly. This control method controls the q -axis current in the stator flux reference frame instead of torque (as in DTC), which is convenient in the field-weakening operation of the motor as it is applied to AC motors including SyRel. This method keeps the high performance of FOC with the relatively high dynamic of DTC. However, the stator resistance variation

results in significant errors in the estimated stator flux, especially at low speeds when the voltage drop across the stator resistance is comparable to the back-EMF. The stator resistance varies with the temperature, and if the stator resistance estimate is considerably bigger than the actual value the system may become unstable. Considering the voltage equation to estimate the stator flux, the accuracy of the estimate significantly depends on the variations of the stator inductance. Usually, the stator inductance decreases with increasing stator current. As such, the online estimation or offline identification procedure of stator resistance or inductance is often required to achieve adequate performance. The previous observations make the proportional and integral gains of the current regulators harder to tune. In fact, the machine parameter variation indirectly affects the control performance of FOC, even though the control strategy directly employs neither of them whereas PI regulators would require gain adaptation throughout the torque-speed domain [37]. In overall, FOC has a simple control scheme that makes it easy to be implemented in practical applications. The switching frequency of FOC is inherently constant. But the switching frequency of FOC is typically high for a given sampling frequency, which means it is suitable for low-power applications. However, the recent advance of SiC-based technology power modules in standard converters reduced the issues related to high-frequency applications and the subsequent power losses on the converter, making this controller well-suited for high-power applications. In general, the FOC is well suited for linear systems acknowledged by the linearity of the PI controllers, thus, the adoption of this method in a nonlinear system such as the SyRel motor makes the tuning and the implementation more complex. Other concerns about the FOC method are the complexity of S-PWM modules implementation that require the usage of devices such as FPGA over DSP or microcontrollers due to limits in the hardware capacity, i.e., the operating sampling frequency.

2.3.2 Direct Torque Control

Direct Torque Control (DTC) is another possibility to control SyRel drives [38, 39, 40], even though it is more prone to higher torque ripple. In the Direct Torque Control (DTC) method, the instantaneous torque of the motor, as well as stator flux linkage, are directly controlled in a stationary reference frame avoiding the Park coordinates transformations (see Fig. 2.4). The switching table is implemented as a LUT, as well as hysteresis controllers opt for a defined combination of switching sequences with regard to the inputs. The inputs of the switching table are the stator flux and torque errors along with the sector of the stator flux. Stator flux and torque estimators are carried out through observers based on the stator voltage equation which establishes the predominant computation burden. The selected actuating signal is applied for the whole sampling period causing the motor torque to increase/decrease to a higher/lower value than the demanded torque. The resulting high torque and flux ripples are due to the lack of control actions during one sampling interval. A viable solution is proposed in [41], where active voltage vectors are employed for some period of sampling time and apply zero voltages for the rest of the sampling time. In this way, the hysteresis bands are not violated, and notably reduced torque and flux undulations are achievable. Besides, a notably higher switching frequency occurs in switches.

In general, DTC assures higher transient torque control performance. Furthermore, it is robust against parameter variations and it is viable in servo applications due to the fast dynamic. In general, the users who are seeking a better transient response, rather than a steady-state response, are inclined to DTC.

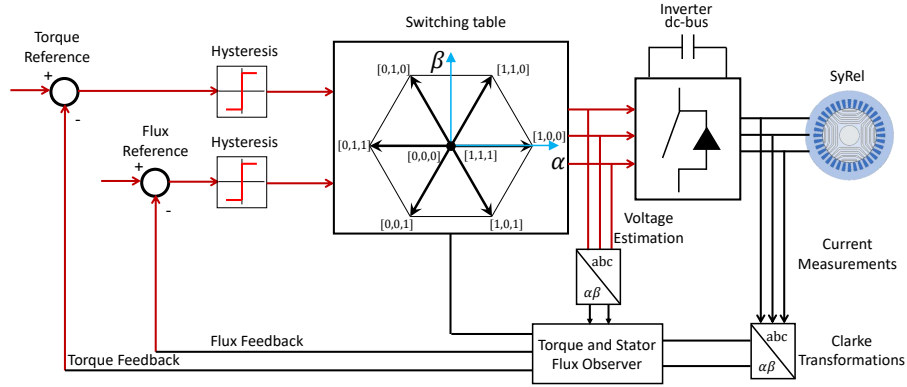


Figure 2.4: DTC block diagram.

2.3.3 Model Predictive Control

An interesting alternative to the aforementioned control techniques belonging to the vector control family is model predictive control model predictive control (MPC), especially in its direct and indirect form known as finite control set MPC Finite Control Set Model Predictive Control (FCS-MPC) [42] and Modulated Model-Predictive Control (M-MPC), respectively. Such a control strategy can effectively deal with complex, constrained, non-linear systems such as SyRel motor drives. Aimed to achieve fast dynamic response, null steady-state errors, and accurate tracking of control variables, electrical parameters and the nonlinear magnetic characteristics of Synchronous Reluctance (SyRel) motors need to be accurately identified for both design and control purposes. Acknowledged the model-based nature of such control techniques, mismatch or variations on the estimated parameters lead to poor control performance [43] and the non-constant switching frequency might limit the number of applications where the FCS-MPC can be employed. However, the high potential and the increasing interest from the researchers in the MPC algorithms, with the advent of powerful microprocessors at low cost, makes these strategies of high interest in drives applications.

Indirect MPC inherently overcomes the non-constant switching frequency issue of FCS-MPC and higher robustness versus parameters variations as well as lower current distortions and, consequently, a reduced torque ripple are achievable while still keeping competitive dynamic performance.

2.3.3.1 Finite-Control-Set Model-Predictive Control

FCS-MPC is nowadays particularly relevant thanks to the readily available hardware and software solutions that can deal with the associated underlying computational complexity of MPC algorithms, which used to be the main barrier to its adoption in the past. FCS-MPC is conceptually simple since the quality of the system behavior is quantified by a cost function that captures the control objectives. This function is evaluated for each one of the possible switch positions of the converter, and the one resulting in the minimum cost is selected and applied to the converter.

As can be seen in literature [44], usually the cost functions of FCS-MPCs take into account the reference tracking error terms [45]. However, as explained in [44], lack of penalization of the control effort can lead to poor performance due to the low switching granularity, i.e., low sampling-to-switching frequency ratio. The control effort factor was considered in several works aimed to minimize the switching losses as in [46], where the change of the switching state was penalized to reduce the commutation losses of a matrix converter. The same approach was adopted in [47] and [48] to control a PMSM and a SyRel, respectively. In [48], particular focus was given to the prediction horizon to enhance the MPC performance at steady-state, even though just simulation results were provided. For this reason, in this work, conventional FCS-MPC is revisited, and special attention is paid to the impact of the control weighting factor on the cost

function to improve the steady-state performance of the drive, while not deteriorating its dynamic behavior.

Another typical issue inherent to model-based control strategies, such as FCS-MPC, is the usually inaccurate and/or incomplete knowledge of the model of the system, leading to steady-state errors that can adversely affect the reference tracking performance of the controller [49]. As far as SyRel drives are concerned, accurate identification of the magnetic model and inverter non-linearities is needed. Several approaches have been employed to tackle the model inaccuracies such as in [50], where the adoption of an online least-squares system identification can significantly improve the reference tracking behavior of MPC. In [51], an integral term was included in the cost function to deal with potential steady-state errors. The latter approach is the one followed in this work due to its simplicity and straightforward adaptability.

In order to implement MPC strategies, two stringent hardware criteria must be satisfied. Firstly, the computing capability of the controller must be sufficiently high to execute the control algorithm in real-time. This is addressed by economically affordable digital control chips based on field-programmable gate arrays (FPGAs) and digital signal processors (DSPs) capable of handling computationally demanding algorithms like FCS-MPC. Furthermore, the power modules of the driving converter must ensure high switching frequencies while respecting the physical limitations imposed by the semiconductor devices. The adoption of silicon-carbide (SiC) power switches allows keeping the operating temperature within the safe working region of the devices while running at very high switching frequencies [52, 53]. Compared with Si isolated-gate bipolar transistor (IGBT), the SiC devices allow for higher operation temperature without suffering from intrinsic conduction effects because of the wide energy bandgap and thus

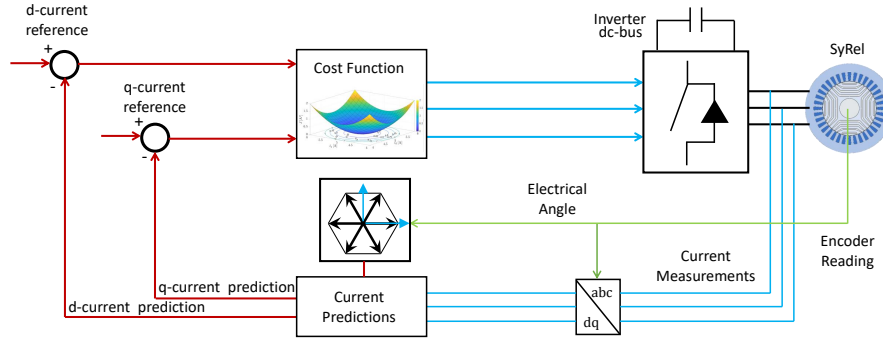


Figure 2.5: FCS-MPC block diagram.

lower specific on-resistance; they also feature higher breakdown electric field, making them very suitable for higher switching speed and less switching loss [54], which are the FCS-MPC's requirements to enhance the drive performance.

According to the working principle of FCS-MPC, the system behavior is predicted for all feasible actuating commands. The one that minimizes a given cost function is selected and applied to the power converter (see Fig. 2.5). Nevertheless, [44] states that the lack of the control effort penalization leads to poor performance and, consequently, a low granularity of switching. Several studies considered the control effort in their cost functions, such as in [46], where the penalization in the change of the switching state results in a reduction in the commutation losses of a matrix converter. The same practice was adopted in [48] and [47] to control a PMSM and a SyRel, respectively. The latter provides simulation results focused on extending the prediction horizon to enhance the MPC performance at steady-state.

Another common difficulty with FCS-MPC is that inaccurate knowledge of the system model can negatively influence the reference tracking performance of the controller [49]. When it comes to SyRel drives, a precise identification procedure of the nonlinear magnetic model is required, unless the controller inherently compensates for any potential model mismatches.

A few approaches have been proposed, mainly applied to PMSMs, to improve the robustness of FCS-MPC. In [51, 55], the integral of the state was included in the cost function, resulting in an augmented prediction model of the PMSM. In [50], real-time least-squares system identification was adopted to correct any set-point deviations. In [3], an integral term was added to the cost function without augmenting the system state. However, it has to be underlined that including an integral term within the cost function, calculated based on the state prediction, increases the algorithm complexity and its computational burden.

2.3.3.2 Modulated Model Predictive Control

Other papers have appeared in the scientific literature proposing modulated approaches resulting in fixed switching frequency and reduced torque ripple (see Fig. 2.6). This approach consists of evaluating the time application of two or more switching states according to the defined online optimization process. In [56] and [4], novel actuating selection criteria with a subsequent duty cycle calculation were considered to control PMSM drives. The same approach was used in [57] to control the electromagnetic torque and the reactive power of a doubly-fed induction machine. A similar approach aimed at achieving constant switching frequency was introduced in [58] to control an RL load throughout a matrix converter.

In the existing literature, fixed frequency CCS-MPC algorithms applied to SyRel drives are barely found, and the few that are cited below assume the SyRel as a linear system neglecting saturation phenomena. In [59], the duty cycle computation is based on a sequential optimization of cost functions which leads to non-optimal solutions [44]. Furthermore, only simulation results were provided. In [60], a different approach was followed to

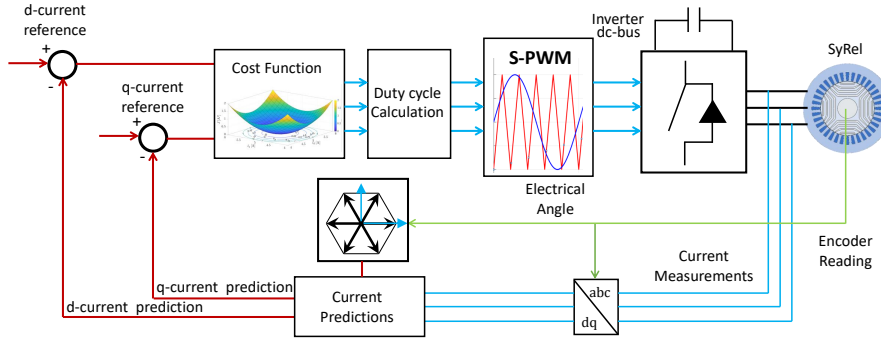


Figure 2.6: M-MPC block diagram.

compute the duty cycle to control a four-switch three-phase inverter-fed linear SyRel. In those papers, an accurate assessment of the overmodulation region, as well as a robustness analysis against parameters variation, were missing. Both the FCS-MPC and CCS-MPC approaches show poor reference tracking performance under parameter mismatches.

Dead beat current control (M-MPC) is categorised as belonging to the CCS-MPC family [44]. It is one of the solutions adopted to achieve high-bandwidth control loop at fixed switching frequency [41]. This method computes the actuation command based on the model characteristics, thus deterioration of Dead beat current control (M-MPC) performance and eventual instability might occur due to mismatch in model parameters, unmodelled delays, dead-time effects, and other errors in the model. All the methods belonging to the CCS-MPC category recently appeared in the scientific literature did not deeply investigate how to improve the robustness of the control. A few papers have introduced integrating terms based on the state increment [61, 62, 63, 64, 65, 66] which can successfully address the problem but increasing the system complexity and the number of computations significantly.

2.3.4 Other Control Techniques on SyRel Motor Drives

Other sophisticated control techniques applicable to SyRel motor drives are reported in the following under the group defined as "Others." Given the enormous number of variants for all the control strategies existing in the literature and all the possible combinations among them, a unique classification is highly complex to define. For this reason, the control techniques mentioned in the following are the few recently developed with high potential to become new benchmarks in SyRel motor drive applications.

2.3.4.1 Model-Free Control

Recently, model-free or non-parametric model predictive control (MPC) emerged in electric drives with sophisticated disturbance observers such as Ultra-local Modeling (ULM) and auto-regressive exogenous (ARX) modeling. They compute the actuation commands according to an optimization problem based on past measurements, whose data are stored in LUT. These techniques have shown competitive performance in PMSM drives [67, 68] but they have not been deeply investigated on SyRel drives. A few applications can be found in [69] and [70]. However, model-free MPCs are prone to several issues: the principal one is named stagnation, consisting in applying the same actuation state for several samples due to a lack of previous information occurring during the start-up. It may require several samples to have sufficient data to provide a good modeling. As stated and proved in [71], model-free controllers show poorer steady-state performance when compared to model-based with SyRel drives.

2.3.4.2 Deviation Model-Based Control

In [72] and [73], a new control method for a SyRel drive was introduced where the commonly used PI current regulators are replaced by novel deviation equations. Compared to the IMs and PMSMs counterparts, the lack of parts mounted on the rotor enables a higher speed range. The rotational force can reach higher thresholds set by the structural stress of the rotor core weakened by rotor barriers designed to guide the flux streamlines. As its name suggests, this method benefits from a deviation model of the motor for control. With this approach, the model of the motor is simplified through normalization to obtain the deviation model of the motor. Then, the deviation model of the motor is utilized to compute the actuation for the system. As a result, the proposed approach provides a simple control scheme with no need for parameter knowledge and controller tuning. This approach contributes to other electrical drives to simplify the machine equations, reduce control complexities, such as the number of conventional controllers, and overcome the problem of machine parameter dependency. In [72], the Deviation Model-Based Control (DMBC) of SyRel is proposed in comparison with FOC and DTC. The method shows simpler and more robust control against parameters' variation compared to the FOC. Besides, Deviation Model-Based Control (DMBC) presents less torque ripple, higher dynamic, and better flux regulation at startup when compared with DTC and there is no need for PI calibration. However, given the number of citations on this approach, this technique is not yet mature and further investigations are required to consider it as a solid benchmark.

2.3.4.3 Sliding Mode Control Technique

The sliding mode control (SMC) [74] is a controller well suited for highly nonlinear time-varying systems such as SyRel motor drives. The SMC features strong robustness, disturbances rejection, and fast response to uncertainties control including certain internal parameter variations and external disturbances. On the other hand, this control method typically features unwanted oscillations known as chattering phenomena. An attempt to mitigate such oscillations was conducted in [75] by employing an augmented-order version of the SMC. Lower chattering and higher accuracy were achieved for a SyRel motor drive application. Such nonlinear controllers combine intelligent and adaptive control methods to identify the uncertainty in SyRel drives.

2.3.4.4 Artificial Intelligence Control Techniques

Traditionally, all the conventional control methods are based on machines' models or some predefined strategies. To alter this classic view on the control system, lately, artificial intelligence-based controllers have been implemented in the power electronics and drive systems. To name a few, Fuzzy Logic (FL), Artificial Neural Network (ANN), and Adaptive Recurrent Fuzzy Neural Network (ARFNN) are the methods that have been studied for SyRel drives. This provides a control system with characteristics compatible with the physical components. Lower cost in comparison with the traditional systems, higher efficiency, more robust system, more reliable, more customizable, and the possibility to emulate human deductive thinking are some advantages of FL control [76]. The drawback of fuzzy control can be the need for high human expertise and regular updating of rules, not applicable for much smaller or larger data than historical

data, and the requirement for massive data.

Chapter 3

SyRel Drive Modelling

In this chapter, the mathematical model used to carry out the simulation studies on the SyRel drive is described. Firstly, the converter model is given by considering an ideal approach with an instantaneous switching pattern, and neglecting the conducting and the switching losses. Secondly, the motor model is derived, and the experimental test results, aimed at identifying the fluxes-versus-current maps, are presented to show the SyRel non-linearities to characterize the motor.

3.1 Two-Level Voltage Source Inverter

The primary function of a voltage source inverter is to convert a fixed dc-voltage to a three-phase ac-voltage with a variable magnitude and frequency. A two-level voltage source inverter (2L-VSI) will be considered to drive the SyRel motor, whose line-to-line voltage level can be varied between $-V_{dc}$ and V_{dc} by the dc-link voltage bus. A simplified circuit of a 2L-VSI is shown in Fig. 3.1.

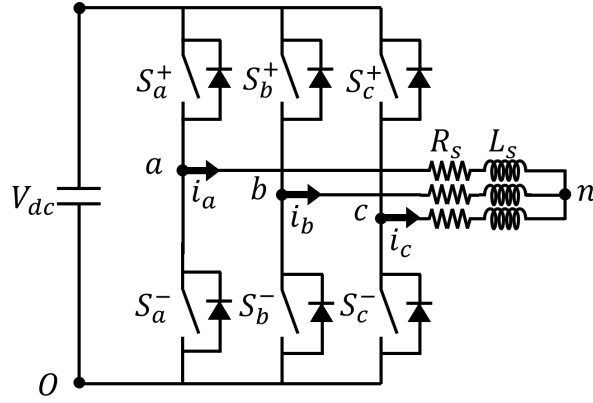


Figure 3.1: 2L-VSI circuit.

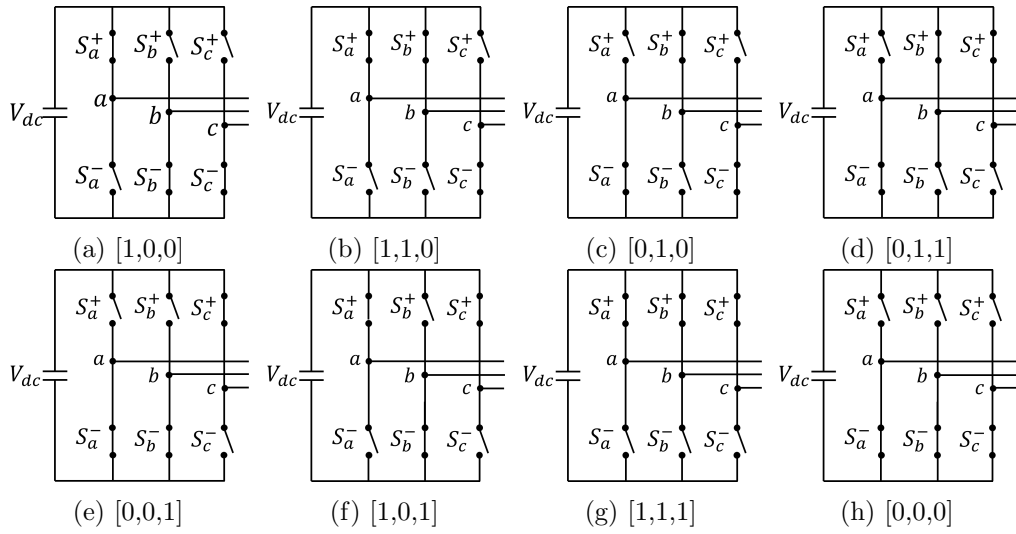


Figure 3.2: Feasible configurations of a 2L-VSI

The inverter is composed of six power switches and six free-wheeling diodes displaced as three cascaded half-bridges. Each leg, denoted by a , b , and c , have a high-side switch denoted as S_a^+ , S_b^+ , S_c^+ respectively, connected to the positive dc voltage source, while the low-side switches denoted as S_a^- , S_b^- , S_c^- are connected to the ground. The free-wheeling diodes (also known as fly-back diodes) are connected anti-parallel to each switch, whose purpose is firstly to guarantee the four quadrant operations and secondly they have to provide a path for the decay of current when the corresponding switch rapidly turns off. Eight feasible configurations are achievable by a 2L-VSI, and they are represented in Fig. 3.2. The phase-voltage

components of the eight possible switch positions (n) can be calculated as

$$\begin{cases} v_a(n) = \frac{V_{dc}}{3} [2S_a(n) - S_b(n) - S_c(n)] \\ v_b(n) = \frac{V_{dc}}{3} [2S_b(n) - S_a(n) - S_c(n)] \\ v_c(n) = \frac{V_{dc}}{3} [2S_c(n) - S_a(n) - S_b(n)] \end{cases} \quad (3.1)$$

where V_{dc} is dc-link voltage, $S_a(n)$, $S_b(n)$, and $S_c(n)$ are the on-state (one), or off-state (zero) of the switches, whose values are listed in Table 3.1. The corresponding line-to-line voltage values $V_{ab}(n)$, $V_{bc}(n)$ and $V_{ca}(n)$ are also reported in the same table for each configuration of the 2L-VSI. These configurations correspond to six active voltage vectors denoted in the stationary reference frame (i.e., α , β coordinates) by $\mathbf{v}_{\alpha\beta}(1, 2..6)$, and two zero voltage vectors denoted by $\mathbf{v}_{\alpha\beta}(0)$, $\mathbf{v}_{\alpha\beta}(7)$, shaping an hexagon in a stationary, orthogonal reference frame ($\alpha\beta$ coordinates), see Fig. 6.1.

By using the following transformation, the voltage vectors can be calculated in a rotating synchronous reference frame (i.e., dq coordinates) as

$$\mathbf{v}_{dq}(n) = \mathbf{P}\mathbf{v}_{abc}(n) \quad (3.2)$$

where $\mathbf{v}_{abc}(n)$ is the phase-voltage vector, \mathbf{P} is the rotation matrix combining the well-known Clarke and Park transformations as function of the electrical angle θ_r , i.e.,

$$\mathbf{P} = \frac{2}{3} \begin{bmatrix} +\cos \theta_r & +\cos \left(\theta_r - \frac{2\pi}{3}\right) & +\cos \left(\theta_r + \frac{2\pi}{3}\right) \\ -\sin \theta_r & -\sin \left(\theta_r - \frac{2\pi}{3}\right) & -\sin \left(\theta_r + \frac{2\pi}{3}\right) \end{bmatrix} \quad (3.3)$$

The fundamental reason to transform the three-phase instantaneous electrical quantities into the synchronously rotating reference dq frame is to

Table 3.1: Switching states of the 2L-VSI.

n	0	1	2	3	4	5	6	7
$S_a(n)$	0	1	1	0	0	0	1	1
$S_b(n)$	0	0	1	1	1	0	0	1
$S_c(n)$	0	0	0	0	1	1	1	1
$v_{ab}(n)$	0	V_{dc}	0	$-V_{dc}$	$-V_{dc}$	0	V_{dc}	0
$v_{bc}(n)$	0	0	V_{dc}	V_{dc}	0	$-V_{dc}$	$-V_{dc}$	0
$v_{ca}(n)$	0	$-V_{dc}$	$-V_{dc}$	0	V_{dc}	V_{dc}	0	0

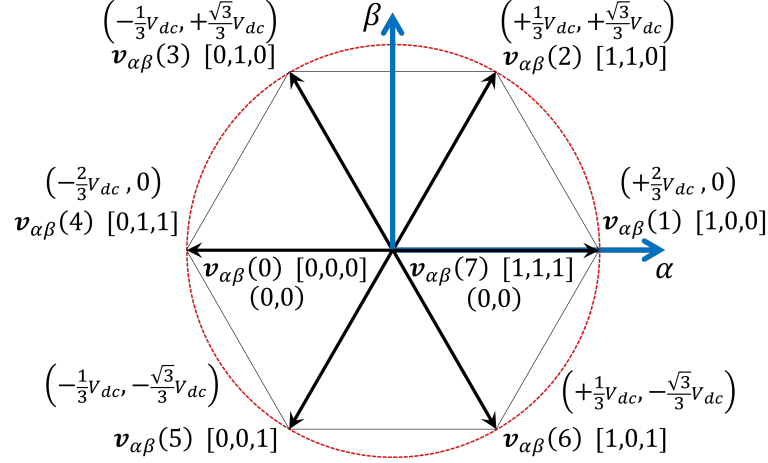


Figure 3.3: 2L-VSI switching states.

make computations much easier. Secondly, it allows the system operator to independently control the active (d-axis) and reactive (q-axis) components of the currents. Similarly, in the aspect of the machine, the flux and torque can be independently controlled. This way, the coupling effect can be minimized to a great extent.

3.1.1 Modulation Stage: Sinusoidal Pulse-Width Modulation

The gate signals to set the desired configuration of the 2L-VSI are obtained considering a carrier-based sinusoidal pulse-width modulation (S-PWM) stage. It consists of comparing a carrier signal \hat{v}_{tr} with the reference voltage vectors v_a^* , v_b^* , v_c^* , normalised with respect to the dc-link voltage to

synthesise the desired a -, b -, and c -phase voltage vector according to the following criteria:

- $\hat{v}_{tr} > v_a^*$, $S_a^+ = 0$, $S_a^- = 1$
- $\hat{v}_{tr} < v_a^*$, $S_a^+ = 1$, $S_a^- = 0$

With the same fashion the b -gate signals S_b^+ and S_b^- can be obtained as

- $\hat{v}_{tr} > v_b^*$, $S_b^+ = 0$, $S_b^- = 1$
- $\hat{v}_{tr} < v_b^*$, $S_b^+ = 1$, $S_b^- = 0$

and the c -gate signals can be obtained as

- $\hat{v}_{tr} > v_c^*$, $S_c^+ = 0$, $S_c^- = 1$
- $\hat{v}_{tr} < v_c^*$, $S_c^+ = 1$, $S_c^- = 0$

When the corresponding switching signal is one (e.g., $S_a^+ = 1$), the corresponding power switch is in conducting mode. On the contrary (e.g., $S_a^+ = 0$), the corresponding power switch blocks the current flow through it. Acting on the duty cycle of the power switches permits the synthesis of the mean value of the reference voltage, and commands the amplitude of the first harmonic of the desired signal.

The carrier signal consists of a triangular waveform with a fixed sampling frequency f_s (also known as carrier frequency), which is set to achieve the desired switching frequency to generate the gate signal to drive the power switches "ON" and "OFF". The triangular waveform is achieved by employing an increasing and decreasing counter synchronized with the clock mechanism of FPGA-based devices.

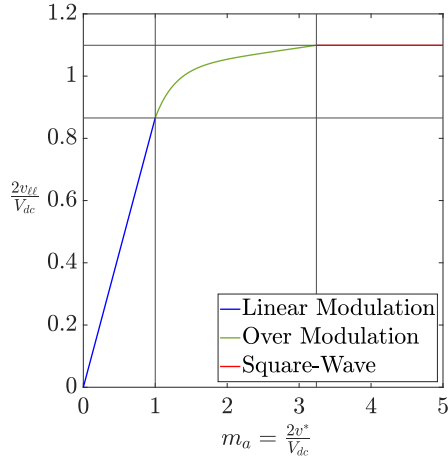


Figure 3.4: Modulation index.

Three different operating regions can be identified for the 2L-VSI according to the relation between the reference voltage and the triangular carrier and they are represented in Fig. 3.4. The first one is the linear region, meaning that the output of the first harmonic of the resulting line-to-line voltage output (v_{ll}) is proportional to input voltage v^* ; in this region, the voltage reference is lower than the triangular waveform. The second region is called the overmodulation region where a decreasing trend between the input reference voltage and the output voltage is observable; in this case, the voltage reference is slightly greater than the carrier signal. Finally, the square-wave region is characterized by the output voltage not affected by changes in the input reference signal. Each modulation region features characteristic harmonics around the switching frequency named side-band harmonics.

In Fig. 3.5a is shown the comparison between the triangular carrier (\hat{v}_{tr}) and the reference voltage (v_a^*) normalised with respect to the dc-link voltage and the resulting gate signal (S_a). Follows in Fig. 3.5b the resulting line-to-line voltage V_{ab} with the corresponding first harmonic V_{ab1} , and in Fig. 3.5c, the resulting harmonic spectrum. It is possible to observe the side-band harmonics at integer multiples of the switching frequency (i.e.,

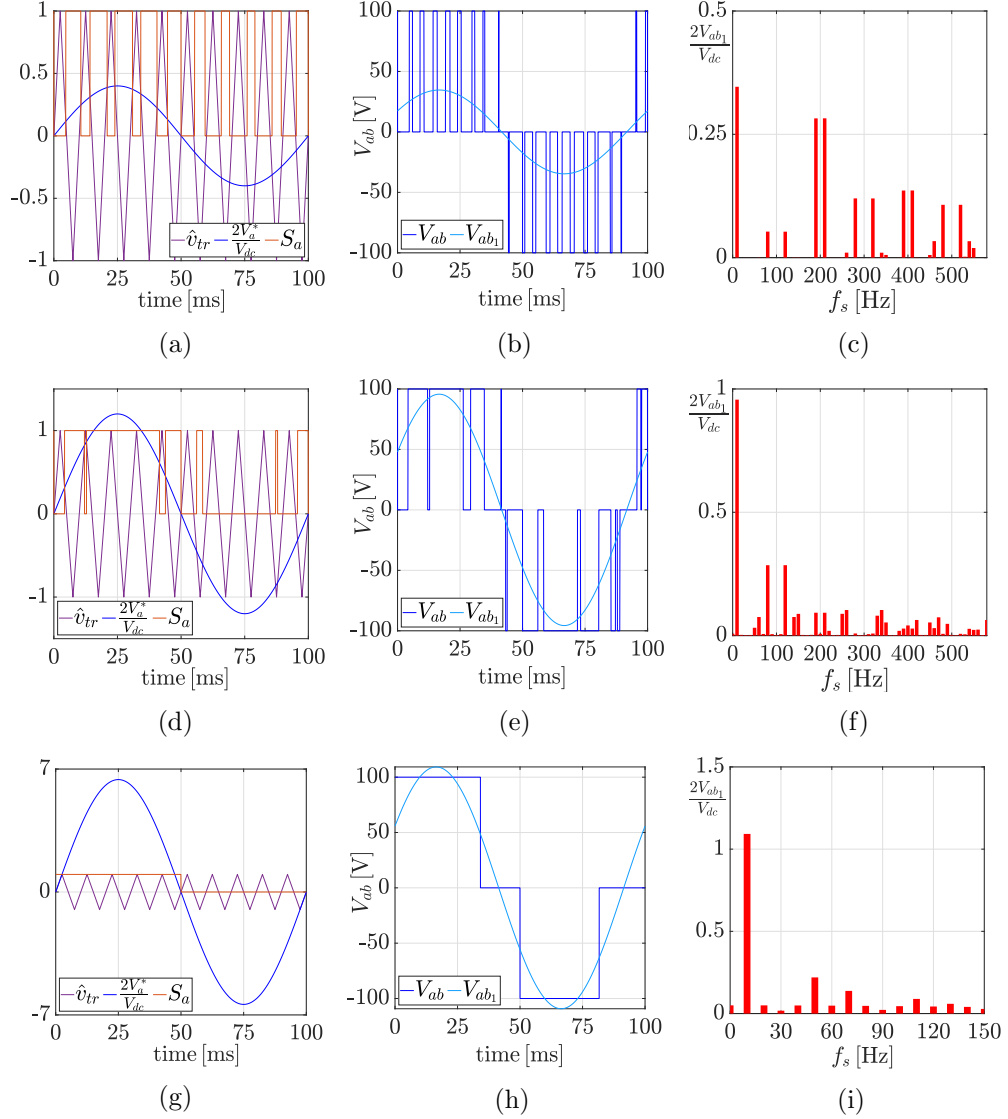


Figure 3.5: S-PWM.

$f_s = 10$ kHz). The same aspects have been shown in the case of the over-modulation region in Figs. 3.5d, 3.5e, 3.5e. It can be noticed how the harmonic spectrum presents lower harmonics content with higher magnitude than in the former case. Finally, When the system operates in the square-wave region (see Figs. 3.5d, 3.5e, 3.5e), the harmonic spectrum presents the typical square-wave harmonic pattern with thirties harmonic and their integer multiples negligible. The first harmonic peak value exceeds the square-wave voltage by 10 %.

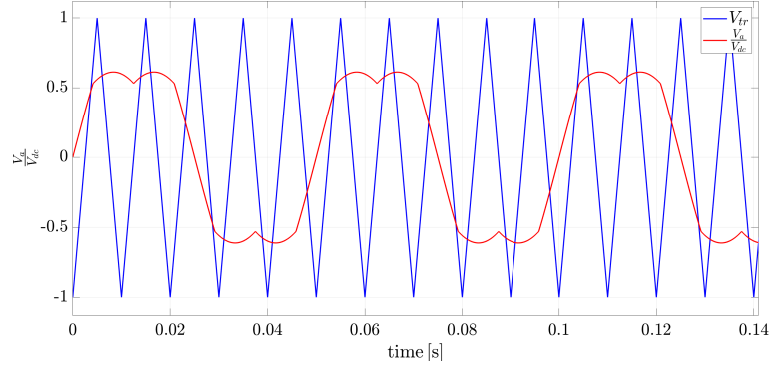


Figure 3.6: .

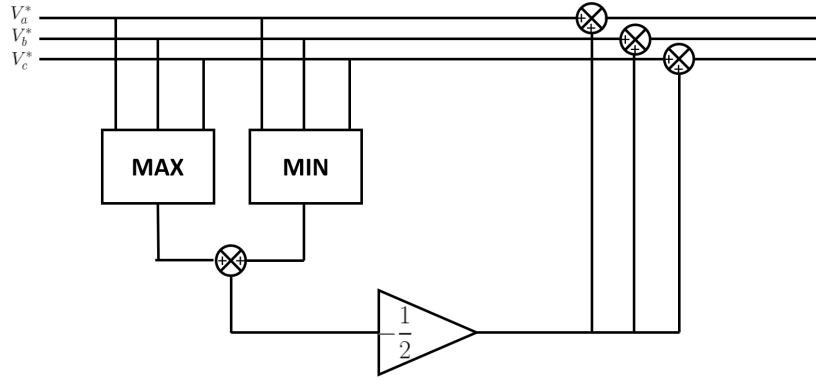
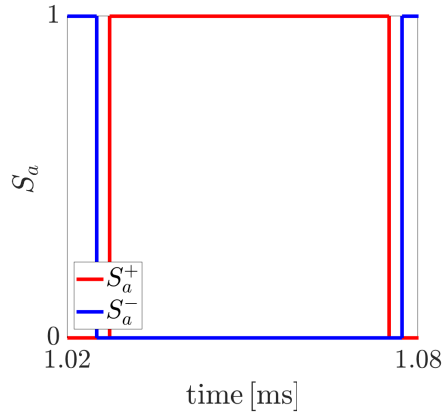


Figure 3.7: Third harmonic injection scheme.

3.1.2 Modulation Stage: Third Harmonic Injection

To extend the linear modulation region, a common-mode voltage can be injected into each reference voltage component. For the case study, the signal injection was based on the third harmonic of the signal. The block diagram of the third harmonic injection is shown in Fig. 3.7. In this way, the dc-link voltage can be fully harvested. In addition, the output voltage is synthesized without introducing distortions to the input signal. Furthermore, it has the advantage of increasing the linear modulation zone by 15% compared to the S-PWM without common-mode signal injection. For each phase, the following formula is applied to get the third harmonic injection:

$$V_{an}^* = -\frac{\max(V_{an}^*, V_{bn}^*, V_{cn}^*) + \min(V_{an}^*, V_{bn}^*, V_{cn}^*)}{2} \quad (3.4)$$

Figure 3.8: Dead-time on the leg a .

3.1.3 Inverter Non-Linearities

It is worth mentioning that the same leg switches cannot be in the "ON" state simultaneously to avoid the "shoot-through" failure event, causing the short-circuit of the supply with potentially catastrophic consequences on the devices. In Fig. 3.8, the introduced dead-time permits to avoid the shoot-through failure on the a -leg of the power converter where the transition from the "low" to "high" state of the power switch S_a^+ is delayed by the dead-time $t_d = 2.2\mu s$. In the same way, the transition from the "low" to "high" state of the power switch S_a^- is delayed by the same dead-time $t_d = 2.2\mu s$. Repeating the same approach on the b - and the c -leg, the shoot-through failure is avoided and the converter can operate safely. For this reason, the switching transition on the same leg is delayed by a few microseconds time intervals, known as death-time. This aspect, as well as the neglected on-state voltage drops, will not be considered in the prediction model, but it will have some impact on algorithms' performance by introducing a voltage error that needs to be either identified and/or compensated. This non-linear effect makes the voltage error dependent on the phase current. Furthermore, the voltage error increases with the dc-link voltage, the dead time, and the switching frequency. The introduc-

tion of the integral terms will show the effectiveness of the voltage error compensation without the need for further identification techniques.

3.2 SyRel Motor: Linear Model

The SyRel motor consists of the same stator winding configuration as the other conventional three-phase machines. On the other hand, the rotor is made of a highly anisotropic ferromagnetic core conveniently shaped to exploit the reluctance principle. The magnetic flux streamlines induced by the stator winding tend to shorten their path aligning and dragging the rotor to achieve the lowest energy state.

The SyRel motor can be mathematically described in several reference frames. In the stationary magnetic axis reference frame, the abc -electrical quantities such as the voltage, current, and magnetic flux are denoted with the space vector notations, where they figure as rotating vectors whose components are 120 degrees phase-shifted with each other. The stationary orthogonal axis reference frame $\alpha\beta$ is another standard representation for the electrical quantities. However, the implementation of practical control techniques with rotating vectors is not straightforward, the reason why the rotating synchronous reference frame aligned along the rotor dq axis is one of the most preferable, where the quantities can be assumed as continuous vectors. The well-known Park and the Clarke transformation matrices can be used to switch from the abc to the dq -axis reference frame.

The continuous-time SyRel motor voltage equation in a synchronous reference frame is described as follows:

$$\mathbf{v}_{dq} = R_s \mathbf{i}_{dq} + \frac{\partial \boldsymbol{\psi}_{dq}}{\partial t} + \mathbf{Q} \omega_r \boldsymbol{\psi}_{dq} \quad (3.5)$$

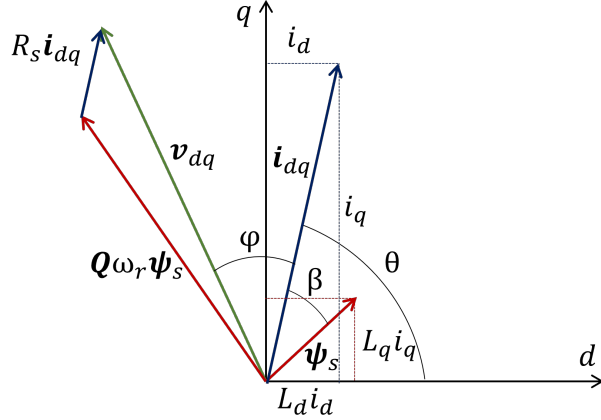


Figure 3.9: SyRel vector diagram.

In (3.5), the terms \mathbf{v}_{dq} , \mathbf{i}_{dq} , and $\boldsymbol{\psi}_{dq}$ represent the voltage, current and magnetic flux vectors, respectively. The term $\frac{\partial}{\partial t}$ is the partial derivative operator. Furthermore, the symbol R_s is the stator resistance, ω_r is the synchronous speed, while \mathbf{Q} is the orthogonal rotation matrix $\mathbf{Q} = \begin{bmatrix} 0 & -1 \\ 1 & 0 \end{bmatrix}$.

Despite the linearity assumption for SyRel motors being a strong approximation, some control design aspects can rely on the linear model for parameter identification purposes. Following the linearity hypothesis, and neglecting the iron core losses, thus assuming a conservative system with zero variation of coenergy, the d - and q -axis magnetic flux components ψ_d , ψ_q result proportional to the d - and q -axis current components i_d , i_q as follows

$$\psi_d = L_d i_d \quad (3.6a)$$

$$\psi_q = L_q i_q \quad (3.6b)$$

where L_d and L_q are the direct and quadrature inductance, respectively. The vector diagram of (3.2) is qualitatively represented in Fig 3.9, where β is the load angle between the flux and the current vectors, θ is the current angle, and ϕ represents the power factor.

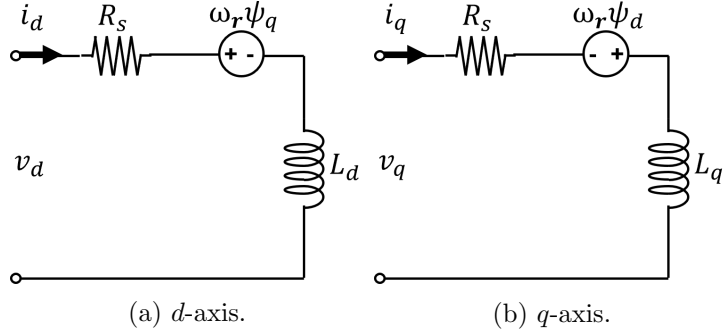


Figure 3.10: SyRel ideal equivalent circuit representation.

The equivalent circuits representing (3.5) is shown in Fig. 3.10.

The electromagnetic torque T_{em} can be evaluated as

$$T_{em} = \frac{3}{2}p(L_d - L_q)i_d i_q. \quad (3.7)$$

Under the linear model assumption and given the motor nameplate (see Table A.1), the direct and quadrature inductance can be estimated for designing a controller for preliminary tests. Given the rated voltage v_n , the rated torque T_0 at the rated speed ω_r , it can be assumed that $i_d = i_q = i_0$, where i_0 is the rated current. A linear system in L_d and L_q can be derived from the current limit circle expression (i.e., $i_d^2 + i_q^2 = i_0^2$), the voltage limit (i.e., $v_d^2 + v_q^2 \leq V_{dc}^2$) 3.1) and (3.7) as follows:

$$\begin{cases} L_d^2 + L_q^2 = \frac{2v_0^2}{i_0^2 \omega_r^2} \\ L_d - L_q = \frac{4T_0}{3pi_0^2} \end{cases} \quad (3.8)$$

A graphical interpretation of (3.8) is shown in Fig. 3.11 where the positive intersection between the two geometric logos representing the first of (3.8) by the red circle, and the second of (3.8) by the blue line, identify a feasible pair of L_d and L_q that will be used to tune the PI controllers needed for the identification tests. It is possible to notice that the resulting d -axis

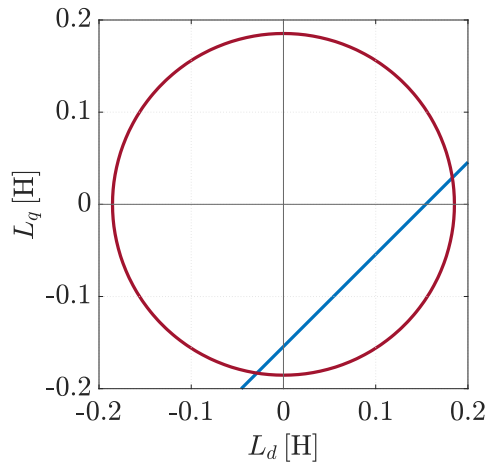


Figure 3.11: L_d and L_q estimation ($L_d = 186.4$ mH, $L_q = 32$ mH).

inductance value is higher than the q -axis component whose difference is proportional to the rated electromagnetic torque according to (3.7).

The iron losses are usually considered in the SyRel motor's equivalent circuit by adding a shunt resistor in both d - and q -axis [25]. For the case study, this effect is neglected as it does not add any significant aspect to the main goals of the work. In addition, neglecting the iron core losses is a reasonable approximation when low-speed operations (i.e., lower than the rated speed [19]) are considered.

3.3 Magnetic Model Identification Tests

A distinguishing feature of the SyRel resides in the non-linear flux versus current characteristics due to the self-axis and cross-saturation phenomena. The former shows that direct current saturates the direct flux, and the same trend can be observed in the quadrature axis. The latter consists of direct flux variations due to changes in quadrature current and vice versa. Therefore, the d - and q -flux components have to be considered as

non-linear functions of the current components i_d and i_q as $\psi_d = f_d(i_d, i_q)$ and $\psi_q = f_q(i_d, i_q)$. The saturation phenomena observed in SyRel motors make the linear control design process problematic in terms of stability and guaranteed performance in the whole operating range.

One of the most acknowledged procedures to identify the flux-versus-current maps of the SyRel motor is the one reported in [77], and it will be carried out to identify the aforementioned f_d , f_q characteristics to be included in the control. This method belongs to the constant speed identification methods and requires an appropriate current control algorithm to be implemented on the SyRel drive with accessible voltage signals. Moreover, a prime mover driven at the desired constant speed and coupled to the SyRel motor is required.

The method relies on (3.5) to evaluate the d - and q -flux for each operable point in the i_d , i_q domain, including the overload. In the case study, the current domain to be tested was from 0 to 7 A with a 0.5 A current step. The whole procedure is highly time-consuming to get viable results, as the wider the explored region, the more accurate the magnetic model result. Compared to other constant speed methods, the one here followed compensates for the stator voltage drop if the test is sufficiently short to avoid thermal effects. On the other hand, it has to be long enough to evaluate the needed signal averaged over at least a mechanical period, to eliminate any electrical or mechanical periodicity, guaranteeing the speed regulation transient to be extinguished.

As far as the rotational speed setting is concerned, the flux estimation error is minimum at high speed. On the contrary, the iron losses are not negligible at high speed. An acceptable compromise to address the core losses and the voltage vector is selecting 1/3 of the base speed.

The single test consists of applying a sequence of three current pulses to the SyRel (i_d^*, i_q^*) , $(i_d^*, -i_q^*)$, (i_d^*, i_q^*) corresponding to motor-brake-motor functioning. The symbol i_d^* denotes the d -axis current command while i_q^* denotes the q -axis current command. The first two pulses compensate for the stator voltage drop. The third pulse is given to eliminate any thermal drift due to stator resistance variation occurring during the first two pulses. The average of the voltage vector in motoring and braking modes turns out to be independent of the stator voltage drop, and other effects such as inverter losses, and dead-time voltage error are compensated.

Downstream the three-pulses test, the flux components can then be evaluated offline as follows:

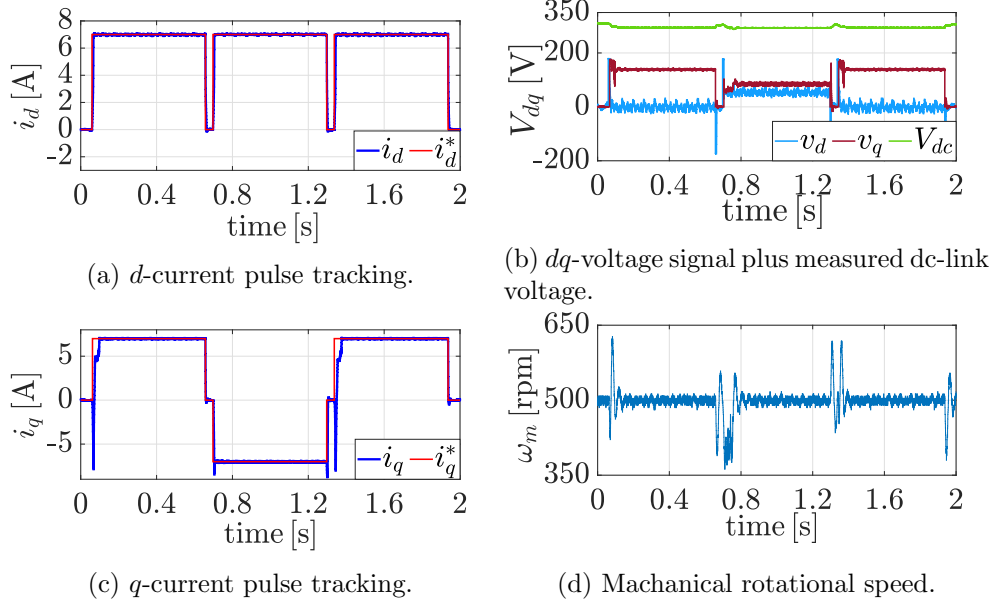
$$\psi_d = +\frac{1}{2} \frac{\frac{v_{q,1}+v_{q,3}}{2} - v_{q,2}}{\frac{\omega_{r,1}+\omega_{r,2}+\omega_{r,3}}{3}} \quad (3.9a)$$

$$\psi_q = -\frac{1}{2} \frac{\frac{v_{d,1}+v_{d,3}}{2} + v_{d,2}}{\frac{\omega_{r,1}+\omega_{r,2}+\omega_{r,3}}{3}} \quad (3.9b)$$

where $v_{d,1}$, $v_{d,2}$, $v_{d,3}$, $v_{q,1}$, $v_{q,2}$, and $v_{q,3}$ are the reference voltage signal output by the controller and averaged over two electrical periods during the three current pulses for the d - and the q -current axis, respectively. The terms $\omega_{r,1}$, $\omega_{r,2}$, and $\omega_{r,3}$ are the averaged electrical speed over the three current pulses.

The test results for a single operating point are reported in Fig. 3.12, for $i_d = 7A$, $i_q = 7A$ at $w_r = 500$ rpm. Fig. 3.12a and 3.12c shows the d - and q -current tracking over the three pulses, respectively. The voltage signals used to evaluate the fluxes are also reported in Fig. 3.12b, while the rotational speed calculated from an optical encoder signal is shown in 3.12d.

It is important to remark that no complex controller gains tuning proce-


 Figure 3.12: Experimental test for $i_d = 7$ A, $i_q = 7$ A.

dures are required for this identification procedure but the controller has to provide stable reference tracking at steady-state regardless of the transient performance in the entire current domain to be tested. The q -current overshoots noticeable in Fig. 3.12 and due to dc-link voltage occurrence and non-linear cross-coupling effect did not influence the results.

Referring to Fig. 3.12, the time interval between two consecutive tests has to be chosen in a way that the motor average temperature remains stable during the whole identification procedure selected as twice the active time.

The identified magnetic model maps f_d and f_q reported in Fig. 3.16a, and 3.16b, respectively, will be implemented as 2D look-up tables LUT to take into account of the saturation phenomena. The flux-versus-current characteristic curves given in Fig. 3.12d are obtained as a function of the self-axis and the cross-axis currents. For instance the line labeled $\psi_d(i_d, 0)$ represents the d -axis flux-linkage as function of the d -axis current when the q -axis current is zero; similarly, $\psi_d(i_d, i_q = 7$ A) gives ψ_d as a function of i_d when $i_q = 5$ A In fig. 3.13c the same flux maps are represented in 2D as

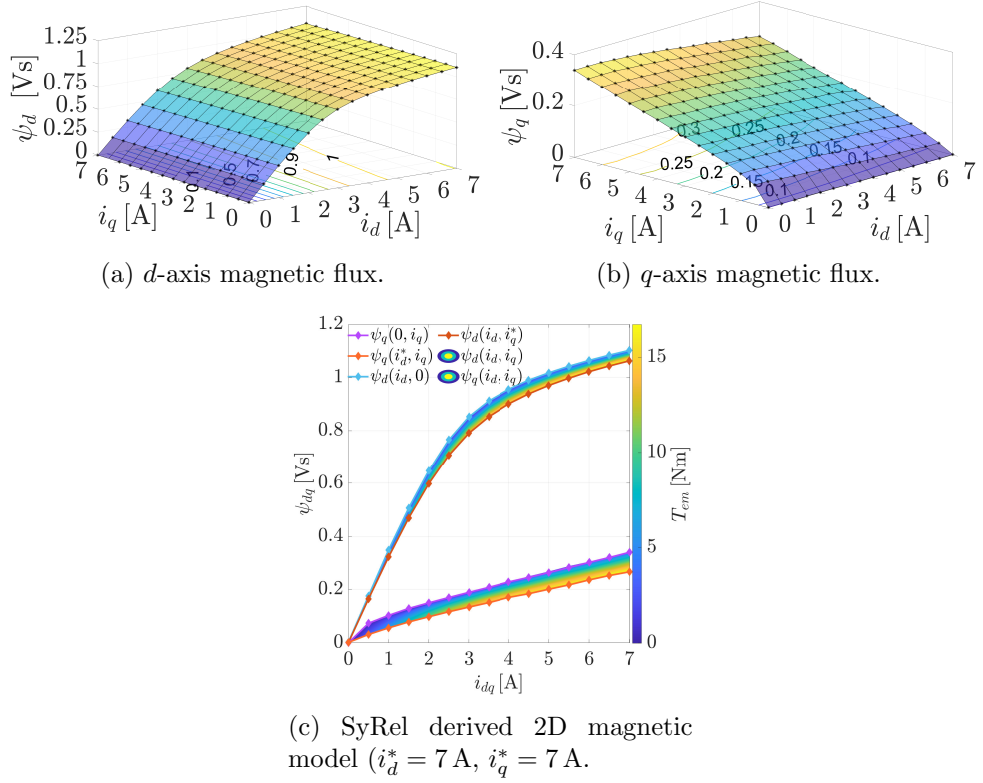


Figure 3.13: Identified magnetic model.

well as the torque contour maps.

3.4 SyRel Motor: Real Model

In this section, the results of the identified flux-versus-current maps are used to evaluate the corresponding apparent inductance and the incremental inductance matrix. Moreover, the optimum operating trajectories in the dq -current plane are also found and shown in the following.

3.4.1 Inductance Calculation

A comparison between the flux-versus-current maps in the ideal case and the real case are shown in Figs. 3.14a, and 3.14b.

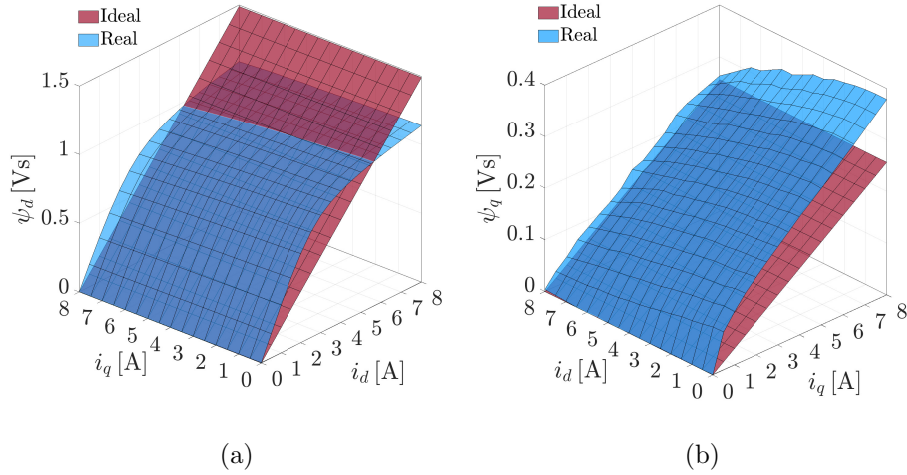


Figure 3.14: (a) Evaluated MTPW trajectory in the ψ_d, ψ_q plane. (b) Evaluated MTPW trajectory in the ψ_d, ψ_q plane.

The benefits of the experimental identification of the magnetic model reside in having the possibility to evaluate offline the motor performance (i.e., torque-versus-speed profile) with precision, and use the flux maps in model-based control implementations. In particular, the determination of the maximum torque per ampere MTPA and the maximum torque per voltage MTPV control trajectories are necessary for the full exploitation of the motor torque and speed ranges.

While the concept of self-axis saturation is widely established, the subject of cross-saturation was defined in two different ways. One considers the cross-saturation phenomenon as the saturation of portions of a magnetic circuit associated with one axis caused by the current of the other axis. The second methodology consists of the d -axis saturating the q -axis and vice versa such that each current has an action on the orthogonal axis inductance. The two approaches are equivalent and the latter will be the one considered in the following.

Given the identified flux versus current characteristics, the derivative of the magnetic flux in 3.5 can be developed assuming it as a composite function

of the current vector i_{dq}

$$\frac{\partial}{\partial t} \psi_{dq} = \frac{\partial \psi_{dq}}{\partial i_{dq}} \frac{\partial i_{dq}}{\partial t} = \mathbf{L} \frac{\partial i_{dq}}{\partial t}, \quad (3.10)$$

where the incremental (also known as dynamic or differential) inductance matrix \mathbf{L} is introduced as follows:

$$\mathbf{L} = \begin{bmatrix} L_{dd} & L_{dq} \\ L_{qd} & L_{qq} \end{bmatrix} = \begin{bmatrix} \frac{\partial \psi_d}{\partial i_d} & \frac{\partial \psi_d}{\partial i_q} \\ \frac{\partial \psi_q}{\partial i_d} & \frac{\partial \psi_q}{\partial i_q} \end{bmatrix} \quad (3.11)$$

whose components can be numerically evaluated from the fluxes linkage and the current components as

$$L_{dd} = \frac{\psi_{d+1}^q - \psi_d^q}{\Delta i} \quad (3.12a)$$

$$L_{qq} = \frac{\psi_{q+1}^d - \psi_q^d}{\Delta i} \quad (3.12b)$$

$$L_{dq} = \frac{\psi_{d+1}^{q+1} - \psi_d^q}{\Delta i} \quad (3.12c)$$

$$L_{qd} = \frac{\psi_{q+1}^d - \psi_q^d}{\Delta i}. \quad (3.12d)$$

In (3.12), the term “ Δi ” is the fixed current step corresponding to two consecutive magnetic flux points. Subscripts identify the flux map, and superscripts denote which orthogonal current a specific map is referred to. The terms L_{dd} and L_{qq} are the direct and quadrature inductance respectively, represented in Figs. 5.20b and 5.19c. The quantities L_{dq} and L_{qd} are the cross magnetization inductance, resulting in non-zero terms provided that the reciprocity condition (3.13) holds valid in a conservative system disregarding the iron losses and the incremental inductance should be symmetric.

$$\frac{\partial \psi_d}{\partial i_q} = \frac{\partial \psi_q}{\partial i_d} \quad (3.13)$$

To clarify the physical meaning of the incremental inductance matrix \mathbf{L} , it governs the transient response of the motor and does not appear at a steady state, and its components are defined as the slopes of the tangents to the flux maps to the quiescent point. As can be deduced from Fig. 3.13c, the dependence of the d - and q -flux components from the cross-coupling axis is much lower than the self-axis. The diagonal components L_{dd} and L_{qq} of the matrix \mathbf{L} result in the most significant terms describing the behavior of the SyREL motor.

The resulting apparent inductance affects the amplitude of the flux linkage and it can be calculated as:

$$L_d(i_d, i_q) = \frac{\psi_d(i_d, i_q)}{i_d} \quad , \quad L_q(i_d, i_q) = \frac{\psi_q(i_d, i_q)}{i_q}. \quad (3.14)$$

The peculiarity of the SyRel resides in how the apparent (also called static or secant) inductance differs from the incremental inductance matrix and the relation between the two concepts is given as follows:

$$L = \frac{\psi}{i} \quad , \quad L_\delta = L + i \frac{dL}{di} \quad (3.15)$$

where L_δ denoted the incremental inductance term and the components are

$$L_{dd} = L_d + i_d \frac{\partial L_d}{\partial i_d} \quad (3.16a)$$

$$L_{dq} = i_q \frac{\partial L_d}{\partial i_q} \quad (3.16b)$$

$$L_{qd} = i_d \frac{\partial L_q}{\partial i_d} \quad (3.16c)$$

$$L_{qq} = L_q + i_q \frac{\partial L_q}{\partial i_q} \quad (3.16d)$$

are valid when the iron core losses are negligible. The apparent induc-

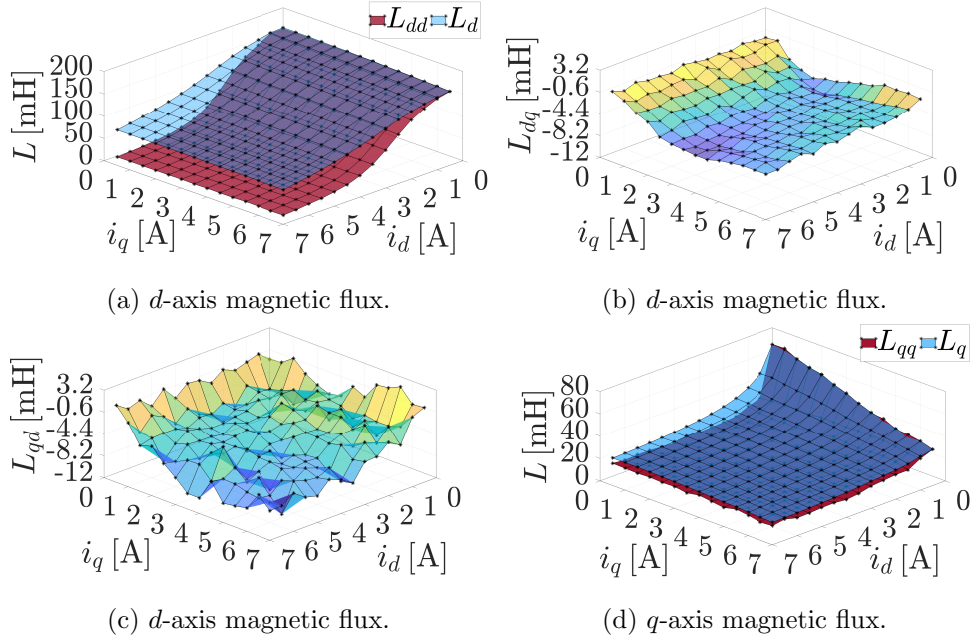


Figure 3.15: Identified magnetic model.

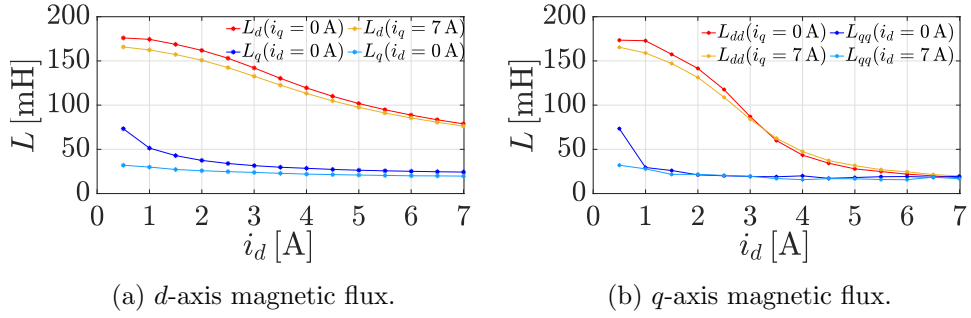


Figure 3.16: Identified magnetic model.

tance is defined as the slope of the line from the origin of the axis to the quiescent point. The two inductances are almost identical near the origin of the axis. They are equal when the SyRel is considered ideal. In general, the apparent inductance is greater than the incremental inductance. Furthermore, acknowledging the negligible iron losses, the cross-coupling inductance components are equal. The peculiarity of the SyRel resides in the difference between the direct and the quadrature inductances terms L_{dd} , L_{qq} , respectively, to produce the electromagnetic torque. Moreover, the coupling inductance terms L_{dq} , L_{qd} are non-zero and are equal when the iron losses can be neglected at low-speed operations.

3.4.2 Maximum Torque Per Ampere Trajectory

Given the flux-versus-current maps in the i_d, i_q plane, the steady-state performance can be evaluated, and several trajectories can be comprehensively identified. These trajectories shall be considered for the drive's operations below and above the base speed to achieve lower power losses. The MTPA trajectory is usually selected for operations below the base speed to minimize the stator winding losses. The current vector with the minimum magnitude for a given electromagnetic torque is the one that meets the MTPA criterion. When the inductances of the SyRel are assumed constant, the MTPA trajectory results in the stator current angle θ equal to 45 electrical degrees or, equivalently, the direct and quadrature components of the stator current in the rotor-oriented reference frame must be such that $i_d = i_q$. However, due to the high saturation of the iron core, the resulting MTPA trajectory presents a slightly different behavior. It can be identified offline seeking the current vector that minimizes the electromagnetic torque. The determined flux-versus-current maps are used to identify the MTPA. Any error in estimating those parameter influence the correctness of the optimum operating point [78]. The procedure adopted in this work consists of evaluating the electromagnetic torque T_{em} for each point tested in the current domain

$$T_{em} = \frac{3}{2}p (\psi_d i_q - \psi_q i_d). \quad (3.17)$$

The resulting three-dimensional surface is shown in Fig. 3.17. The MTPA can be identified by considering the contour plots of the calculated torque T_{em} . Each contour plot depicted in blue in Fig. 3.18b represents the constant torque geometric boundaries. Considering a defined torque level, the MTPA coordinates can be identified by finding the nearest i_d and i_q

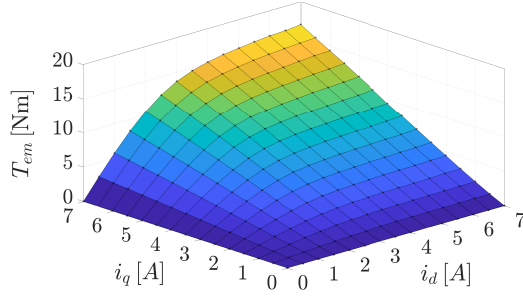
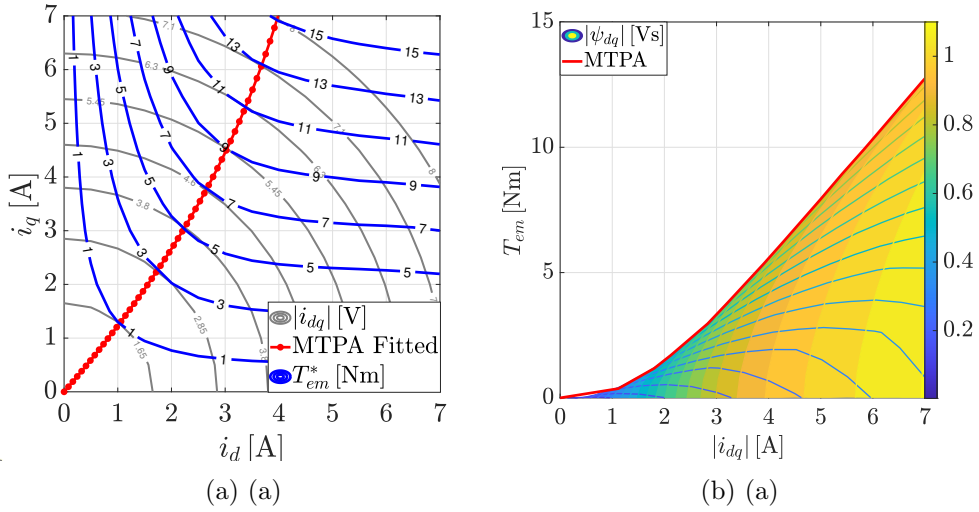


Figure 3.17: Evaluated 3D torque surface.


 Figure 3.18: Evaluated MTPA trajectory in the (a) i_d, i_q plane and (b) $|i_{dq}|, T_{em}$ plane.

coordinates to the origin of the axis. Repeating the procedure for all the torque levels, the MTPA is fully determined. It can be observed how the slope of the MTPA progressively increases (see red line in Fig. 3.18b). The maximum torque for each current magnitude level is determined for current angles greater than 45 deg. The achieved MTPA reflects the effect of the saturation phenomena described above, and it holds until the voltage saturation limit is reached.

The same result can be observed by representing the same constant torque curves in the $(\angle \mathbf{i}_{dq}, |\mathbf{i}_{dq}|)$ plane, the minimum current magnitude points are found for angles greater than 45 deg. The higher the torque and the current magnitude, the more the real system differs from the ideal case

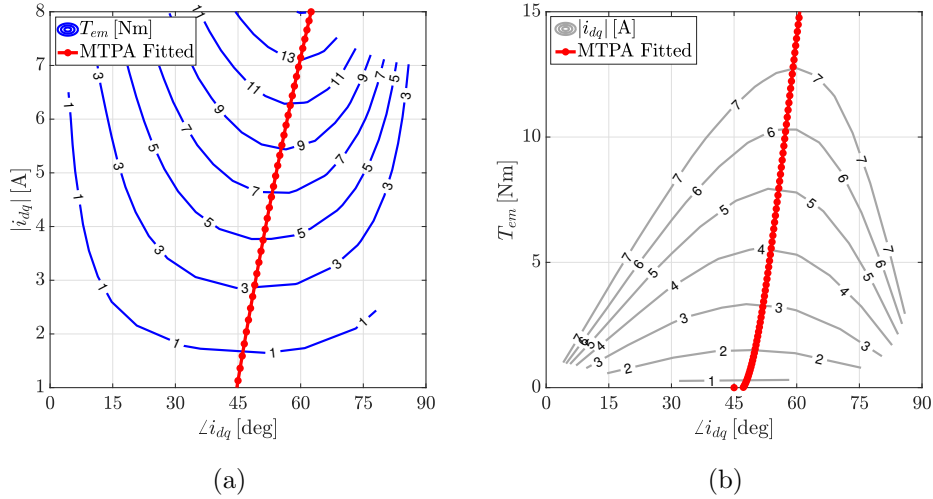


Figure 3.19: Evaluated MTPA trajectory in the (a) $\angle i_{dq}$, $|i_{dq}|$ plane and (b) $\angle i_{dq}$, T_{em} plane.

($\angle i_{dq} = 45$ deg, see Fig. 3.19a). Another way to see the same trend can be observed in Fig. 3.19b where the constant current magnitude curves are represented in the $(\angle i_{dq}, T_{em})$ plane.

3.5 Chapter Conclusions

In this section, the simplified model of the SyRel motor was described. Based on this simplified model, a standard control technique based on PI controllers has been designed to control the SyRel motor over a predefined operating range allowing the implementation of a standard procedure to estimate the SyRel motor's magnetic model.

The implemented method consisted of running the SyRel motor at constant speed such that the iron loss effects could be neglected. Positive and negative current setpoints were set in a way to make the stator resistance and inverter non-linearity effects negligible. In this way, the flux-versus-current maps could be accurately identified, enabling the estimation of the MTPA and the inductance matrix. The model-based controllers' implementations

described in the following chapters relied on the identification procedure described in this chapter.

Chapter 4

FCS-MPC: Case Study

In this chapter, the working principle of the FCS-MPC applied to a SyRel driven by a 2L-VSI will be derived. It is based on an integer quadratic optimization problem consisting of

1. measuring and/or estimating state variables.
2. Predicting the state variables at the next time step for each feasible actuating variable.
3. Evaluating a predefined cost function for each prediction.
4. Selecting the actuating variable that minimizes the cost function.
5. Applying the new switching state to control the system at the desired operating point.

In its standard formulation, the FCS-MPC shares the same features with proportional controllers (i.e., the presence of setpoint offsets) but with a faster dynamic response. Given the model-based nature, the reference tracking performance is affected by model parameter mismatches due to

poor model identification, or parameter variations during functioning. Identification procedures as well as the selection of the controller's set of parameters can guarantee the best achievable performance.

The set of parameters necessary to design a FCS-MPC is described in the sequel of this chapter aimed at enhancing the controller performance.

4.1 FCS-MPC Design Parameters

The control goals can be fulfilled by the FCS-MPC given a set of definitions and parameters that have to be selected by the control designer, affecting both the computational complexity and the expected performance.

- The most essential element is the description of an accurate discrete mathematical model to predict the system behavior for each actuating variable.
- The sampling interval is another fundamental controller parameter defined as the rate at which the controller executes the algorithm. If it is selected too large, when a disturbance occurs, the controller will not readily react to the disturbance. Smaller sampling rates enable fast reactions to setpoint changes despite the higher computational load. The recommendation is to set from ten to twenty times the rise time of the open-loop system's response to achieve the right balance between performance and computational effort [79].
- The prediction horizon is defined as the number of predicted future time steps, and it represents how far the controller predicts into the future. The prediction horizon has to be set according to the system's dynamics and the hardware's limitations. Fig. 4.1 graphically

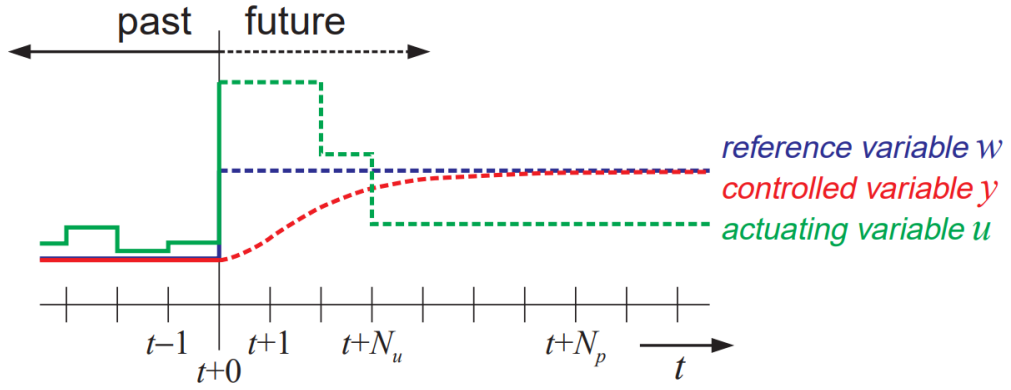


Figure 4.1: Definition of the control and prediction horizon taken from [2].

shows the prediction horizon in the time domain with respect to the prediction of the system behaviour till the prediction horizon N_p .

- The control horizon is another important design parameter. It is defined as the number of future control actions leading to the predicted plant output. A higher control horizon enables more accurate predictions at the cost of increased complexity. The control horizon could be selected the same as the prediction horizon, however, usually only the first couple of control moves have a significant effect on the predicted output behaviour to disturbances, while the remaining moves have only a minor effect. This aspect can be noticed in Fig. 4.1 with N_u representing the control horizon. Therefore, choosing large control horizon only increases computational complexity. Therefore, the benefit of considering two or three steps control horizon results in better predictions [44].
- The core of the FCS-MPC algorithms resides in the definition of the cost function. It is defined as a scalar non-negative aimed at selecting the best actuating variable to accomplish multiple control targets. Several types of cost functions can be selected in terms of the norm used for the stage cost. The FCS-MPC can incorporate hard or soft

constraints on the inputs and outputs, respectively. Unlike hard constraints, soft constraints can be violated and they are introduced to meet specific system requirements. Combinations of hard and soft constraints on inputs and outputs allow the system to respond to setpoint changes without violating the system limitations. With the objective function, the system model, and hard and soft constraints, the optimization problem is solved in real time to find the best actuation to accomplish the control objectives.

- As FCS-MPC has multiple goals, a way to achieve balanced performance between these competing goals is to weigh the input rates and output relative to each other. A larger weight prioritizes the control action toward certain states.

In the case study, the sampling time was set to execute the control algorithm in real-time (i.e., from 10 to 48 kHz) according to the available hardware (see Appendix A). Furthermore, one step or a sampling rate is considered for the prediction and the control horizons.

4.2 Predictions

As stated above, one of the main steps of predictive controllers consists of predicting the future behavior of the system according to its mathematical model, its current state, and the feasible input actuation. The SyRel drive model was represented in the synchronous reference frame (dq coordinates) rotating at the electrical speed ω_r , where the quantities can be assumed as constant vectors in a reference frame. When the time execution for the control algorithm is smaller than the sampling interval, the one-step-ahead prediction can be considered for the prediction calculation [79]. As the

control algorithm will be implemented on a DSP, the discrete-time model of the drive is derived in (4.1) by employing the forward Euler discretization to (3.5).

$$\mathbf{i}_{dq}^{k+1}(n) = \mathbf{i}_{dq}^k + T_s \mathbf{L}^{-1} [\mathbf{v}_{dq}(n) - R_s \mathbf{i}_{dq}^k + \mathbf{Q} \omega_r \boldsymbol{\psi}_{dq}] \quad (4.1)$$

It considers the identified flux versus current maps (see Fig. 3.13c) and the subsequently derived inductance matrix (3.12). On the left-hand side of (4.1), the term $\mathbf{i}_{dq}^{k+1}(n)$ indicates the current prediction at the next time step (i.e., superscript $k + 1$) calculated for each feasible switch positions (i.e., $n = 0, 1, 2, \dots, 7$) of the 2L-VSI. On the right-hand side, T_s is the sampling interval between two consecutive time steps, the term $\mathbf{v}_{dq}(n)$ is defined in (3.2), whereas the term \mathbf{i}_{dq}^k is the measured current vector at the actual time step (i.e., superscript k). The symbols for the magnetic flux vector and the inverse of the differential inductance matrix are $\boldsymbol{\psi}_{dq}$ and \mathbf{L}^{-1} , respectively, both assumed as functions of the current vector. Acknowledging the controller's sensibility versus model mismatches, the flux, and the inductance matrix terms are assumed as functions of the current, whose characteristics are derived experimentally and shown in Figs. 3.13c and 3.15. The self-axis and cross-saturation phenomena are highlighted and taken into account by storing the identified characteristic in 2D LUTs.

4.3 Cost Function

This section is dedicated to the design choice of the cost function, defined as a scalar, non-negative measure of the controller performance. The choice of modifying the standard 2-norm cost function is motivated by reaching higher performance as shown in Chapter 5. In particular, the introduction

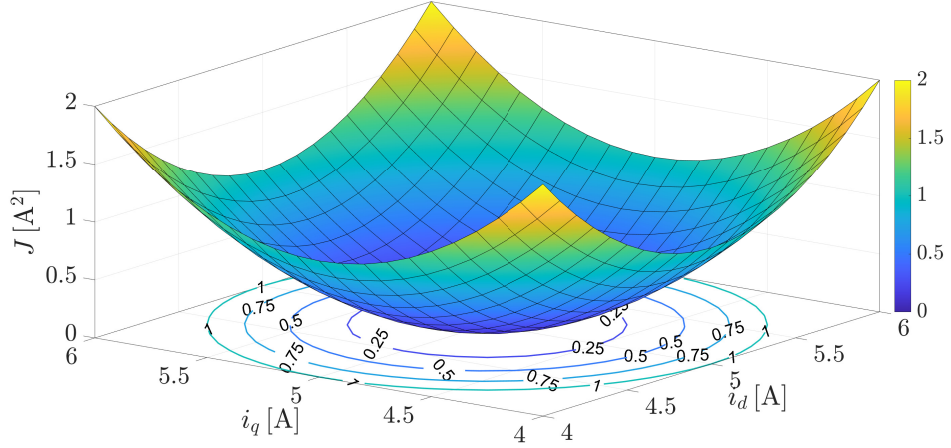


Figure 4.2: Cost function graphical interpretation.

of integral of the error terms in the tracking terms allows to achieve higher robustness versus parameters variations. Furthermore, the introduction of a control effort weighting factor enables lower current distortions.

4.3.1 Current Tracking Terms

In electric drives application, the most commonly defined cost function $J_1(n)$ includes reference tracking terms defined as the sum of the (squared) 2-norm of the current errors as follows:

$$J_1(n) = \lambda_i \left\| \mathbf{i}_{dq}^* - \mathbf{i}_{dq}^{k+1}(n) \right\|_2^2 \quad (4.2)$$

where i_d^* , i_q^* are the current reference components of the current reference vector \mathbf{i}_{dq}^* . $i_d^{k+1}(n)$ and $i_q^{k+1}(n)$ are the predicted current components of the current prediction vector $\mathbf{i}_{dq}^{k+1}(n)$ at the next time step $k + 1$ for the eight configurations that the 2L-VSI can assume (i.e., $n = 0, 1, 2, \dots, 7$, see Tab. 3.1). A graphical representation of the cost function is illustrated in Fig. 4.2. It shows the 3D trend of the i_d and i_q versus the cost function

$J(n)$, proving the existence of a minimum of $J(n)$ given the current references (e.g. $i_d^* = i_q^* = 5$ A). The symbol $\lambda_i = \begin{bmatrix} w_d & 0 \\ 0 & w_q \end{bmatrix}$ denote a diagonal matrix whose components w_d and w_q are non-negative d - the q -current reference tracking term weighting factors aimed to set the relative importance between the two output variables. The term w_d penalizes the predicted deviation of the d -current component at time step $k + 1$. Similarly, the term w_q penalizes the predicted deviation of the q -current component from its reference at time step $k + 1$. Both terms are penalized quadratically and by appropriately tuning the weights in the cost functions, a large degree of similarity between the two controllers can be achieved. The search for the optimum control action converges to the minimum of the 3D surface, where the reference tracking error is an absolute minimum. The controller will provide the control action such that the minimum of $J(n)$ is reachable in a finite-step interval. The level sets of the (convex) cost function are ellipsoidal. This implies that for an equally good tracking of the multiple objectives (on the d - and q -axis), the weighting factor selection in the cost function is required to turn the level sets into circular ones. [80] shows that for predictive current control, the common choice of equal weights on the two orthogonal current components minimizes the current distortions.

The control act proactively to achieve fast dynamic response. However, if the prediction are mistaken, the system responds with a steady-state error between the reference and the prediction, thus the actual feedback. The switching configuration that minimises (4.2) at the next time step is selected and applied.

In the context of power electronics, the 2-norm of a ripple variable is proportional to its Total Demand Distortion (TDD) [81]. Therefore, minimizing the output tracking error is akin to minimizing the TDD of the output

variables. This implies that better tracking performance is achieved when the 2-norm is used. Furthermore, When the 2-norm is used, a wide range of switching frequencies are achieved. The highest switching frequency occurs when the control effort weighting factor λ_u defined in the sequel is zero and, thus, depends only on the chosen sampling interval. By doing so, practical closed loop stability, favorable tracking performance and comparatively low distortions are ensured. Low current TDDs imply low torque TDD [81]. The most common pitfall, namely a poorly chosen norm is discussed, which can lead to suboptimal performance or even instability. It is computationally cheaper when the 1-norm instead of the 2-norm is used. Therefore, from a computational perspective, the adoption of the 1-norm in FCS-MPC seems to be preferable, particularly in light of the fact that the MPC algorithm has to be executed in real time within a few tens of microseconds. On the other hand, the 1-norm can result in a performance deterioration as well as closed-loop instability. Besides the stability issues incurred by the use of the 1-norm a limited range of switching frequencies as well as performance degradation are among the direct consequences of such a design choice [80]. The choice of norm has a profound impact on the closed loop system performance when MPC with reference tracking is employed. Despite the common belief that an objective function with the 1-norm is preferable for computational simplicity, the 1-norm is a poor choice. Operation at low switching frequencies is impaired, tuning is difficult and stability issues arise. The (squared) 2-norm avoids these issues and is thus clearly preferable. In particular, the 2-norm guarantees closed-loop stability [80].

4.3.2 Integral Terms Inclusion

The accuracy of the prediction model is critical to the effectiveness of the controller because the FCS-MPC essentially behaves as a proportional controller. As a result, any existing model inconsistency might amplify potential reference tracking problems. An efficient approach will be adopted to tackle this issue, i.e., by incorporating an integrating element into the cost function to compensate for any model inaccuracy and so the steady-state errors. The integral of the error are embedded within the (squared) 2-norm term to make it dependent on the actuating commands (n) thanks to the cross-product. The cost function defined in (4.2) is modified as follows:

$$J(n) = \left\| \mathbf{i}_{dq,err}^{k+1}(n) \mathbf{W}_{dq} T_s \left(\sum_{j=1}^{\ell} \mathbf{i}_{dq,err}^{k-j} + \mathbf{i}_{dq,err}^k \right) \right\|_2^2 \quad (4.3)$$

where the prediction errors at the next time step $k + 1$ are defined as

$$\mathbf{i}_{dq,err}^{k+1}(n) = \mathbf{i}_{dq}^* - \mathbf{i}_{dq}^{k+1}(n) \quad (4.4)$$

while the error at the current error at step k , i.e., $i_{d,err}^k, i_{q,err}^k$ is:

$$\mathbf{i}_{dq,err}^k = \mathbf{i}_{dq}^* - \mathbf{i}_{dq}^k \quad (4.5)$$

The integrals of the current errors are evaluated at every sample j where ℓ is the number of samples. The terms $\mathbf{i}_{dq,err}^{k-j}$ are the previously calculated integral of the errors. \mathbf{W}_{dq} is a diagonal matrix whose nonzero entries are the two gains tuned in a trial-and-error fashion. Even though the addition of the integral term will unavoidably add a computational overhead to the proposed FCS-MPC method, it is still computationally cheaper than other existing methods. For example, one of the approaches found in literature is based on augmenting the system state (see, e.g., [51]). This implies that the

amount of required calculations increases significantly as the dimension of the state-update function increases i.e., (3.5) would need to be adapted to account for the augmented state, and more computations to be performed accordingly. Another approach, i.e., the approach proposed in [3] (see Section V in [3]) considers an additional term in the cost function that depends on the error between the reference and the predicted currents. This means that (3.5) needs to be adjusted to account for this error, while a numerical integration needs to be performed. In contrast to the above, with the approach proposed in this work, the integration is neither dependent on the prediction, nor requires an augmented state. It simply requires a few algebraic operations on each axis of the dq coordinate system, as explained in the following:

- two subtractions, i.e., $i_{d,err}^k = i_d^* - i_d^k$, and $i_{q,err}^k = i_q^* - i_q^k$;
- two multiplications, i.e., $T_s \cdot i_{d,err}^k$, and $T_s \cdot i_{q,err}^k$;
- two additions, i.e., $T_s \cdot i_{d,err}^k + i_{d,err}^{k-1}$, and $T_s \cdot i_{q,err}^k + i_{q,err}^{k-1}$;
- finally the values obtained from the last operation have to be added to the reference tracking term.

From the above, it can be concluded that when comparing the proposed approach with the ones described in [3] and [51], less calculations are required. The integral error term can effectively compensate for mismatches in L_d and L_q , and thus ensure a zero steady-state error. In this respect, the use of a magnetic model may look redundant. Nevertheless, such a model is necessary to determine the the incremental inductance matrix \mathbf{L} in (3.5). If this matrix is not correctly identified, higher current ripples are typically produced, thus deteriorating the quality of the current (i.e., higher current distortions). This point was also discussed in Section III-B of [71] in which

the errors introduced in the values of the incremental inductances lead to errors in the values of the predicted currents for instant $k + 1$ but they do not affect the motor steady-state tracking capability of the reference values set by the control system. The sole effect of incremental inductance errors as high as 40% is the increase of current and torque ripples, without affecting the steady-state performance of the drive system.

Overall, the presented control method can achieve favorable system performance, as clearly demonstrated with the presented experimental results, while the modest increase in the computational demands did not hinder its real-time implementation. Hence, the improved steady-state performance and increased robustness to parameters mismatches outweigh any potential disadvantages due to the somewhat increased computational burden. It is also worth mentioning that such inclusion did not deteriorate the system's dynamic response. As shown in Sect. 5, in the presence of model inaccuracies, the integral terms act as model-free compensators for adjusting setpoint offsets.

4.3.3 Control Effort Inclusion

FCS-MPC restricts switching transitions to the discrete-time instants. The low sampling-to-switching-frequency ratio, known as the granularity of switching, unduly restricts the switching instants of FCS-MPC to a coarsely sampled time axis. On the other hand, a high sampling-to-switching-frequency ratio allows FCS-MPC to switch at approximately any moment in time, and, thus, effectively in the continuous-time domain. This results in a fine granularity of switching. The control effort term penalizes the change in the switch position, allowing to lower the average switching frequency, getting a more favorable granularity of switching, thus permitting

operation in a quasi-continuous time domain, and achieving lower current distortions [44]. High granularity of switching is achievable by penalizing the control effort as well as increasing the sampling interval, thus ensuring competitive steady-state performance.

The control effort factor is defined as:

$$\Delta \mathbf{S}(n) = \mathbf{S}_{abc}(n) - \mathbf{S}_{abc}^{k-1} \quad (4.6)$$

The term $\mathbf{S}_{abc}(n) = [S_a(n) S_b(n) S_c(n)]^T$ is evaluated for each configuration of the 2L-VSI ($[0,0,0]$, $[1,0,0]$, \dots $[1,1,1]$), while \mathbf{S}_{abc}^{k-1} is the three-phase switch position applied at the previous time step $k - 1$. The values that the control effort factor $\Delta S(n)$ can assume are listed in Table 4.1.

The control effort term is introduced in the cost function as follows

$$J(n) = \left\| \mathbf{i}_{dq,err}^{k+1}(n) + \mathbf{W}_{idq} T_s \left(\sum_{j=1}^m \mathbf{i}_{dq,err}^{k-j} + \mathbf{i}_{dq,err}^k \right) \right\|_2^2 + \lambda_u \|\Delta \mathbf{S}(n)\|_2^2 \quad (4.7)$$

To achieve a fine granularity of switching, the weighting factor $\lambda_u > 0$ is added. Conventional FCS-MPC does not include the control effort penalization, or equivalently $\lambda_u = 0$. The unconstrained (i.e., relaxed) solution of the optimization problem results in a quantized deadbeat controller. This implies that the switching frequency is not directly controlled, but merely limited by the sampling frequency which defines a theoretical upper limit $\bar{f}_{sw} = f_s/2$. As a consequence, conventional FCS-MPC achieves poor granularity of switching, which has a negative impact on the drive performance, as indicated in the next section. Hence, the aim is to have as high sampling frequencies as possible and tune λ_u such that the average switching frequency is reduced, and, consequently, fine granularity of

switching is achieved. Thanks to contemporary microprocessors that come with high computational power and low costs, a cost-effective real-time implementation of the proposed FCS-MPC approach is feasible.

Table 4.1: Control effort list of values for each configuration change.

n	0	1	2	3	4	5	6	7
0	0	1	2	1	2	1	2	3
1	1	0	1	2	3	2	1	2
2	2	1	0	1	2	3	2	1
3	1	2	1	0	1	2	3	2
4	2	3	2	1	0	1	2	1
5	1	2	3	2	1	0	1	2
6	2	1	2	3	2	1	0	1
7	3	2	1	2	1	2	1	0

Tradeoff between the tracking accuracy (i.e., the deviation of the output variables from their references) and the switching effort (i.e., the switching frequency), whereas—for sake of simplicity—the output errors equally prioritized the tracking error cost, which depends linearly on the current error. When the (squared) 2-norm is used in the cost function, the tracking error cost changes quadratically with the current error. The switching cost dominates over the tracking error cost. The difference between the predicted squared current errors for the various switching states exceeds the switching cost, then a switching transition occurs from the past time interval $k - 1$ and the current time interval k to reduce the current error. Consequently, closed-loop stability is ensured [80]. When the switching cost outweighs the relative reduction in the tracking error, then switching is avoided regardless of the absolute tracking error. As a result, the current error increases, the controller tracking performance deteriorates and stability issues arise. As a rule of thumb, the sampling frequency should be about two orders of magnitude higher than the resulting switching frequency [82]. To achieve high sampling frequencies, control platforms based on field-programmable gate arrays (FPGA) are well suited, because operations can be highly pipelined

and parallelized.

4.3.4 Prediction Saturation

Another term defined in (4.8) can be added in the cost function to secure the drive functioning within certain current magnitude boundaries.

$$g_{sat} = \begin{cases} 0 & \text{if } \sqrt{[i_d^{k+1}(n)]^2 + [i_q^{k+1}(n)]^2} \leq i_{sat} \\ \infty & \text{if } \sqrt{[i_d^{k+1}(n)]^2 + [i_q^{k+1}(n)]^2} > i_{sat} \end{cases} \quad (4.8)$$

where i_{sat} is the maximum current tolerated by the drive. In this way all the actuating variables that predicts current over the imposed threshold are discarded resulting in similar way as the saturation scheme for standard controllers.

4.4 Chapter Conclusions

In this chapter, a detailed overview of the design choices for the implementation of the FCS-MPC is reported. The accuracy of the mathematical model used to predict the system's behaviour is of paramount importance. Furthermore, the classical formulation of FCS-MPC has been improved by introducing integral terms to increase the system robustness versus parameters' mismatches. Finally, the choice of introducing a control effort weighting factor to reduce the current distortions has been described. Thanks to these design choices, it will be shown how the classical formulation of FCS-MPC can be easily outperformed.

Chapter 5

FCS-MPC: Simulation and Experimental Results

In this section, simulation and the experimental results of the proposed FCS-MPC scheme applied to SyRel motor driven by a 2L-VSI are shown. The block diagram of the FCS-MPC method is presented in Fig. 5.1. It is assumed that the SyRel motor is driven by a prime mover and controlled in the current control mode. Two of the phase current components i_b and i_c and the rotor angle θ_r are measured and used to predict the system's behavior at the next time step $k + 1$ for each feasible actuating command (n) according to (4.1). Given the actual d - and q -current components (i.e., i_d^k and i_q^k), as well as the d - and q -current reference signals (i.e., i_d^* and i_q^*), the cost function defined in (4.7) is evaluated for all the feasible voltage vectors, and the one that minimises (4.7) is selected and the corresponding gate signals S_g are sent to the 2L-VSI.

The steady-state performance metrics adopted here to evaluate the effectiveness of the proposed FCS-MPC algorithm are the average switching frequency \bar{f}_{sw} , and the current total demand distortion (TDD_{*i*}), shown in

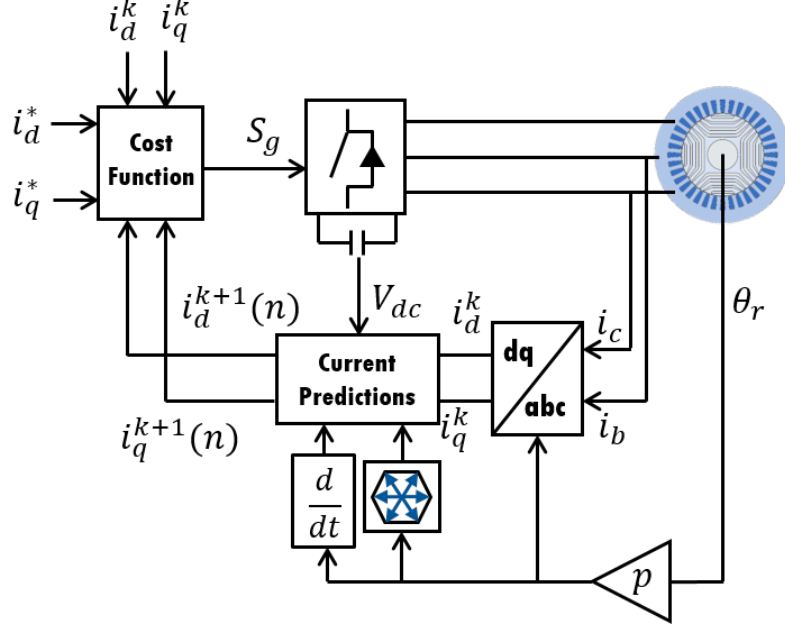


Figure 5.1: Block diagram of FCS-MPC for a SyRel Motor drive.

the equations below:

$$\bar{f}_{sw} = \lim_{\ell \rightarrow \infty} \frac{1}{\nu \ell T_s} \sum_{z=0}^{\ell-1} \|\Delta \mathbf{S}_{abc}(z)\|_1 \quad (5.1a)$$

$$\text{TDD}_i = \frac{\sqrt{\sum_{n \neq 1} i_n^2}}{I_n} \quad (5.1b)$$

Above, in the definition of f_{sw} , ℓ is the number of samples, and ν is the number of power switches of the used converter, which are six for a 2L-VSI. The estimation of the average switching frequency in real time presents some issues. The instantaneous switching frequency pattern over time corresponds to a non-casual finite impulse response filter. The average computation as presented in (5.1a) suffers the limit of having finite storage constraints and the impossibility to implement such a non-causal filter in real-time. In [83], the switching frequency is computed online utilizing an infinite impulse response filter and considered as a controllable state variable. In a similar approach, in this thesis, a low-pass filter LPF is introduced to calculate online the moving average switching frequency (5.1a). The mean value is

post-processed and computed over an integer number of electrical periods. The reason behind the use of a LPF is justified by the fact that communication issues might occur during real-time acquisition between the control platform and the host computer, especially at high sampling frequencies, forcing to down-sample of the data to facilitate the acquisitions. The same approach was considered in simulations.

Regarding the TDD_i definition is well established that the reference tracking terms in (4.7) are proportional to the current distortion, thus it is calculated by taking into account the energy spread over all harmonics except for the fundamental. The denominator is based on the rated current I_n . The TDD_i is also calculated in a post-processing stage over an integer number of electrical periods and averaged over the three phases. An alternative measure of the current distortions is the total harmonic distortion (THD). This is defined as:

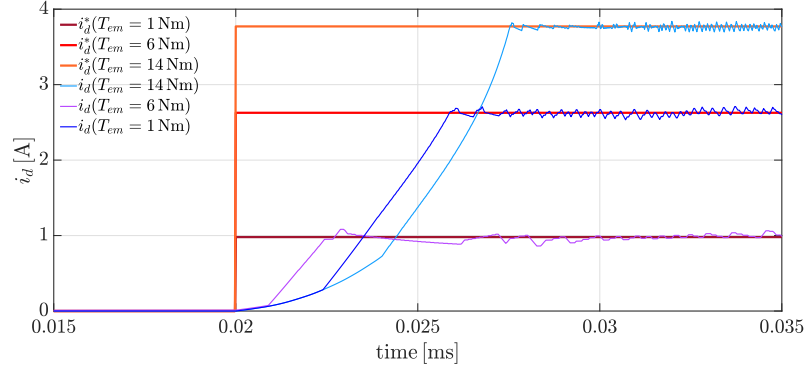
$$THD_i = \frac{\sqrt{\sum_{n \neq 1} i_n^2}}{i_1}. \quad (5.2)$$

As can be observed, the nominator of the current (THD) expression is the same as that of the TDD_i (see (5.1b) and (5.2)), but the denominator of the (THD) accounts for the amplitude of the fundamental current (i.e., i_1). As a result, when the current is low the THD tends to infinity, while the TDD_i remains approximately constant. Moreover, the practical impact of current harmonics is mostly independent of the actual current (i.e., the fundamental). For these reasons, the TDD_i rather than the THD was chosen to assess the quality of the output current.

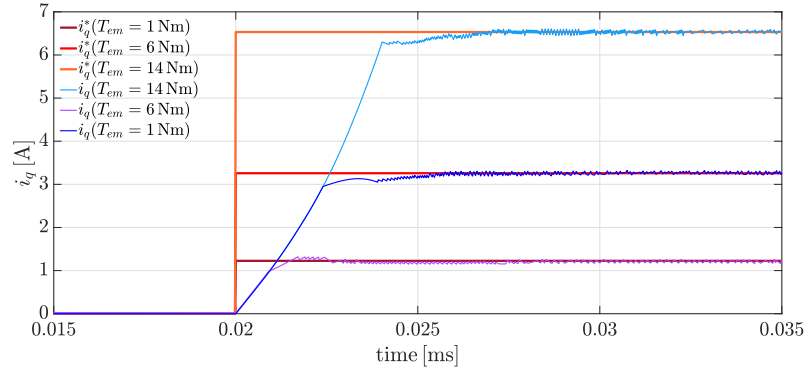
5.1 FCS-MPC Simulation Results

The simulation results are presented by taking into account the real flux-versus-current characteristics and the resulting apparent and incremental inductance described in Sect. 3.3. The identified magnetic model was considered in the model of the SyRel motor and included as LUTs such that the current prediction can perfectly match the plant. The 2L-VSI model is based on (3.1), and the dead-time effects are neglected. The disturbance introduced by the dead-time effect of the 2L-VSI is tackled by the introduction of the integrating terms. One of the main reasons why the use of FCS-MPC with a SyRel motor is beneficial over linear controllers resides in how the dynamic performance is independent of the operating point. Standard PI controllers need an accurate evaluation of the controller gains to guarantee the desired performance and stability margins over the whole operating region. In Fig. 5.2, it is shown how the dynamic performance achieved by employing the FCS-MPC with a classical formulation of the cost function such as in (4.2) does not change by moving the operating point. In fact, the achieved d - and q -axis step responses performed at constant speed (i.e. $\omega_r = 400$ rpm) present identical trends. Three different operating points corresponding to three different level of electromagnetic torque according to the trajectory (i.e., $T_{em} = 1$ Nm, $T_{em} = 6$ Nm, $T_{em} = 14$ Nm) were considered. Being the quadrature inductance lower than the inductance on the d -axis, the q -axis step response (see Fig. 5.14d) is typically faster than the d -axis behavior (see Fig. 5.14d). It can also be observed how the d -current tracking starts tracking the reference command slowly until when the corresponding q -axis current is unsettled.

In the following, firstly, an explanation of the switching frequency calculation is given. Secondly, the inclusion of the integrating terms will be



(a)



(b)

Figure 5.2: FCS-MPC dynamic performance comparison ($f_s = 48$ kHz, $\omega_r = 400$ rpm, $V_{dc} = 300$ V)(a) d -current tracking. (b) q -current tracking.

assessed with a sensibility analysis over a few parameter variations. Follows the investigation of the impact of the control effort weighting factor on the controller steady-state performance. Finally, the operating conditions such as the current, and the rotational speed are changed to observe how the performance varies over the operating domain.

5.1.0.1 Switching Frequency Calculation

The switching frequency is the first key metric used to evaluate the performance of the FCS-MPC. Its computation will be here described through simulation results achieved by setting the controller in current-control mode at a constant speed. Referring to the control scheme illustrated in Fig. 5.1, the d - and the q -current components are controlled at 1 A, while the speed

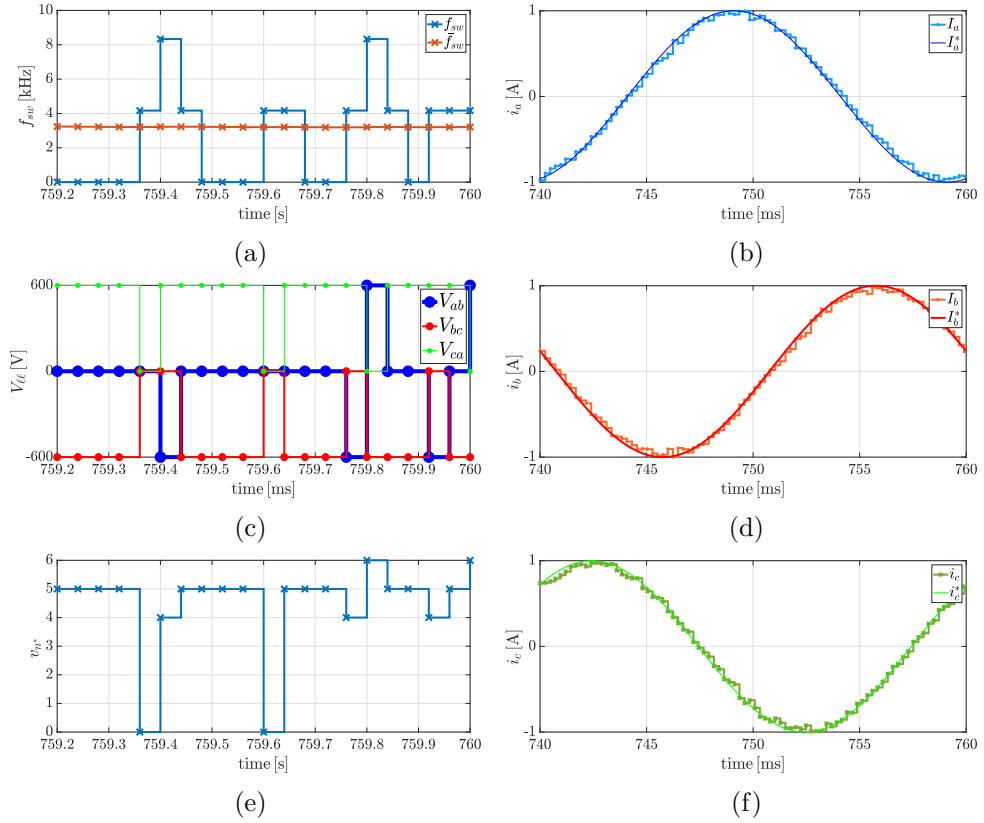


Figure 5.3: Switching frequency calculation. (a) Switching frequency. (b) a -phase current tracking. (c) Switching state. (d) b -phase current tracking. (e) Optimum vector. (f) c -phase current tracking.

was kept constant at 1500 rpm by the prime mover. The instantaneous switching frequency was calculated over time as follows:

$$f_{sw} = \frac{[S_a(n^*) - S_a(n^-)]^2 + [S_b(n^*) - S_b(n^-)]^2 + [S_c(n^*) - S_c(n^-)]^2}{\nu T_s} \quad (5.3)$$

In (5.3), S_a , S_b and S_c stand for the switching states on the leg "A", "B", and "C", respectively. The value of S_a , S_b , and S_c are logic variables set to "high" to enable the upper switches of the corresponding leg. Meanwhile, the lower switch on the corresponding leg is enabled. The actuating vector selected in the previous time step is denoted n^- , while n^* denotes the actual optimum vector. The moving average of the instantaneous switching frequency \hat{f}_{sw} was computed online using a LPF whose equation in the

discrete-time domain is reported as follows:

$$\hat{f}_{sw}(n) = [1 - T_s\omega_{co}f_{sw}(n)]\hat{f}_{sw}(n-) + T_s\omega_{co}f_{sw}(n) \quad (5.4)$$

In (5.4), T_s is the time sampling, $\hat{f}_{sw}(n-)$ represents the moving average in the previous time step, while $\omega_{co} = 2\pi f_{co}$ is related to the cut-off frequency f_{co} set to 25 Hz. The term f_{co} is selected by considering a trade-off between having a quick settlement to the mean value with limited oscillations.

The calculated instantaneous switching frequency as well as its moving average are plotted over time in Fig. 5.3a. In the same time interval, the line-to-line voltages and the corresponding selected voltage vector, denoted as in Tab. 3.1, are shown in Figs. 5.3c and 5.3e, respectively. It can be verified how the instantaneous switching frequency was zero during the first four samples as the computed optimum vector did not change. When the commutation occurs, a peak in the instantaneous switching frequency is observable. The higher the number of commutations, the higher the resulting peak. The threshold is reached when three switches change state during a time step, and the resulting instantaneous switching frequency would be $f_s/2$. When two switching events occur the calculated f_{sw} results $f_s/3$. When only one switching commutation occurs, the computed f_{sw} would be $f_s/4$. On the other hand, when the switching state is constant, the instantaneous switching frequency is zero. Typically, the average switching frequency can vary from $f_s/5$ to $f_s/10$ [82]. The a -, b -, and c -phase current tracking are also shown for one electrical revolution in Figs. 5.3b, 5.3d and 5.3f, respectively.

It is well established that the higher the sampling frequency and, subsequently, the average switching frequency, the better performance in terms of current distortions can be achieved. The typical trend of the switch-

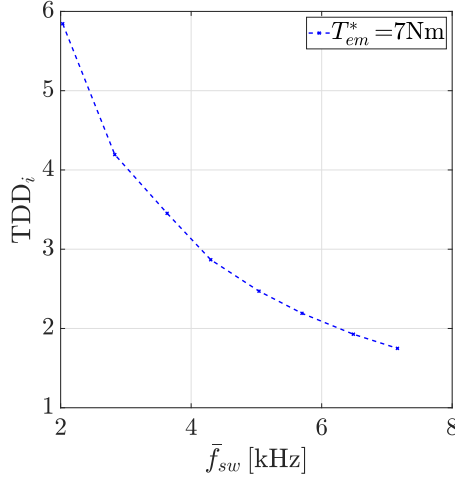


Figure 5.4: TDD_i versus \bar{f}_{sw} trend for $T_{em} = 14 \text{ Nm}$ MTPA.

ing frequency f_{sw} versus the TDD_i is shown in Fig. 5.4 obtained by running several simulations at increasing sampling frequencies for a fixed operating point. Specifically, demanding a specific torque reference (i.e., $T_{em} = 14 \text{ Nm}$), the d - and q -current references are evaluated according to the MTPA trajectory. The rotational speed was fixed by the prime mover to 1500 rpm and the dc-link voltage was fixed to 600 V. The sampling frequencies varied from 15 to 50 kHz with 5 kHz step between a simulation and the next one. The control effort term and the integral gains were disabled, and the cost function was defined as (4.2). The results of the eight simulations show that the higher the sampling frequency, the lower the resulting current distortions with a hyperbolic trade-off. Referring to the TDD_i versus \bar{f}_{sw} trade-off curve shown in Fig. 5.4, two results obtained at 25 kHz and 50 kHz corresponding to $\bar{f}_{sw} \approx 3.8 \text{ kHz}$ and $\bar{f}_{sw} \approx 5.2 \text{ kHz}$, respectively, are reported in Fig. 5.5. Specifically, the d - and q -current tracking is shown during transient and at steady-state in Figs. 5.5a and 5.5c for $f_s = 25 \text{ kHz}$, respectively. The subsequent a -, b -, c -phase current tracking is achieved by employing the Clark and Park transformations to the feedback and the reference signals, whose results are reported in Fig. 5.5e, and the corresponding harmonic spectra in Fig. 5.5g. Similarly, the same results are

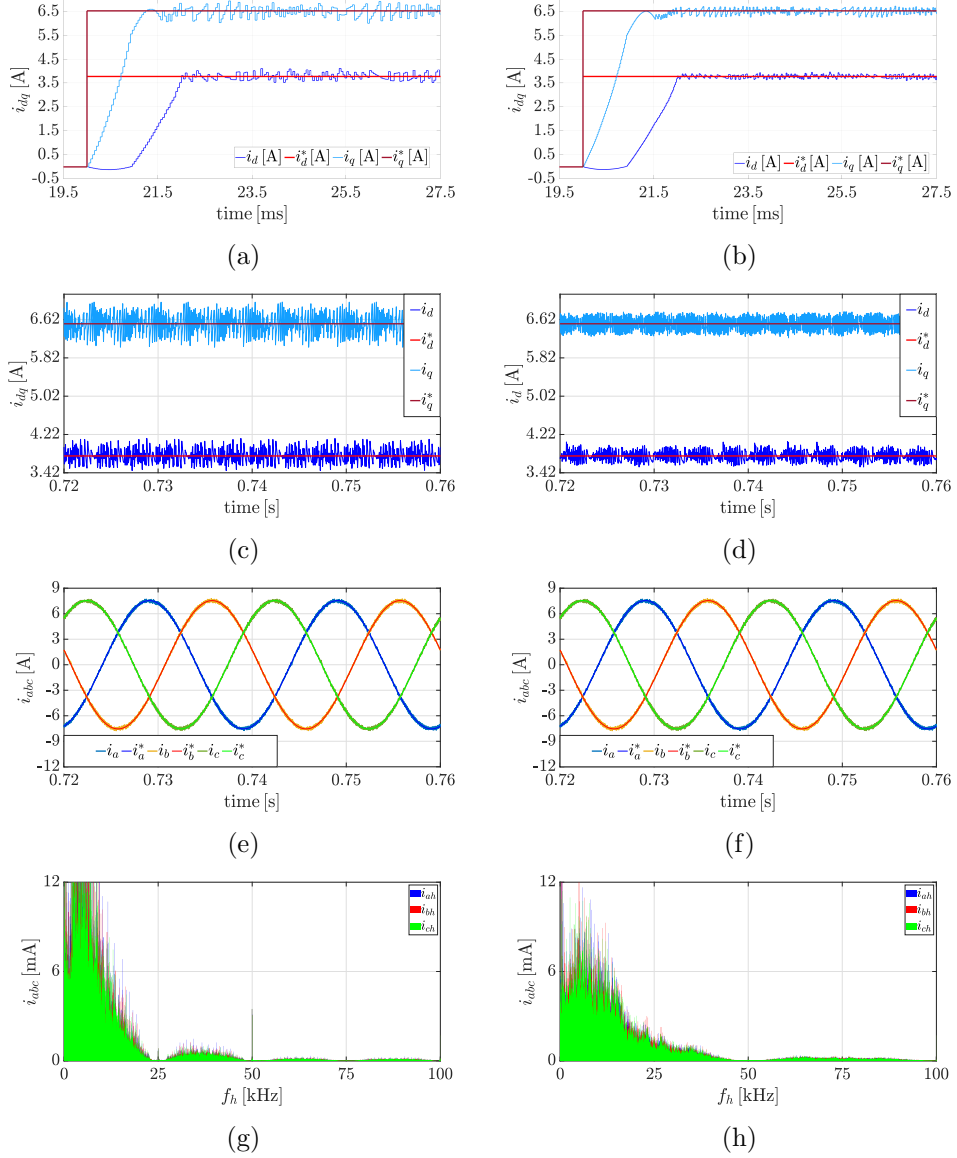


Figure 5.5: (a) dq -current tracking transient response at $f_s = 25$ kHz. (b) dq -current tracking transient response at $f_s = 50$ kHz. (c) dq -current tracking at $f_s = 25$ kHz. (d) dq -current tracking at $f_s = 50$ kHz. (e) abc -current tracking at $f_s = 25$ kHz. (f) abc -current tracking at $f_s = 50$ kHz. (g) Harmonic spectra at $f_s = 25$ kHz (h) Harmonic spectra at $f_s = 50$ kHz

shown for $f_s = 50$ kHz in Figs. 5.5b, 5.5d, 5.5f, and 5.5h. It can be observed how the current ripple on the d - and q -axis is higher at 25 kHz than 50 kHz, as well as the corresponding a -, b - and c -phase current harmonic content. In both cases, the most significant current harmonic content is bounded within the first side-band harmonic with a nondeterministic pattern.

5.1.0.2 Integral Terms Inclusion and Robustness Analysis

The effectiveness of the integral error term and the corresponding weighting factor to address current prediction errors will be proved by means of simulations run at 50 kHz. The system was aimed to be torque-controlled (i.e., $T_e m^* = 14 \text{ Nm}$) taking into account the MTPA and subsequently the resulting d - and q -current references (i.e., $i_d^* = 3.77 \text{ A}$, $i_q^* = 6.53 \text{ A}$) at a fixed rotational speed (i.e., $\omega_m = 1500 \text{ rpm}$). The control effort weighting factor was set to zero to highlight the sole effect of integral error term when current prediction errors are intentionally introduced. In particular, errors of $+50\%$ on the d -flux and -50% on the q -flux were considered, and the step response curves are shown for several integral weights in Fig. 5.6c for the d -current component, and in Fig. 5.6e for the q -current component. The integrals over time of the errors between references and feedback current components were also computed to highlight the presence of steady-state errors and their evolution over time. They are shown in Fig. 5.6d, and 5.6f for the d - and q -current errors, respectively.

When the integral of the error over time presents an average constant trend, it proves the absence of steady-state errors. On the other hand, the integral of the error shows an increasing trend. In Figs. 5.6a and 5.6b are shown the transient response on the d - and q -axis for three different W_d (i.e., $W_d = 0, 20, 80 [1/s]$) and W_q (i.e., $W_q = 0, 40, 160 [1/s]$). It can be noticed how the rise time results are equal for the three cases examined, while higher overshoots are observable when the integrals of the error gains are set higher. In addition, referring to Figs, 5.6c and 5.6e, when W_d and W_q are both set to zero, steady-state errors are observable on both the d - and q -axis, highlighted by the increasing trends of the integral of the errors shown in Figs. 5.6d and 5.6f for the d - and q -axis, respectively. It is also possible to

notice how greater weights lead to faster model mismatch compensations. When the weights are set to $W_d = 80$ and $W_q = 160$ [1/As], the integrals of the errors on the corresponding axis settle much faster than the other cases considered. Higher weighting factors also present higher overshoots. In Fig. 5.6g and 5.6h have also been shown the a -phase current tracking for the three considered cases, and the corresponding harmonic spectra, respectively.

Trial-and-error procedures can be carried out to select the weights to achieve the desired dynamic and steady-state performance [84]. In the cost function, it is possible to distinguish primary terms (i.e., reference tracking terms) and secondary terms (i.e., the control effort weighting factor). The first step of the procedure consists of setting the secondary terms weighting factors to zero. The second step is establishing measures such as the value of the current reference tracking and TDD as performance metrics to evaluate the performance achieved by gradually increasing the weighting factor starting from $\lambda_u = 0$. The achieved performance is recorded for each value of the selected λ_u , and the one that achieved satisfactory s and TDDs is selected. In the case study, when the model accuracy is high, lower values for the weighting factors can be selected to keep the dynamic behavior of the system unchanged. Further investigations would be required to study the stability of the system resulting from the introduction of the integral error term in a predictive controller frame (here not addressed). In this work, the stability of the system was guaranteed by trial-and-error procedures.

Another simulation with the same control settings as the one described in Fig. 5.6 was run to analyze the effect of the inductance variations (i.e., L_{dd} , L_{qq}). Errors of +50% and -50% on both the d - and the q -axis incremental inductance were considered. Variations of the mutual inductance terms (i.e., L_{dq} , L_{qd}) were not considered as they are about an order of

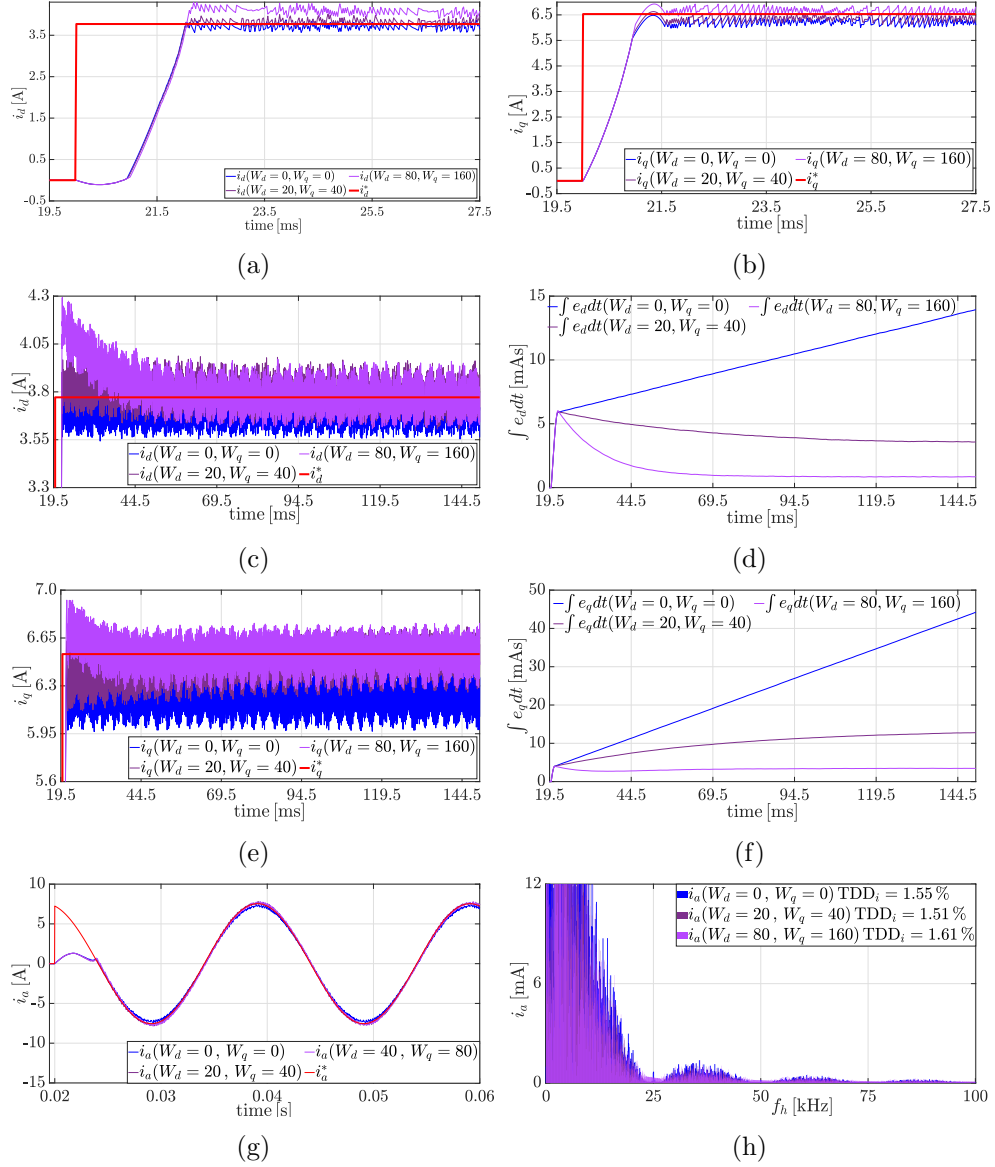


Figure 5.6: Effects of the flux vector variations on (a) d -current tracking during transient, (b) q -current tracking during transient, (c) d -current tracking at steady-state, (d) integral of the d -current tracking over time, (e) q -current tracking at steady-state, and (f) integral of the q -current tracking over time, (g) a -current tracking for the three cases, and (h) the corresponding harmonic spectra.

magnitude smaller than the self-axis inductance components. Referring to Figs. 5.7a and 5.7b, the d - and q -current reference tracking are shown as well as their corresponding integral of the error over time in Fig. 5.7c and 5.7d, respectively. In particular, three-step response curves are shown: one describes the case of considering a +50% error in both L_{dd} and L_{qq} ; the second case describes the case in which the actual self-axis incremental in-

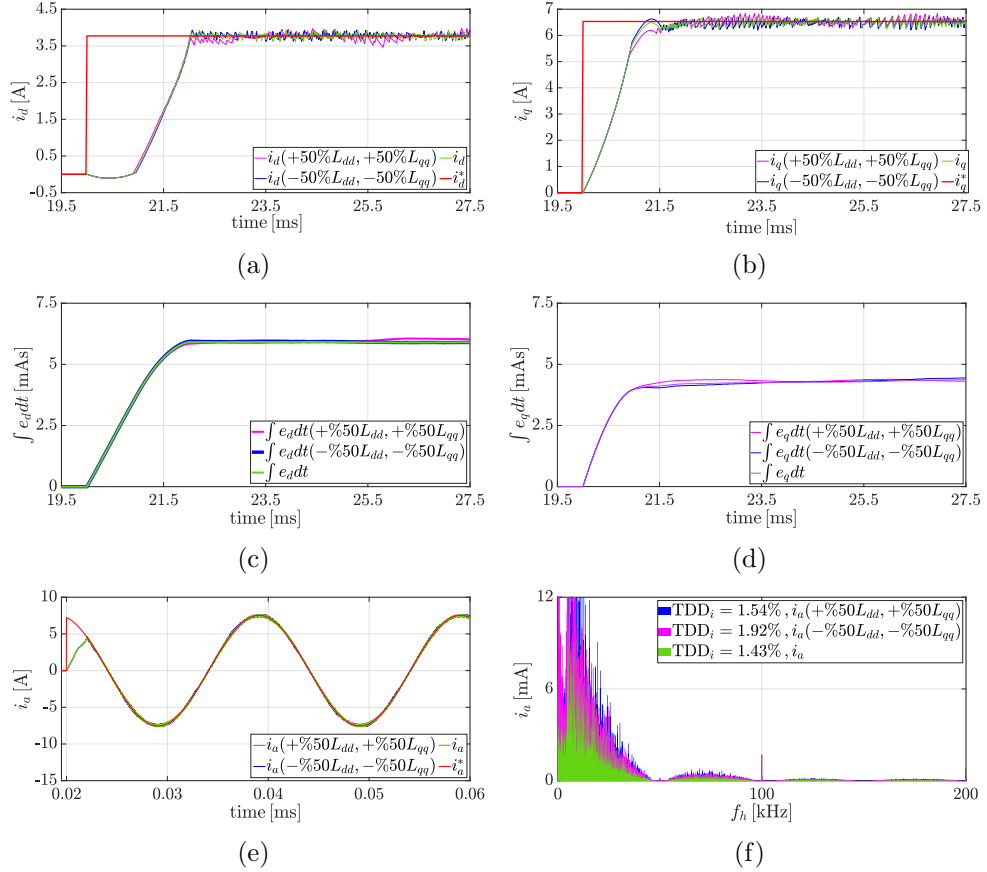


Figure 5.7: Effects of the flux vector variations on (a) d -axis current step response curve, (b) q -axis current step response curve, (c) integral of the d -current tracking over time, (d) integral of the q -current tracking over time, (e) a -phase current tracking, and (f) the corresponding harmonic spectra.

ductance components are decreased by 50%; finally, it also shown the case of inductance components closely matching the identified ones. In all the cases considered, the integral action was disabled (i.e. $W_d = 0$, $W_q = 0$). It can be noticed how the step response curves show quite similar behavior in the three cases and their corresponding integrals are approximately constants, proving that reference tracking errors do not depend on inductance inaccuracies. On the other hand, by performing the Fourier analysis on the resulting phase current waveform shown in Fig. 5.7e and observing the resulting harmonic spectra, it is possible to observe how these inaccuracies lead to higher ripples, thus higher current TDD_i than the case with a perfectly estimated inductance matrix (see Fig. 5.7f). Therefore, the best

performance in terms of current distortion can be achieved if the model of the system is accurately identified.

The voltage drop due to the stator winding is the last significant aspect to consider. However, stator resistance variations are omitted since the effect is more significant at lower speeds, and conceptually it is characterized by the same effect on steady-state performance as flux variations.

5.1.0.3 Control Effort Weighting Factor Variation

As described in the model of the drive in the Chapter 3, a set of simulations are performed with the SyRel motor in current-control mode while keeping the rotational speed and the dc-link voltage fixed. For a given sampling frequency, the control effort weighting factor is varied and the procedure is repeated for several sampling frequencies. The steady-state performance described in (5.1) is evaluated for each simulation. In Fig. 5.8, the resulting trade-off curve between the TDD_i and the average switching frequency \bar{f}_{sw} are shown considering conventional FCS-MPC (i.e. $\lambda_u = 0$), and the proposed cost function which include the control effort and the integral terms at two sampling frequencies, i.e. $f_s = 24$ kHz, $f_s = 40$ kHz. It is clear that the introduction of the control effort term (i.e. when $\lambda_u > 0$) allows achieving a lower current distortion over a wide range of switching frequencies and for different sampling frequencies with respect to the performance obtained with $\lambda_u = 0$. Indeed, considering the same switching frequency, i.e. $\bar{f}_{sw} \approx 4$ kHz, about 25% improvement of the TDD_i is obtained. The advantage in terms of TDD_i over the conventional approach increases as λ_u increases for a given sampling frequency f_s . Increasing the latter allows to achieve a wider switching frequencies range, indeed the blue line is wider than the dark green line, both calculated considering the same

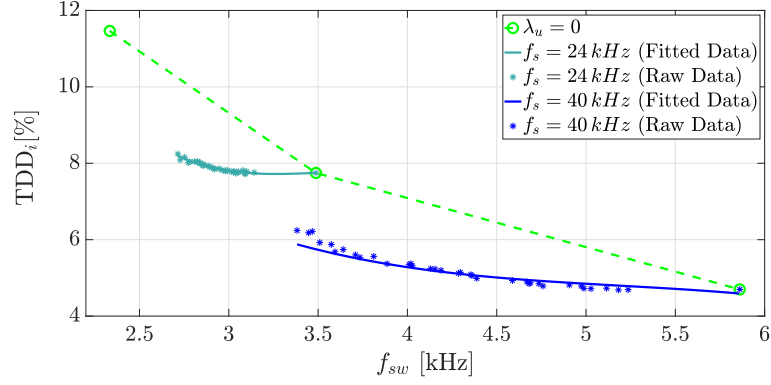


Figure 5.8: Trade-off curve between TDD_i and switching frequency at various λ_u and full-load ($i_d = i_q = 5.5$ A; $\omega_m = 1500$ rpm, $0 < \lambda_u < 0.056$).

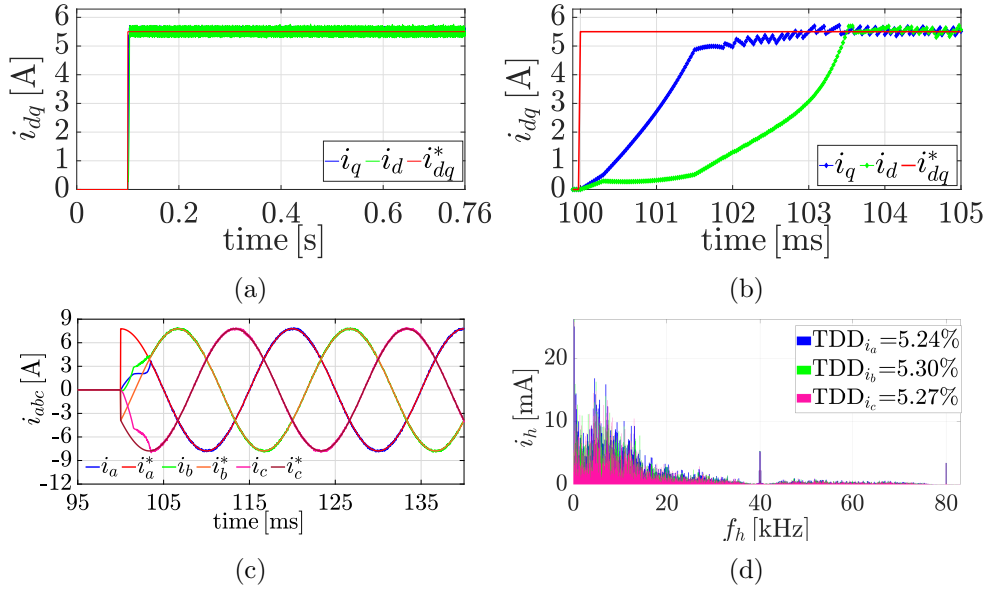


Figure 5.9: (a) dq -current reference tracking ($f_s = 40$ kHz, $\bar{f}_{sw} \approx 4020$ Hz, and $\lambda_u = 0.0384$). (b) dq -current reference tracking transients. (c) b -, c -phase currents reference tracking. (d) b -, c -phase current harmonic spectra.

range of λ_u . The simulations have been done at full load, i.e., the current references set to 5.5 A on both d - and q -axis, with the dc-link at 600 V, and the mechanical rotational speed at 1500 rpm. The current control tests are performed within a time window of 0.76 s, lasting long enough to have a periodicity over one mechanical turn.

The d - and q -current reference tracking are shown for $f_s = 40$ kHz and $\lambda_u = 0.0384$ in Figs. 5.9a and 5.9b, respectively. Moreover, in Figs. 5.9c

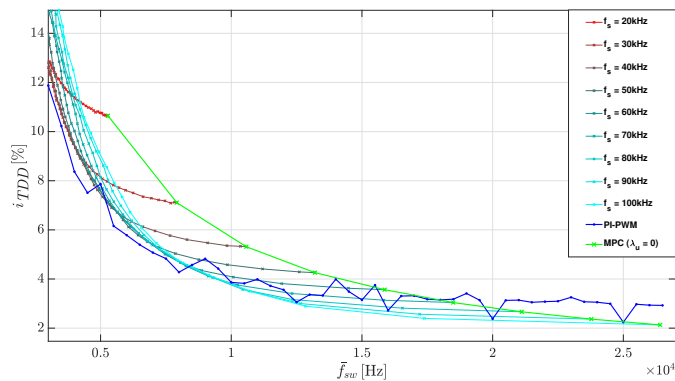


Figure 5.10: Comparative analysis between the FCS-MPC and the PI-based FOC control method.

and 5.9d are reported the a -, b - and c -phase current reference tracking and the harmonic spectrum of the phase currents, respectively, confirming the low current TDD_i .

To show the potential of the weighting factor term in the cost function, in Fig. 5.10 a comparative analysis between the FCS-MPC and the standard FOC-based control method is shown (blue line). It can be observed how the performance of the system surpasses the PI-based control approach for switching frequencies above 17 kHz when the sampling frequencies were set above 70 kHz and control effort weighting factor was $\lambda_u < 0.002$. This behavior is justified by the improved granularity of the switching aspect that makes the controller closer to a continuous time controller. This comparison was considered just on simulations due to the complexity of achieving such high switching frequencies on DSP. The described comparison can be performed by experimental tests if the described control strategy is entirely implemented on FPGA and that was not the purpose of this work.

Referring to the results shown in Fig. 5.10, a deeper comparison has been performed at 8.2 kHz switching frequency, showing further details of the system's behaviour with the two controllers. In particular, the d -current control step response is reported in Fig. 5.11a for both the FCS-MPC and

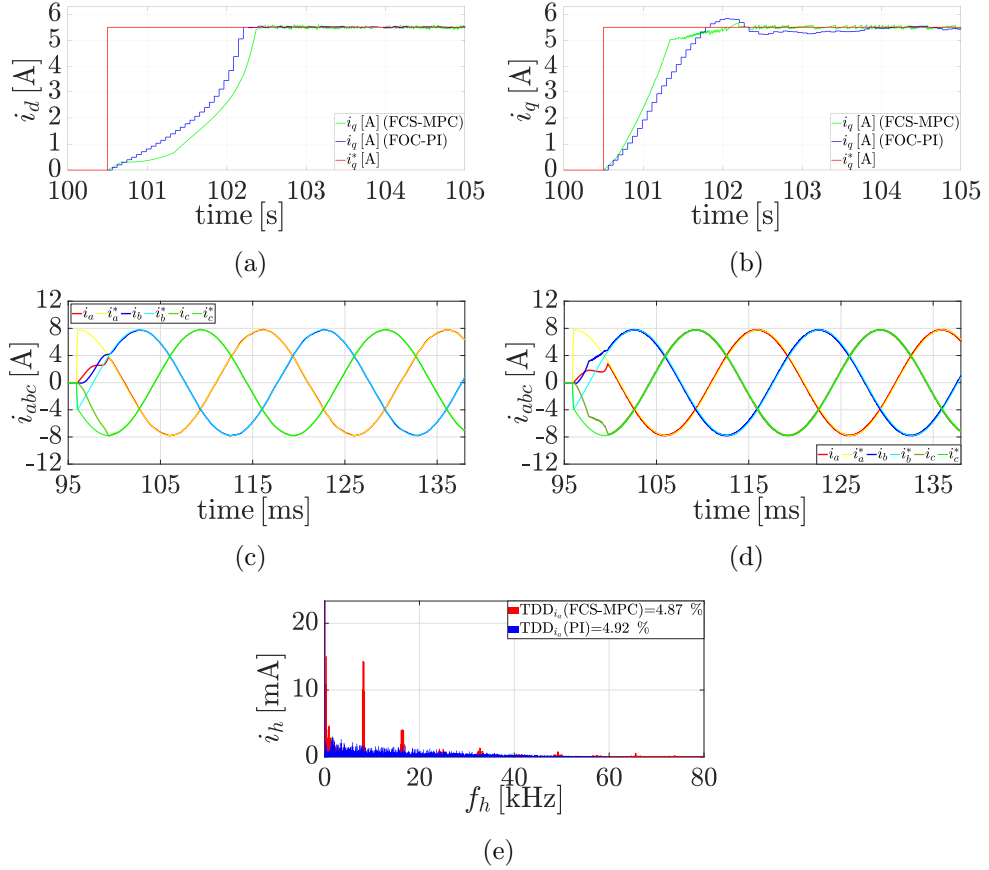


Figure 5.11: Comparative analysis of FCS-MPC versus PI-based FOC control at $\bar{f}_{sw} = 8.2$ kHz (a) d -current reference tracking. (b) q -current reference tracking. (c) Phase current reference tracking achieved by the FCS-MPC. (d) Phase current reference tracking achieved by the PI-based FOC control. (e) a -phase current harmonic spectra comparison.

the PI-based FOC control. The q -current step response curve is shown for both controllers in Fig. 5.11b. The phase-current tracking is illustrated in Fig. 5.11c and 5.11d for the two cases while the harmonic spectra referred to the phase "a" is also reported in Fig. 5.11e. In general, it can be noticed that the dynamic of the FCS-MPC slightly surpassed the PI-based FOC control method. Despite the similar current distortion, it can also be observed that the harmonic spectra of the PI-based FOC control method showed significant harmonic content at lower frequencies (i.e., 8.2kHz and multiples). For this reason, the FCS-MPC outperformed standard PI controllers at the cost of an increased computational cost.

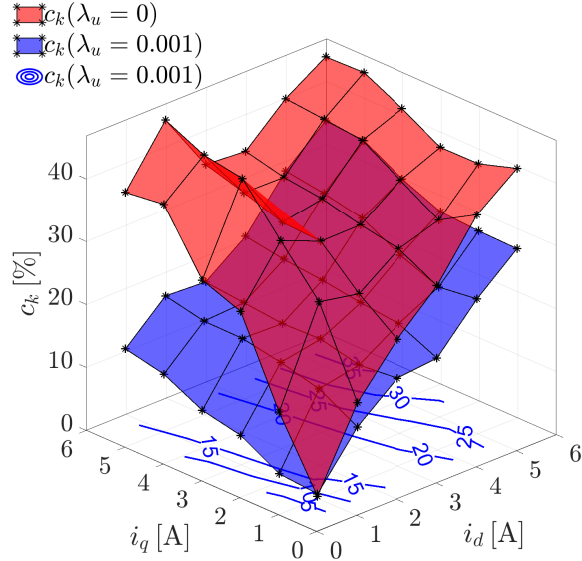


Figure 5.12: Steady-state performance variations due to changing the current command.

5.1.0.4 Current Variations

Given the importance of introducing the control effort weight greater than zero, a further analysis was carried out by means of simulations to investigate how the steady-state performance is affected by changing the operating point in the entire d - q current plane for two different values of the control effort weighting factor (i.e., $\lambda_u = 0$ and $\lambda_u = 0.005$). The rotational speed of the system was set to 400 rpm, the dc-link voltage was set to 300 V, while the sampling frequency was set to $f_s = 48$ kHz. Both the current components i_d , i_q vary from 1.5 A to 5.5 A, assuming a 1 A step between two consecutive points. With the aim of comparing these results, a comprehensive performance metric c_k is considered which is defined as the product between TDD_i and the inverse of the granularity of switching i.e., $\frac{\bar{f}_{sw}}{f_s}$.

$$c_k = \text{TDD}_i \frac{\bar{f}_{sw}}{f_s}. \quad (5.5)$$

The latter takes into account both the effect of the switching frequency and the TDD_i . Lower c_k values mean better overall performance. In Fig. 5.12, the obtained c_k are represented for the two cases studied. First of all, it can be observed how c_k presents lower value of c_k when $\lambda_u = 0.005$. In addition, c_k is mostly affected by variations due to d -current component. The reason behind this behavior is found in the inductance variations. Specifically, variation due to the d -axis current cause more significant L_{dd} drop than L_{qq} variations (see Fig. 3.16), making the system more sensible to d -axis current variations.

5.1.0.5 Speed Variations

When the drive operates at different rotational speeds, the overall performance might change. In particular, the cross-coupling terms in (3) depending on the rotational speed alter the calculation of the current prediction whose cost function is dependent. Few simulations were run to quantify how the performance varies with the rotational speed. Specifically, several current control simulations were run to identify the importance of the rotational speed variations when considering two different values of the control effort weighting factor (i.e. $\lambda_u = 0, \lambda_u = 0.005$). The sampling frequency was fixed to $f_s = 48$ kHz and both current references i_d, i_q were set to 1.1 A. The rotational speed varied from 100 rpm to 900 rpm with 100 rpm speed step between two consecutive simulations. Referring to Fig. 5.13a, the \bar{f}_{sw} trend over speed is represented in blue for $\lambda_u = 0$, while it is represented in violet when $\lambda_u = 0.01$. In the same figure, the TDD_i trends for the rotational speed ω_m are also represented. In both cases, lower switching frequency and lower TDD_i are observable when the control effort weighting factor is greater than zero. Furthermore, Fig. 5.21b shows the trend of c_k over speed in the two cases studied. Lower c_k is observable with $\lambda_u = 0.005$.

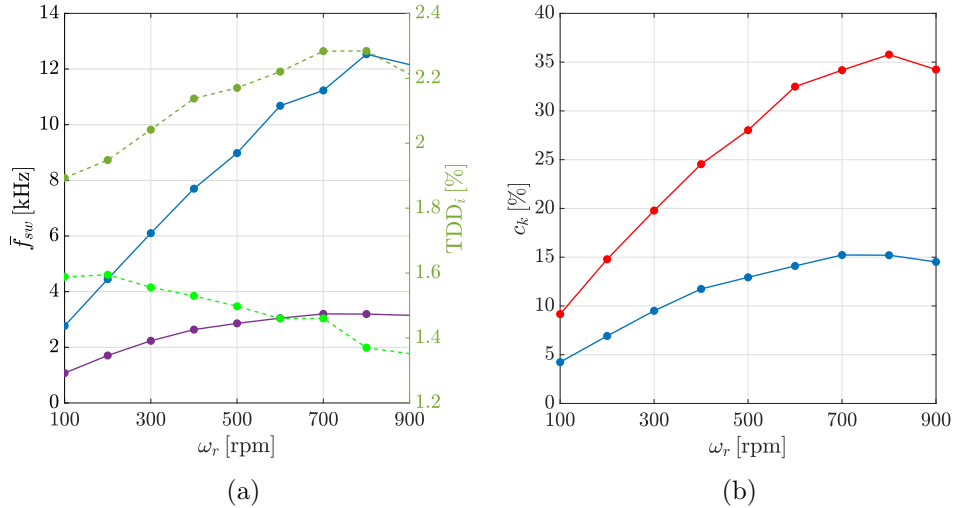


Figure 5.13: (a) dq -current reference tracking ($f_s = 40$ kHz, $\bar{f}_{sw} \approx 4020$ Hz, and $\lambda_u = 0.0384$). (b) dq -current reference tracking transients. (c) b -, c -phase currents reference tracking. (d) b -, c -phase current harmonic spectra.

It can be deduced how lower c_k can be obtained by setting the $\lambda_u = 0.005$. Furthermore, the rate of difference between the two trends in Fig. 5.13b is higher at higher speed, justifying the introduction of the control effort weighting factor. The absence of a standard procedure to tune the control effort weight make the controller design process more complex and it remains an open topic for future investigations.

5.2 Experimental Results

The test rig for this set of experiments is described in appendix A. During tests the average dc-link was 300 V fixed by a dc-power supply, and limited by the industrial drive rated voltage. The following aspects have been assessed: the impact of the integral term inclusion on reference tracking; the improvement of the steady-state performance due to the control effort weighting factor variations for a fixed operating point, and over the entire d - q current domain; effects on steady-state performance have also been evaluated at different speed and torque.

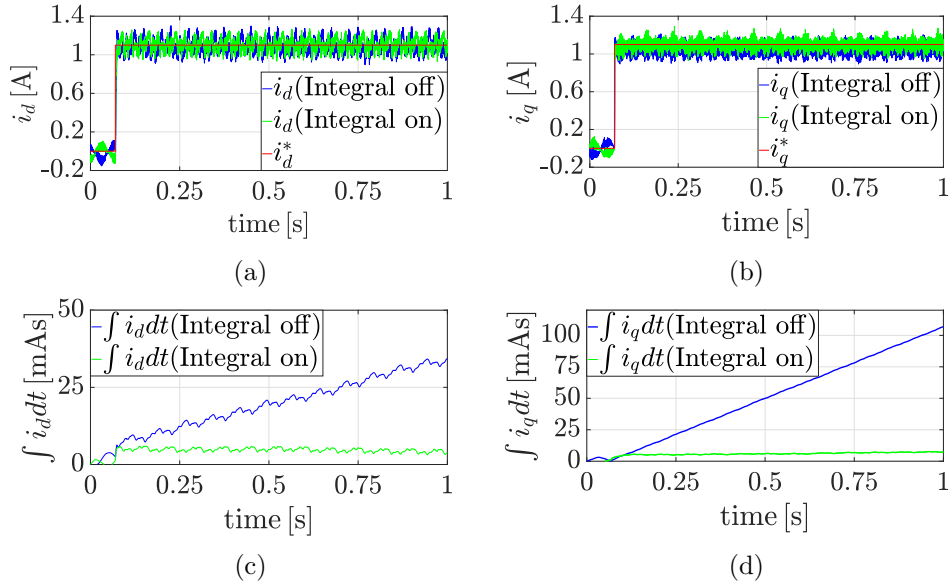


Figure 5.14: (a) d -current tracking with and without integral (b) q -current tracking with and without integral. (c) Numerical integration of the d -current error over time with and without integral. (d) Numerical integration of the q -current error over time with and without integral.

5.2.1 Integral Terms Assessment

Two current-control tests at a constant speed ($\omega_m = 100$ rpm) have been performed to show the impact of including integral terms when a +50% error is introduced in both flux vector components ψ_d , ψ_q in the current predictions. In Figs. 5.14a and 5.14b the d - and q -current reference tracking are shown in both cases when the integral term is considered (green lines) and not considered (blue lines). The numerical integration of the current errors (see (4.5)) is also computed and plotted in Figs. 5.14c, and 5.14d to make the results clearer. Analyzing these figures, it is evident that including the integral term in the cost function allows for achieving zero steady-state current error, even in the presence of model inaccuracies. As a result, a high degree of robustness is achieved and potential parameter variations, model mismatches, etc., are successfully tackled by the controller.

It is worth underlining that the integral of the current vector error is calcu-

lated considering the current reference and the feedback signals of all the past measurements. The cross product between (4.4) and the integral of (4.5) in 4.7 makes the selection of the optimum actuating voltage vector dependent on the integral of any detected steady-state error. By doing so, the inclusion of the integrals of the error terms does not introduce significant computational complexity compared to the methods based on the predictions and on augmenting the state of the system. The integral is performed only once per current component, making the integral calculation model-free but keeping the model-based terms as a proportional action. The integral calculation is performed by storing and summing up the past current errors $\sum_{j=1}^{\ell} i_{dq,err}^{k-1}$ with the actual current error $i_{dq,err}^k$ in (4.7). The result is then multiplied by the sample time and the weighting factors.

An experimental comparison with the method introduced in [3] is also performed. The purpose of the integral action introduced in [3] aimed to compensate for inter-sampling errors due to the discrete-time prediction model, temperature-dependent parameters drifting or aging factors, and model mismatches. The method consists of evaluating the integral of the error terms (i.e., $\mathbf{I}(n)$) from the reference command and the current prediction as follows:

$$\mathbf{I}(n) = \int_0^{\tau} [\mathbf{i}_{dq}^* - \mathbf{i}_{dq}^{k+1}(n)] dt \approx T_s \sum_{j=0}^m \mathbf{i}_{dq,err}^{k+1-j}(n) \quad (5.6)$$

With the above, the (simplified) cost function considered in [3] is

$$J(n) = \|\mathbf{i}_{dq,err}^{k+1}(n)\|_2^2 + \mathbf{W} \|\mathbf{I}(n)\|_2^2 \quad (5.7)$$

The integral of the error calculation is based on the current prediction error (i.e., $\mathbf{i}_{dq,err}^{k+1-j} = \mathbf{i}_{dq}^* - \mathbf{i}_{dq}^{k+1}(n)$) at the next time step $k + 1$, where T_s is the sampling interval, and τ represents a generic time instant during the test/-

operation. The integral action is the sum of the previous output and the new error that is amplified by the integral gain. Hence, the integral action allows for the accumulation of errors over time. The value m introduced in (4.7) expresses this accumulation action. In essence, it represents the number of samples during the tests. Hence, it starts from 0 at time zero (i.e., when the test begins) and it increases during the experiment. Nevertheless, m is initialized to zero at the beginning of each period (due to the 2π -periodicity) to avoid potential overflow problems occurring during prolonged operations. In other words, m represents the step at which the discretized integral of the error is calculated.

[3] investigated how the effectiveness of the integral action is affected by varying m . In particular, it is shown that larger time windows allow to achieve better compensation of the model mismatches. Nevertheless, the proposed integration method does not make any difference from a computational perspective whether the whole test/operation is considered or merely a limited time window. This is because the previously stored values are updated at each new iteration of the controller, i.e., only one new operation is the performance at each sampling interval.

Given the above, for a fair comparison between the method proposed and the one presented in [3], the same time window (i.e., the whole test/operation time window) was considered. The results are shown in Fig. 5.15. As can be seen from the figure, both methods achieve similar robustness to parameter variations, albeit the proposed one exhibits somewhat shorter settling times. Note that only the tracking behavior on the q -axis is shown for reasons of compactness; the behavior on the d -axis is similar. Even though both the proposed FCS-MPC scheme and the one in [3] include an element of integrating nature in the cost function, this is done differently. Specifically, the proposed method introduces the product between the pre-

dicted and accumulated errors—see (4.4) and (4.5), respectively—that can enable faster transient responses. To verify this, the tests were carried out by considering that the flux was overestimated by 30% while operating in the current-control mode and at a constant speed. The d - and q -current references were set to $i_d = 2.6$ A, and $i_q = 3.7$ A, respectively, corresponding to a torque command of $T_{em} = 7$ Nm. Moreover, the rotational speed was 800 rpm, and the dc-link voltage 300 V. Finally, the sampling frequency was 24 kHz, and the control effort weighting factor was chosen as $\lambda_u = 0.0040$. For the first test, the integral of the current error was excluded from the cost function; the corresponding tracking of the q -component of the current reference is shown in Fig. 5.15. In the same figure, the tracking performance of the proposed FCS-MPC method is shown when the integrating term is active. Finally, for comparison purposes, the behavior of the method in [3] is depicted. As can be observed, both FCS-MPC methods successfully compensate for the error introduced in the prediction model due to the flux variation, but the proposed method exhibits better dynamic performance. Finally, it is worth mentioning that the integral of the current error is calculated considering the predicted current error (see (4.4)) and the integral of the past errors (see (4.5)). As these depend on the (known) current reference and the (already computed) accumulated steady-state error, respectively, it can be seen that the additional computational overhead is very small, especially as compared with methods that rely on an augmented state or an exhaustive prediction of the state. Hence, the proposed method, not only selects the optimal actuating voltage vector by accounting for the past steady-state error (and thus by introducing an integrating element that improves the robustness), but it also comes with a relatively low computational complexity.

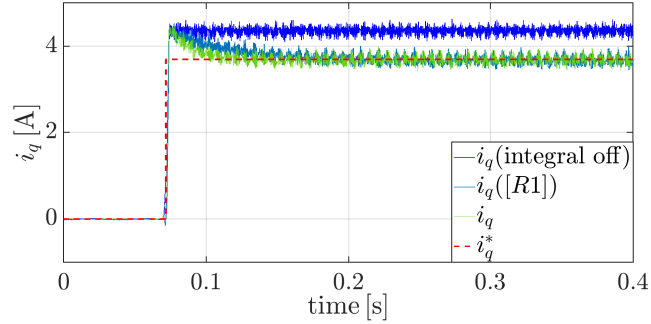


Figure 5.15: Assessment of the effectiveness of the integrating action of the proposed FCS-MPC scheme and its comparison with the method described in [3].

5.2.2 Control Effort Assessment

In the following, more experimental evidence on the SyRel drive is reported. In this test campaign, the SyRel motor run in current-control mode at a constant speed set by the prime mover, and with the dc-link voltage set by the dc-power supply. The control effort weighting factor is varied at several sampling frequencies and the steady-state performance metrics described in (5.1) are evaluated.

5.2.2.1 Tests at rated current

Due to the hardware limitation on the dc-link bus voltage, the following tests were arbitrarily chosen to meet the hardware limitations while guaranteeing no voltage saturation. The current references on the d - and q -axis were set equal to the rated value while the speed was fixed by the prime mover to 100 rpm. Fig. 5.16 reports the results in terms of current TDD _{i} of the test campaign carried out for three different values of sampling frequency: $f_s = 32, 40, 48$ kHz over a wide range of λ_u . Each test lasts enough to acquire at least twenty electrical periods for accurate computation of the current TDD _{i} to assess the effectiveness of the proposed FCS-MPC to

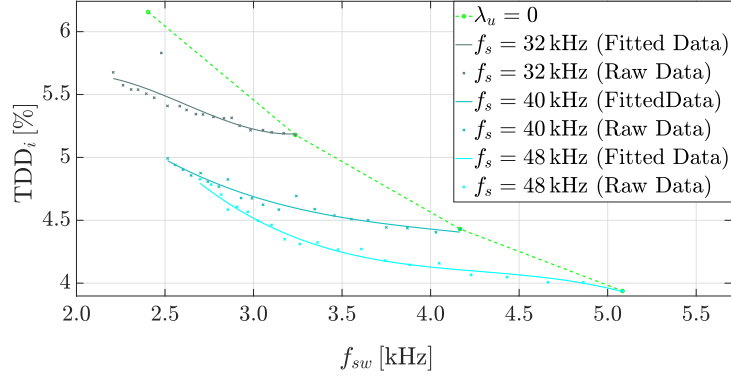


Figure 5.16: Trade-off curve between TDD_i and switching frequency ($i_d = i_q = 5.5$ A; $\omega_m = 100$ rpm, $0 < \lambda_u < 0.032$).

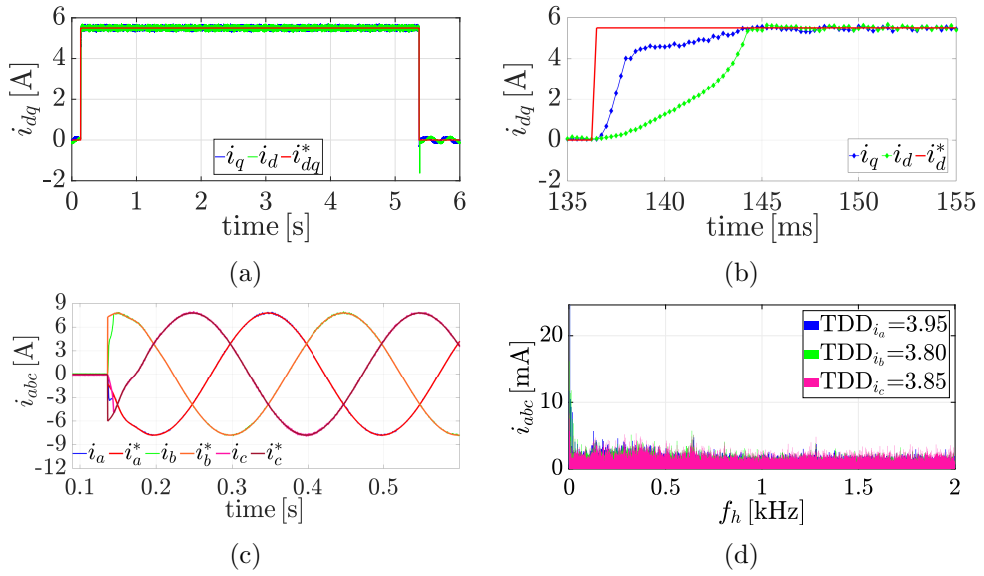


Figure 5.17: (a) dq -current reference tracking ($f_s = 48$ kHz, $\bar{f}_{sw} \approx 3.2$ kHz, and $\lambda_u = 0.0160$). (b) dq -current reference tracking transients. (c) b -, c -phase currents reference tracking. (d) b -, c -phase current harmonic spectra..

guarantee zero steady-state reference tracking errors, and a reduced TDD_i compared to conventional FCS-MPC. Similar to the simulation studies (see Fig. 5.8), the trend based on the experiments is the same, i.e., the proposed FCS-MPC outperforms the conventional one, thanks to the fine granularity of switching. The trial-and-error procedure was considered to tune the control effort weighting factor to show the obtained results. Fig. 5.17 reports the dq -current tracking, the phase-currents, and the phase current spectrum for the given operating point.

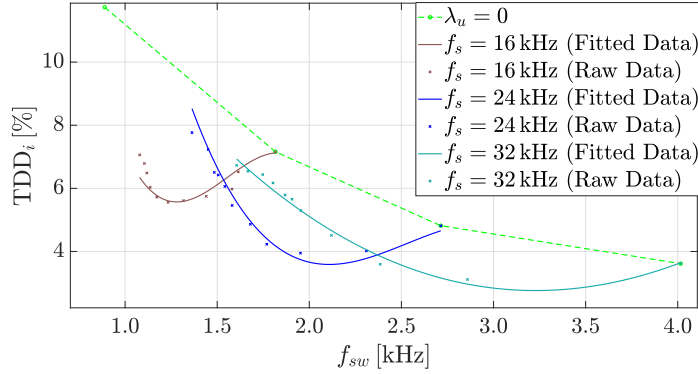


Figure 5.18: Trade-off curve between TDD_i and switching frequency at various λ_u ($i_d = i_q = 1.1$ A; $\omega_m = 400$ rpm, $0 < \lambda_u < 0.08$).

5.2.2.2 Tests at 20% of the Rated Current

In another test campaign, the dq -axis current references were chosen to be 20% of the rated current, while the rotational speed was set to 400 rpm. As for the previous set of tests, the trend illustrated in Fig. 5.18 shows that a more favorable TDD_i can be achieved with the proposed FCS-MPC algorithm. Differently, from the former case, the trends for the three tested sampling frequencies $f_s = 16, 24, 32$ kHz show a higher margin of improvement. Furthermore, the trends are not monotonically decreasing as the switching frequency increases but they present minimums. This difference can be justified by the non-linear inductance variations with the current which is an intrinsic characteristic of the SyRel. The higher the load current, the lower the corresponding inductance, thus the importance of the tracking term over the control effort in 4.7 prevails. However, the effects due to current and speed variations are further discussed in the following subsections. Also in this case, the dq -reference current tracking, the phase currents and their spectrum are shown in Fig. 5.19.

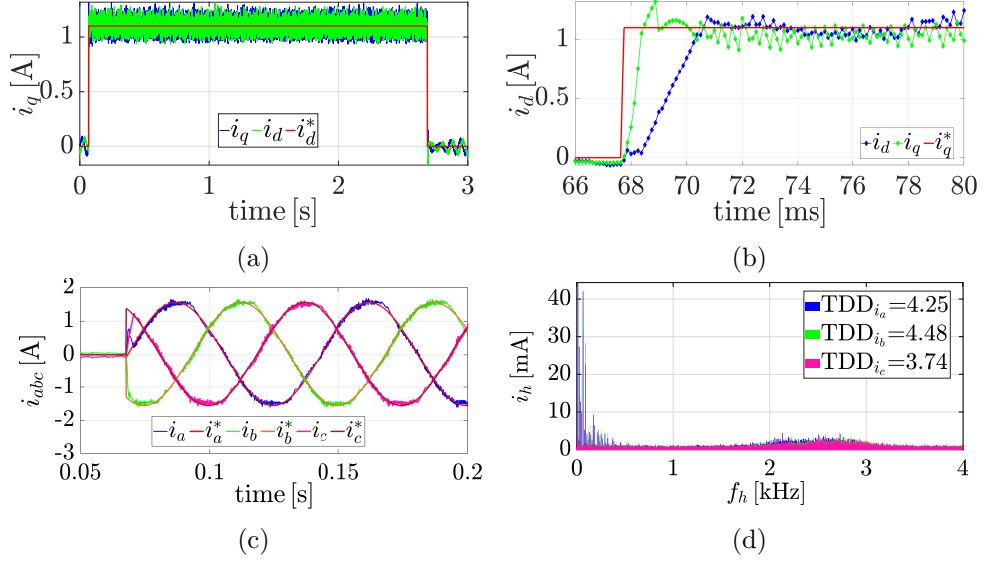


Figure 5.19: (a) dq -current reference tracking ($f_s = 24$ kHz, $\bar{f}_{sw} \approx 2$ kHz, and $\lambda_u = 0.0160$). (b) dq -current reference tracking transients. (c) a -, b -, c -phase currents reference tracking. (d) b -, c -phase current harmonic spectra.

5.2.3 Tests over the entire d - q current plane

The following reports an experimental investigation of the steady-state performance over the entire d - q current plane for two different values of the control effort weighting factor, i.e., $\lambda_u = 0$ and $\lambda_u = 0.0160$. The rotational speed was fixed at 400 rpm while the sampling frequency was set to $f_s = 48$ kHz. Both the current components i_d , i_q vary from 1.5 A to 5.5 A, assuming an 1 A step. To compare these two series of tests, a comprehensive performance metric c_k as defined in (5.5). The latter takes into account both the effect of the switching frequency and the TDD_i . Lower c_k values mean better overall performance. In Fig. 5.20, the obtained c_k are plotted for the two cases $\lambda_u = 0$ and $\lambda_u = 0.016$. It can be noticed how the c_k variations are mostly due to d -current component variation (see Fig. 5.20 contour plots) as the L_{dd} variation over the tested current domain is more significant than L_{qq} variations (see Fig. 3.16). Furthermore, higher performance is achievable in the whole explored current domain by setting $\lambda_u > 0$.

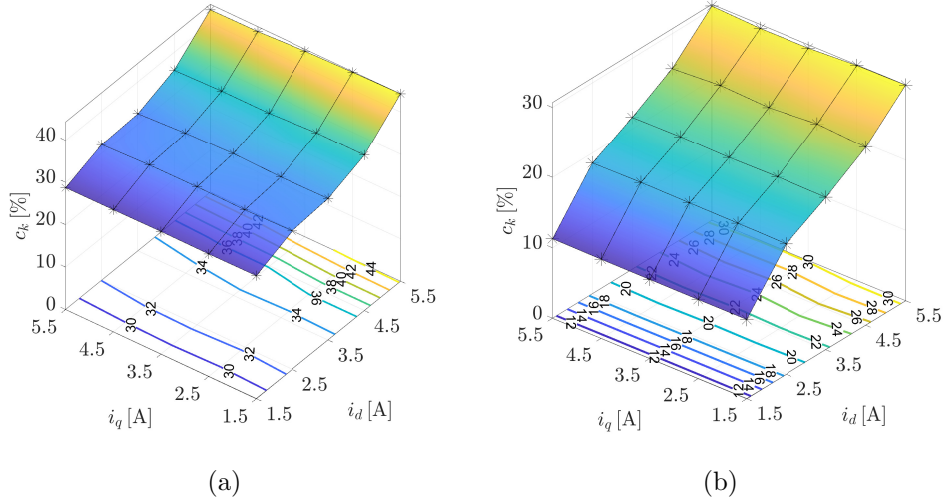


Figure 5.20: (a) Overall steady-state performance over the current domain given $\omega_m = 100$ rpm, $f_s = 48$ kHz, $\lambda_u = 0$. (b) Overall steady-state performance over the current domain for $\omega_m = 100$ rpm, $f_s = 48$ kHz, $\lambda_u = 0.016$.

5.2.4 Tests at different speeds

Speed variations also have an impact on the overall performance. For this reason, current control tests were performed to quantify the importance of this variation for two values of the control effort weighting factor ($\lambda_u = 0, \lambda_u = 0.0160$). The tests were performed with a fixed sampling frequency ($f_s = 48$ kHz) and both current references i_d, i_q set to 1.1 A, while the rotational speeds varied from 100 rpm to 900 rpm with 100 rpm speed step. Referring to Fig. 5.21a, the TDD_i and \bar{f}_{sw} trends with respect to the rotational speed ω_m are represented showing advantageous results when $\lambda_u = 0.0160$. Fig. 5.21b shows the c_k trend over speed in the two cases. Lower c_k is observable with $\lambda_u = 0.0160$ when $w_m > 750$ rpm. This is because the back-electromotive force term in (3.5) makes the reference tracking term in (4.7) more important than the control effort. Combining the results of increasing the load current and the rotational speed, a lower margin of improvement is observable due to the reduced importance of the control effort term over the reference tracking term.

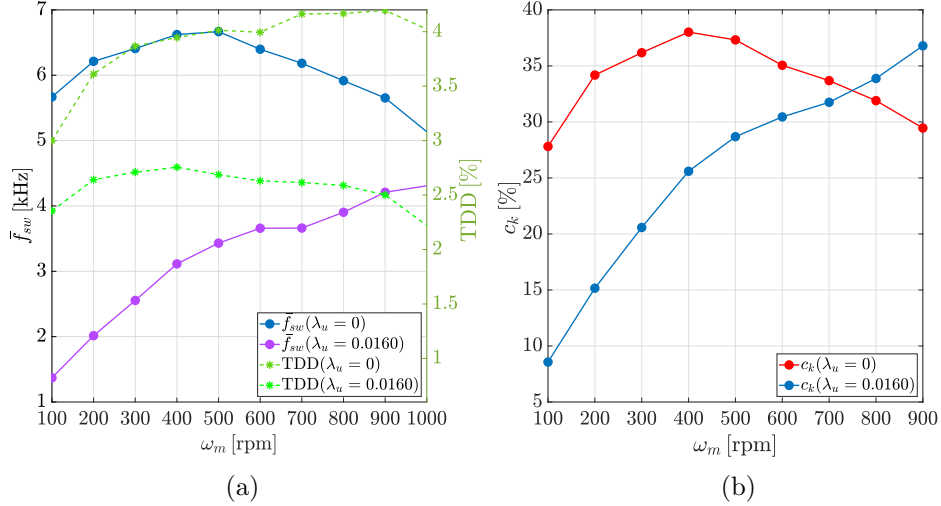


Figure 5.21: (a) TDD_i and \bar{f}_{sw} trends with respect to the speed for a fixed $\lambda_u = 0$. (b) TDD_i and \bar{f}_{sw} trends with respect to the speed for a fixed $\lambda_u = 0.016$.

5.2.5 Tests at MTPA conditions

Considering the same current controller, consisting of the proposed cost function that accounts for the current tracking error, an outer block was considered to calculate the current reference commands corresponding to a specific electromagnetic torque. The operations in current or torque mode indicate the functionality of the outer loop. Operating in both modes enables the examination of different scenarios, and thus the assessment of the performance of the proposed FCS-MPC scheme at more operating points. Specifically, in current mode, the reference currents are set directly. On the other hand, in torque mode, the current references are calculated from the MTPA's LUTs, where the torque command corresponds to a specific pair of current coordinates, selected according to the MTPA shown in Fig. 3.19. Finally, it is worth mentioning that testing a control scheme by alternating between the two operating modes is a common practice in the industry as well.

Two torque control tests ($T_{em} = 1.4\text{Nm}$, and $T_{em} = 12.6\text{Nm}$) were performed and compared for various f_s and λ_u in Fig. 5.22. Lower TDD_i is

achieved for lower torque when considering the same switching frequency. In addition, a lower margin of improvement can be achieved by varying λ_u when considering high torque values. Indeed, with higher torque, the current reference tracking term in (4.7) dominates the control effort, decreasing the margin of improvement. It is like the whole lower torque

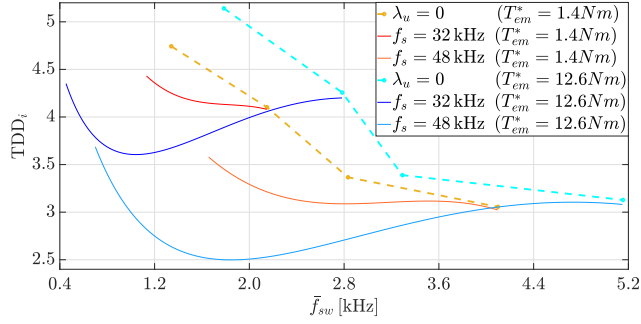


Figure 5.22: TDD_i and switching frequency trade-off for two torque references ($\omega_m = 100$ rpm, $0 < \lambda_u < 0.032$).

trend rotates and moves toward the left reducing the resulting switching frequency range. This behavior is justified by the fact that as the current components rise, especially on the d -axis (see the MTPA Fig. 3.19), the corresponding inductance decreases causing the reference tracking term in (4.7) to be more important than the case at lower torque reducing the margin of improvement.

5.3 Chapter Conclusions

In this chapter, extensive simulation and experimental analysis have been conducted to show the performance of the proposed FCS-MPC. The first step consisted of evaluating the system's robustness against parameter variations. In particular, model mismatches have been introduced in the prediction model to observe the effectiveness of the introduced integral terms in the cost function without affecting the dynamic performance. This study

has been considered in both simulations and then validated experimentally.

The second step consisted of evaluating the impact of the introduced control effort weighting factor in the cost function aimed at improving the steady-state performance. It has been shown that the use of the control effort weighting factor properly tuned enabled lower current distortion in both simulations and experimental tests.

Finally, the impact of changing the operating point has been investigated highlighting the fact that an accurate magnetic model and optimum trajectories are highly recommended to enhance the proposed controller performance.

Chapter 6

SyRel Drive:

Modulated-Model Predictive Control

In this section, the proposed M-MPC is derived. It belongs to the family of M-MPC controllers.

The proposed method solves the control and modulation problems in one computational stage in an optimal, coordinated manner. Moreover, it has an inherent mechanism to address the over-modulation problem. Thanks to these two characteristics, it can fully utilize the available dc-link voltage and compute the optimal application times of the optimal switch positions. For PI-based field-oriented control (FOC) and deadbeat control methods, control and modulation are two decoupled entities that act independently from each other, i.e., in an uncoordinated manner. Moreover, in case of overmodulation, a dedicated mechanism is required to saturate the commanded voltage. The above implies that when the voltage synthesized by the modulator is different from the voltage commanded by FOC, the best

possible dynamic performance is not guaranteed because the basic current transition phenomena are neglected [85].

Based on the above, the main advantages of the proposed method are: 1) Full utilization of the available dc-link voltage thanks to the coordinated control and modulation. 2) Simpler controller design as control and modulation are considered together, while there exists an inherent mechanism to address the overmodulation problem. Moreover, no significant tuning is required, as for the case with PI controllers, where the gains are chosen for specific operating points, and then gain scheduling is performed to make the controller suitable for a wide range of operations.

The block diagram of the proposed M-MPC is illustrated in Fig. 6.1. The phase currents (i.e. i_a, i_b), the dc-link voltage (i.e. V_{dc}), as well as the rotor angular position θ_r are measured and used to predict the current vector in dq coordinates at the next time step $k+1$. The angle was measured utilizing an optical encoder. The electrical speed ω_r was numerically computed from the rotor angle considering the number of pole pairs specified in Table A.1. The calculated electrical speed was then filtered by a low-pass filter to reduce the ripples caused by quantization error introduced by the encoder and provide higher robustness and relatively constant speed [86].

Another common practice that was adopted in the present work relates to the compensation for the encoder inter-sampling errors [87]. In the real-world setting, at the beginning of the sampling interval, the actual rotor angle is measured, and a one-step delay occurs between measurements and actuation. During this interval, when the motor rotates at a constant speed, the rotor position changes. For a given sampling interval, more significant rotor displacements occur at higher speeds. Consequently, an error in the current reference tracking is observable as the controller is designed in the

synchronously rotating dq reference frame. This inter-sampling angle offset can be compensated for by considering the following:

$$\theta_c = \theta_r + \frac{1}{2}T_s\omega_r \quad (6.1)$$

In (6.1), θ_c is the rotor angle that compensates for the inter-sampling error due to the rotation of the drive at ω_r , θ_r is the rotor angle measurement and T_s the sampling interval. The such compensated angle can be used in the Park and the inverse Park transformations to switch from the stationary to the synchronous reference frames without affecting the steady-state performance. This aspect is beneficial, particularly for the introduced model-based control strategy.

6.1 Evaluation Function

The typical MPC approach consists of selecting the best actuating variable based on the definition of a cost function which is by definition a positive scalar. The cost function is then evaluated as many times as the number of configurations the actuator (i.e., a 2L-VSI) can assume, and the configuration corresponding to the minimum cost function is selected to control the drive system. The cost function typically includes the 2-norm of the error tracking terms. Differently from the rigorous definition of a cost function, defined as a positive scalar, an evaluation function has been defined such that it can assume both positive and negative values. The control problem has been tackled geometrically evaluating the vectors that comply with specific geometric conditions. The defined evaluation function divided into two scalar components is introduced and evaluated from the current reference signals i_d^* , i_q^* , and the current predictions (4.1).

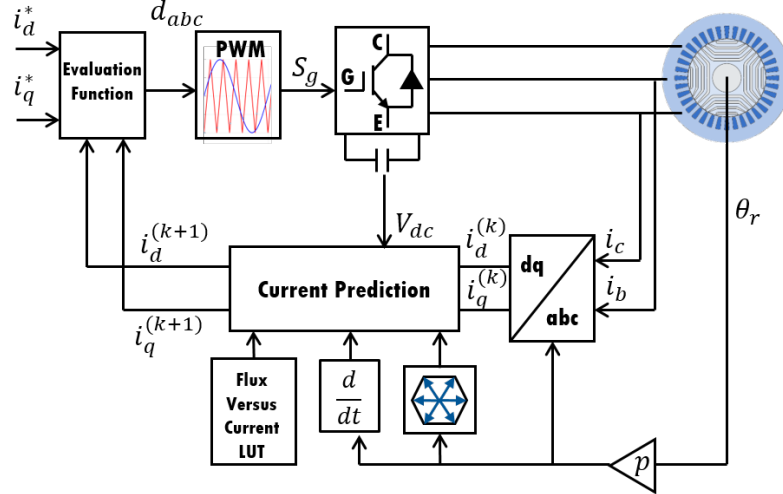


Figure 6.1: Block diagram of M-MPC for SyRel motor drive.

Subsequently, the duty cycles (i.e. d_{abc}) are computed based on an on-line optimization problem and sent to a modulation stage to generate the switching signal S_g of the 2L-VSI to control the SyRel at the desired operating point. The current prediction components are calculated as in (4.1) considering the flux and the inductance terms as functions of the current vector as described in Sect. 3.4. The design of the proposed evaluation function was done such that the following three goals are achieved. Firstly, to enable the integration of the tracking error in the same fashion as in the PI-based controllers. In doing so, improved tracking performance and increased robustness can be achieved, as demonstrated in the following. Secondly, to introduce a self-saturation mechanism to the computation of the target coordinates. This is achieved with the adoption of the geometric criteria according to (6.5a), (6.5b) and (6.5c). And lastly, to facilitate a greater controller design simplicity by avoiding the use of weighting factors.

Differently for the standard cost function, the components of the evaluation function can assume both positive and negative values. Furthermore, the classical formulation of the cost function does not allow for such flexibility unless additional constraints are included in the optimization problem.

This, however, would complicate the controller design and increase the size of the optimization problem, and thus its computational complexity. Moreover, the weighting factor selection criteria are based on empirical and iterative processes [88].

With the use of traditional cost functions, nonlinear systems such as the considered SyRel drive exhibits high saliency. As a result, the level sets of the (convex) cost function are ellipsoidal, see Fig. 4.2. This implies that for equally good tracking of the two current references (on the d - and q -axis) a weighting factor in the cost function is required to turn the level sets into circular ones. As the choice of the weighting factor, it is not trivial, and a poor choice may lead to suboptimal performance. In the case study, the optimization problem is tackled geometrically to bypass the aforementioned difficulties. With this choice of the evaluation function, no such weighting factors are needed and the problem is tackled by adopting a geometric approach.

The voltage vector selection is affected when using a quadratic cost function as compared with the evaluation function proposed in this thesis. The study is done based on simulations where a current controller is assumed at constant speeds. For the quadratic cost function, one similar to the one described in [4] is considered to evaluate the pair of optimal voltage vectors. These pairs are then compared with the ones calculated by the proposed evaluation function. The comparison is shown in Fig. 6.2. It is noticeable how the vector selection computed by the quadratic cost function follows the correct trend but it is less accurate and, inevitably, it will lead to higher current ripples. Hence, such methods will achieve inferior performance compared to that achieved with the cost function proposed in this work. The evaluation function, whose components can assume positive or negative values admits a pair of switching commands, and the optimum solution is

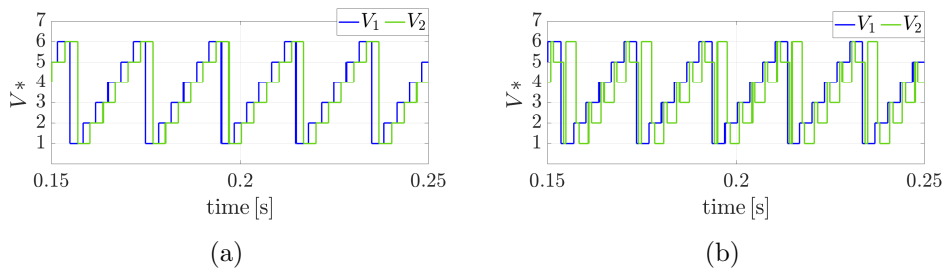


Figure 6.2: Optimum vector selection by means of (a) the proposed M-MPC (b) and [4].

found by a vectorial analysis as described in detail in the following.

The evaluation function is defined as follows

$$\mathbf{g}(n) = \begin{bmatrix} g_d \\ g_q \end{bmatrix} = \begin{bmatrix} i_{d,err}^{k+1}(n) + T_s w_d \sum_{j=0}^m (i_{d,err}^{k-j}) \\ i_{q,err}^{k+1}(n) + T_s w_q \sum_{j=0}^m (i_{q,err}^{k-j}) \end{bmatrix}, \quad (6.2)$$

The error tracking terms (i.e., $i_{d,err}^{k+1}(n)$, $i_{q,err}^{k+1}(n)$) are evaluated as the difference between the the reference signal i_d^* , i_q^* and the predictions $i_d^{k+1}(n)$, $i_q^{k+1}(n)$ evaluated for each feasible voltage vector that the 2L-VSI can provide (i.e., $n = \vec{v}_0, \vec{v}_1, \dots, \vec{v}_7$), see Fig. 3.2).

$$i_{d,err}^{k+1}(n) = i_d^* - i_d^{k+1}(n) \quad (6.3a)$$

$$i_{q,err}^{k+1}(n) = i_q^* - i_q^{k+1}(n) \quad (6.3b)$$

Just considering these adds in the evaluation function components, the algorithm results to be a proportional-like controller, whose steady-state performance is highly dependent on the accuracy of the model used in the prediction stage. To address the issue, the integral of the actual error between the references and the feedback signals (i.e., $i_{d,err}^k$, $i_{q,err}^k$) are included in the evaluation function components to compensate for any occurring steady-state errors due to model inaccuracies. In (6.2), T_s represents the sampling interval set to execute the algorithm, m is the number of samples

used to evaluate numerically the integral of the current error components $i_{d,err}^{k-j}$, $i_{q,err}^{k-j}$. Two weighting factors w_d , w_q have been included to make the evaluation function components physically consistent. They are tuned in a trial-and-error fashion and their variation can enhance the dynamic performance of which the system can compensate for model mismatches.

6.2 Duty Cycle Calculation

According to the above definition of the evaluation function (6.2), given the current references, the eight switching configurations of the 2L-VSI enable the calculation of eight pairs of coordinates shaping a hexagon into the g_d , g_q plane as shown in Figs. 6.3a and 6.8a. The vertices represent the achievable steady-state errors at the next time step by applying the corresponding active vectors indicated as $\vec{v}_1, \dots, \vec{v}_6$, while the zero vectors (\vec{v}_0 and \vec{v}_7) lay in the hexagon center. It is important to describe the behavior of the controller during steady-state and transients.

6.2.0.1 Steady-state Operation

To achieve zero steady-state error operations, the origin of the axis of the g_d , g_q plane is the target to be reached (i.e. $t_d = 0$, $t_q = 0$). The behavior here outlined refers to the operation described in Sect. 7.1 (i.e. $i_d^* = 5.5$ A, $i_q^* = 5.5$ A, $T_s = 10$ ms, $V_{dc} = 600$ V, $\omega_m = 1500$ rpm). The target coordinates can be reached through a linear combination of two of the active voltage vectors and one of the zero vectors. The sum of the time application of the two of the selected active voltage vectors and the zero vector must be one, meaning that in one sample time, three voltage vectors are applied. Referring to the Figs.6.3a and 6.3b, the target coordinates (i.e. red dot) is

reachable by applying a linear combination of the vector \vec{v}_1 and \vec{v}_6 , where $d_1(i, j)$ and $d_2(i, j)$ are the computed duty cycles corresponding to the time application of the vectors \vec{v}_1 , and \vec{v}_6 over the sampling interval T_s , represented by the orange, and the blue segments respectively in Fig.6.3b. It is possible to derive the pair of voltage vectors geometrically by solving the following linear problem for all the feasible pairs of consecutive voltage vectors.

$$\begin{bmatrix} d_1(i, j) \\ d_2(i, j) \end{bmatrix} = \begin{bmatrix} g_{i,d} - g_{0,d} & g_{j,d} - g_{0,d} \\ g_{i,q} - g_{0,q} & g_{j,q} - g_{0,q} \end{bmatrix}^{-1} \begin{bmatrix} t_d - g_{0,d} \\ t_q - g_{0,q} \end{bmatrix} \quad (6.4)$$

In (6.4), the two components of the evaluation function $g_{i,d}$, $g_{i,q}$, $g_{j,d}$, $g_{j,q}$ were evaluated for each pair of adjacent vectors (i, j) among the set $(1, 2)$, $(2, 3)$, $(3, 4)$, $(4, 5)$, $(5, 6)$, $(6, 1)$. The terms $g_{0,d}$, $g_{0,q}$ are the evaluation function coordinates for the zero vectors, while t_d , t_q are the target coordinates both set to zero. Among all the calculated duty cycles, the unique pair solution that meets the following constraints is the one that allows the machine to be controlled at the desired operating point, resulting in a three-vector voltage actuation.

$$d_1(i, j) \geq 0 \quad (6.5a)$$

$$d_2(i, j) \geq 0 \quad (6.5b)$$

$$d_1(i, j) + d_2(i, j) \leq 1 \quad (6.5c)$$

The inequalities described in (6.5) are geometrical constraints to be verified so that the solution $d_1(i, j)$ $d_2(i, j)$ lays within one of the six triangles boundaries (see Fig. 6.3a). For a specific time instant during which the drive operates at a steady state, all the computed duty cycles are depicted in Fig. 6.4 in the g_d , g_q plane to observe graphically the uniqueness of the

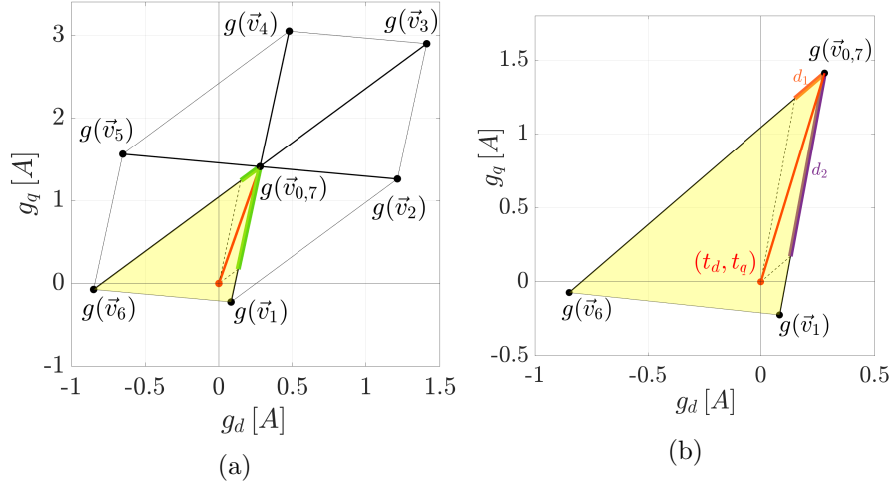


Figure 6.3: (a) Evaluation function g_d , g_q coordinates for the feasible configurations of a 2L-VSI during steady state operation; (b) duty cycle representation.

solution.

Fig 6.4a represents the optimal solution where the zero steady-state targets, depicted by the red dot in the origin of the g_d , g_q plane, lie within the triangle highlighted in green. The time application for the identified voltage vectors meets the requirements in (6.5) where both the duty cycles result positive and their sum is less than one.

In Fig 6.4b, the triangle depicted by evaluating (6.4) considering the voltage vectors \vec{v}_1 and \vec{v}_2 . In this case, the duty cycle corresponding to the vector \vec{v}_2 results negative, i.e., in the direction of \vec{v}_5 . This means that to achieve the desired target, \vec{v}_1 and \vec{v}_5 could be considered. However, this pair of voltage vectors results in a higher amount of switching states, and thus this solution is discarded.

A further case analysed the evaluation of (6.4) considering \vec{v}_2 and \vec{v}_3 represented in Fig. 6.4c. As for the previous case, the commutation from two non-consecutive voltage vectors causes higher switching losses in the system. In addition, the time application of the vectors \vec{v}_2 and \vec{v}_6 with their corresponding blue segments violates the constraint on the sampling

interval described by (6.5c).

In Fig. 6.4d, it is shown the duty cycle calculated when the voltage vectors \vec{v}_3 and \vec{v}_4 are applied. In this case, as both the time application for \vec{v}_3 and \vec{v}_4 result negative, the constraints (6.5a), (6.5b) and (6.5c) are all violated.

In Fig. 6.4e, the vectors \vec{v}_4 and \vec{v}_5 are considered. This case study is similar to the one described in Fig. 6.4b.

Finally, when the vectors \vec{v}_5 and \vec{v}_6 are applied the resulting triangle is the one highlighted in cyan in Fig. 6.4f. This case study shows similar time applications as for the case described in Fig. 6.4c.

This pattern can reduce the number of iterations required to identify the optimum pair of voltage vectors and the corresponding duty cycle application. In fact, instead of evaluating six pairs of duty cycles, three consecutive pairs of voltage vectors would suffice to seek the optimum solution. Given the symmetry to the hexagon center between the case described in Figs. 6.4a and 6.4d, the optimal solution can be found when either of the two cases are identified. The only difference when the solution described in Fig.6.4d is found consists of referring the duty cycles applications to the voltage vectors symmetrical to the hexagon center of symmetry. In such a way, the number of iterations can be halved, and the same optimal solution can still be found. Thanks to the vector analysis conducted on the g_d, g_q plane and the resulting patterns, the M-MPC can be computationally lighter and more competitive than standard FCS-MPC. The last observation on the depicted hexagon at steady-state resides in the g_d, g_q axis scales. It can be seen how the g_q axis range is wider than the g_d axis. The reason behind this difference is due to the inherent d - and q -axis inductance difference. Higher inductance on the d -axis signifies a lower error range reachable on the g_q axis. On the other hand, the lower inductance value

6.2. DUTY CYCLE CALCULATION

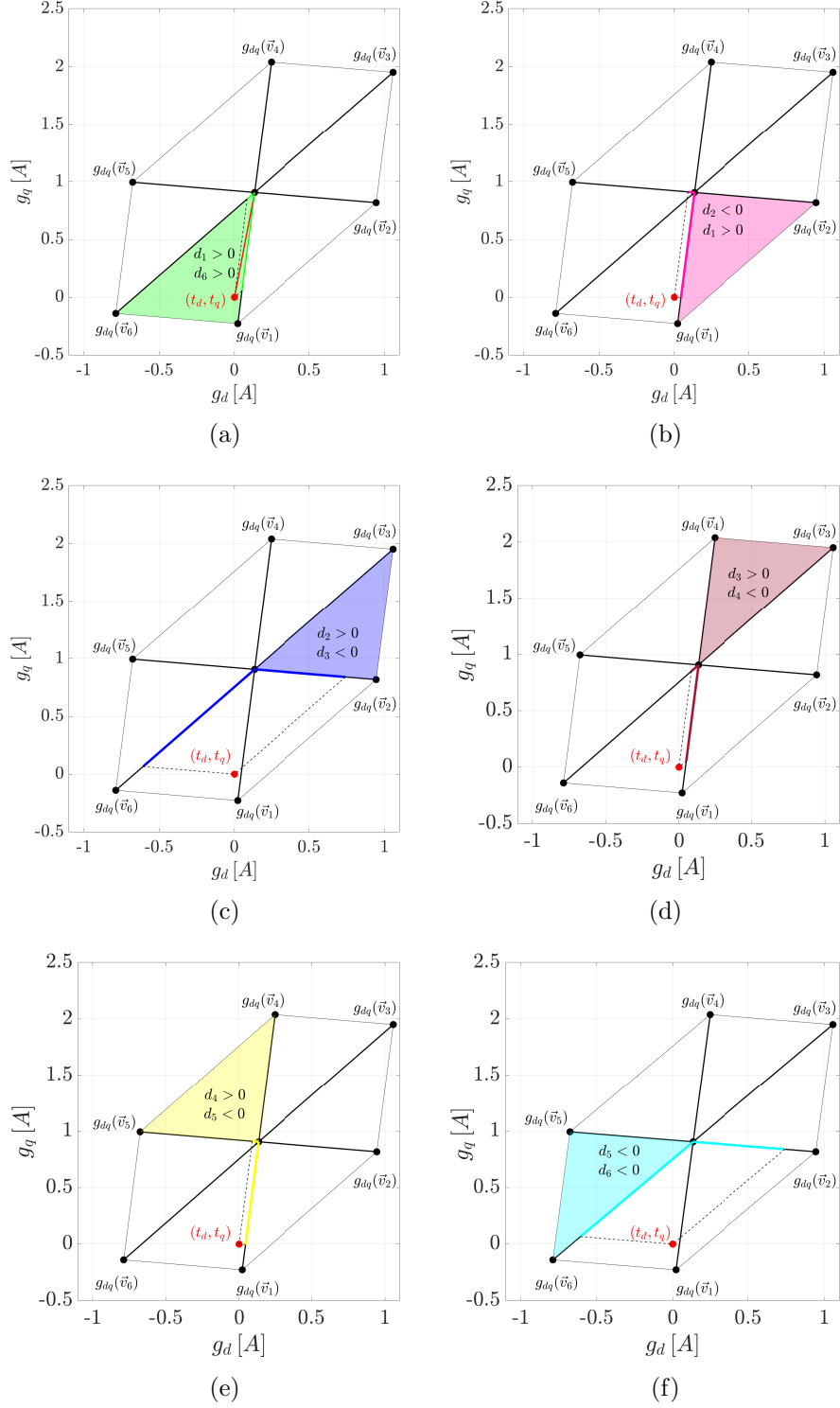


Figure 6.4: (a) Evaluation function g_d, g_q coordinates for the feasible configurations of a 2L-VSI during steady state operation; (b) duty cycle representation.

on the q -axis amplifies the error observed on the g_d axis.

An ordinary steady state operation with the available control commands

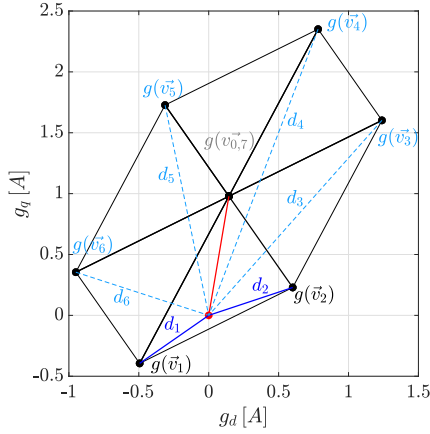


Figure 6.5: Distance from voltage actuation to the target at steady state.

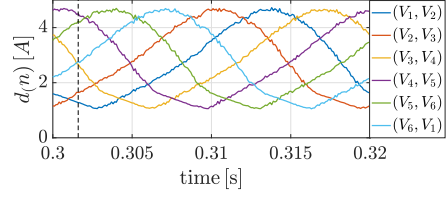


Figure 6.6: Evolution of (6.6) over time.

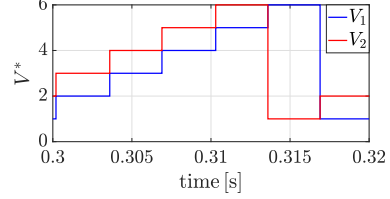


Figure 6.7: Optimum voltage vector selected.

is depicted in Fig. 6.5 for a specific time instant. In order to prove the uniqueness of the duty cycle's steady-state solution, the segments $d_1 \dots d_6$ representing the distance of each hexagon vertex from the target coordinates (i.e., the red dot) are illustrated. The sum of the magnitude of two consecutive segments can be calculated as

$$\bar{d} = d_i + d_j \quad (6.6)$$

where the suffixes i, j belongs to the set $(1, 2), (2, 3), (3, 4), (4, 5), (5, 6), (6, 1)$. The evolution of this quantity for a fixed-speed drive consists of a rotating hexagon around its center. The trend of the hexagon vertices over time is reported in Fig. 6.6. The corresponding voltage vector for the same time interval is reported in Fig. 6.7. Based on Fig. 6.5, and as shown in Fig. 6.6, it is straightforward to show that the minimum value of (6.6) is achieved by a unique pair of voltage vectors.

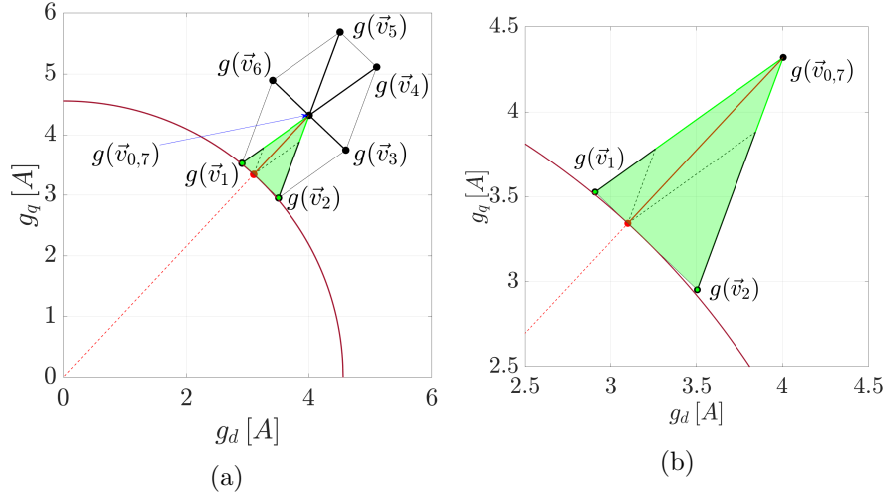


Figure 6.8: (a) Evaluation function g_d, g_q coordinates for the feasible configurations of a 2L-VSI during transient; (b) duty cycle representation.

6.2.0.2 Transient Operation

It might occur during transients that the conditions (6.5) are not satisfied for any pair of adjacent voltage vectors, meaning that the zero steady-state error is not obtainable, and the target coordinates lay outside the hexagon. Referring to the same operation as described in Sect. 7.1, but considering a time instant corresponding to the transient operation, it is noticeable how the resulting hexagon is displaced from the zero steady-state targets (see Fig. 6.8a). In this specific case scenario, a new target, displaced from the origin of the axis, has to be calculated. First of all, the closest triangle to the origin of the axis is identified by finding the voltage vectors whose corresponding duty cycles meet the requirements (6.5a) and (6.5b). In Fig. 6.8b, the resulting voltage vectors are \vec{v}_1 and \vec{v}_2 . The new target is calculated by finding the intersection between (a) the line segment that connects the origin of the g_d, g_q plane, and the zero vector coordinates, and (b) the line segment that connects the coordinates of the evaluation function obtained for the two neighboring active vectors that satisfy the condition (6.5c), see Fig.6.8b. Analytically, the new target is calculated as

follows

$$\begin{cases} \bar{t}_d = g_{0,d} + d_1(i, j)(g_{i,d} - g_{0,d}) + d_2(i, j)(g_{j,d} - g_{0,d}) \\ \bar{t}_q = g_{0,q} + d_1(i, j)(g_{i,q} - g_{0,q}) + d_2(i, j)(g_{j,q} - g_{0,q}) \end{cases} \quad (6.7)$$

Solving again (6.4), accounting for the renewed target coordinates (i.e. \bar{t}_d, \bar{t}_q), the pair of duty cycles that satisfies the conditions (6.5), are the ones applied to the machine. During transients, as the achievable target lies on the hexagon boundaries, the control action results in two-vectors voltage actuation, and the zero-vectors are never applied under these circumstances. The purpose is to make the hexagon center approach the zero steady-state error as quickly as possible and the operation goes back to the case described previously. Choosing a different target than the one described might lead to instability problems. Once the new target coordinates are calculated, the duty cycles corresponding to all the pairs of adjacent voltage vectors can be evaluated. The uniqueness of the solution also in this case during transient is proven graphically in Fig. 6.9. The first case illustrated in Fig. 6.9a shows that the pair of voltage vectors \vec{v}_4 and \vec{v}_5 whose corresponding operating area is highlighted in yellow does not allow to reach the target coordinates (i.e., red dot on the hexagon edge). The duty cycle corresponding to the application of \vec{v}_4 results negative, meaning that the pair \vec{v}_1 and \vec{v}_5 should be considered instead. The number of computations might be reduced considering this symmetry.

In Fig. 6.9b the pair \vec{v}_5 and \vec{v}_6 does not allow the system to reach the target. The pair \vec{v}_6 and \vec{v}_2 shall be used instead against the time constraint (6.5c). The optimum solution is represented in Fig. 6.9c the target lies on the edges of the triangle shaped by the vectors \vec{v}_6 and \vec{v}_1 . Moreover, the sum of the resulting duty cycle is one, meaning that no zero vectors are considered and the solution presented is physically doable. The case

6.2. DUTY CYCLE CALCULATION

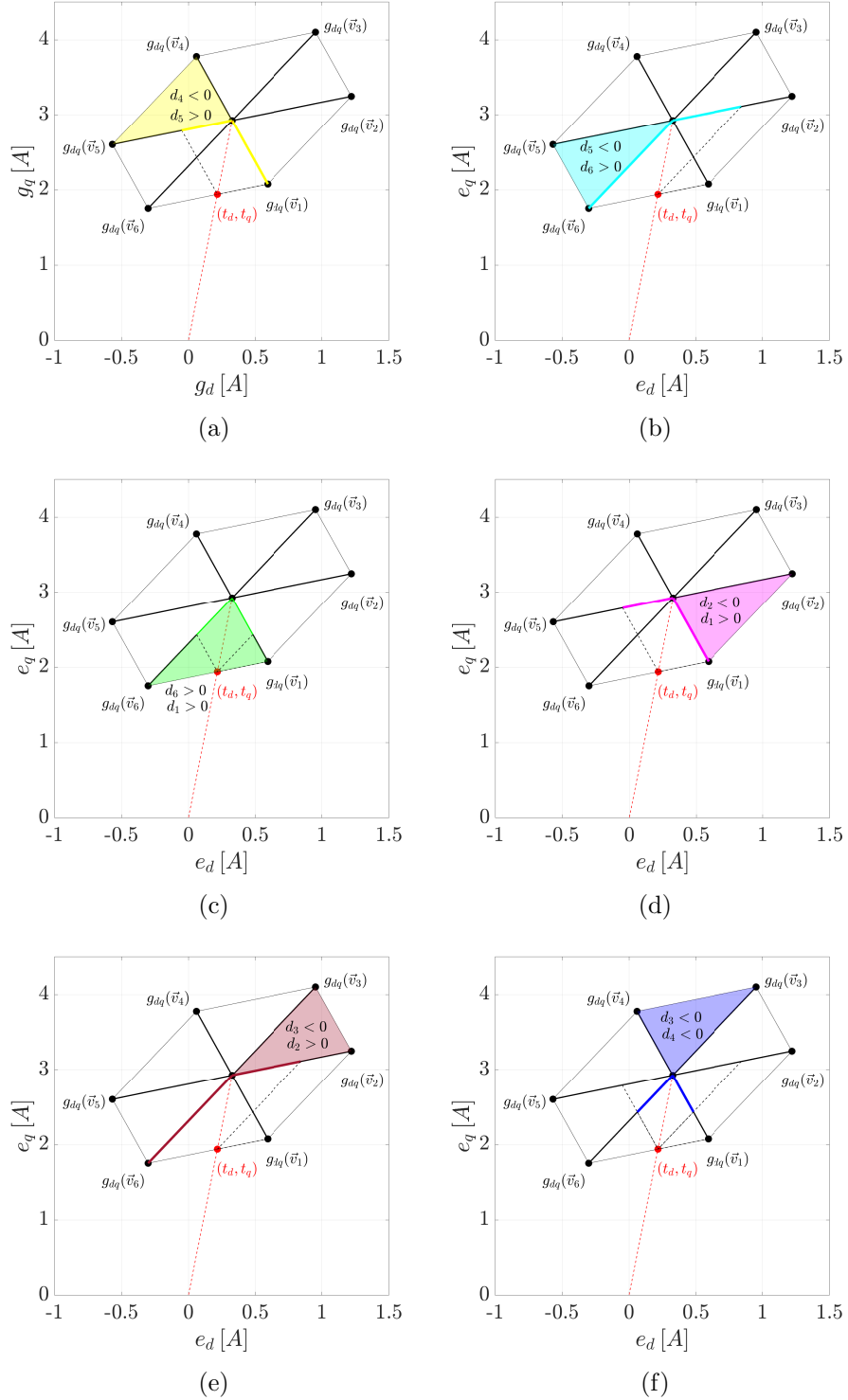


Figure 6.9: (a) Evaluation function g_d , g_q coordinates for the feasible configurations of a 2L-VSI during steady state operation; (b) duty cycle representation.

illustrated in Figs. 6.9d and 6.9e are similar to the cases shown in Figs. 6.9a and 6.9f, respectively. The last case shown in Fig. 6.9f depicts how the application of the voltage vectors \vec{v}_3 and \vec{v}_4 result in negative duty

cycles. The symmetrical vector to the hexagon center shall be used instead of making this case related to the optimal solution described in Fig. 6.9c. The same considerations on reducing the number of iterations needed to identify the optimal solution can be assumed in this case as well. The only difference is that a few more calculations need to be performed to find the new target coordinates.

Also in this case, the difference between the g_d - and g_q -axis is notable. The lower inductance axis increases the range of errors obtainable on the corresponding axis. Finally, the reference voltage vector synthesized by the modulator is calculated as

$$\vec{v}_{ij} = d_1(i, j)\vec{v}_i + d_2(i, j)\vec{v}_j + d_0\vec{v}_0, \quad (6.8)$$

where

$$d_0 = 1 - [d_1(i, j) + d_2(i, j)]. \quad (6.9)$$

As for the steady-state operation, during transient as well a unique pair of voltage vectors is found to control the system. Fig. 6.10 shows the actuating voltage hexagon for an overmodulation operation. The evolution over time of (6.6) for the possible switching states is reported in Fig. 6.11 with the corresponding voltage vectors represented in Fig. 6.12 in the same time interval. It can be observed how the renewed target coordinates guarantee a unique pair of voltage vectors satisfying the aforementioned conditions.

In Fig. 6.13, the turnaround time of the implementation of the described M-MPC on DSP was measured and the results are shown in Fig. 6.13. It can be observed how the time execution required for all the stages to evaluate the next actuation command takes about $12 \mu\text{s}$. while the sampling interval was 0.1 ms.

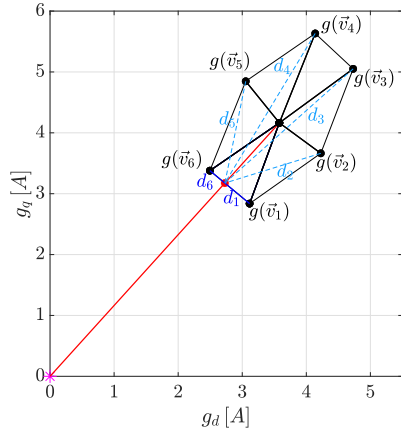


Figure 6.10: Distance from voltage actuation to the target during transient.

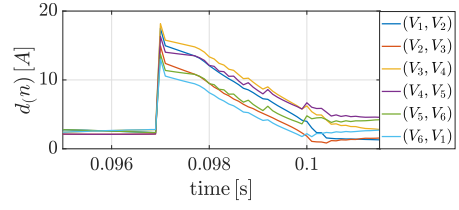


Figure 6.11: Evolution of (6.6) over time.

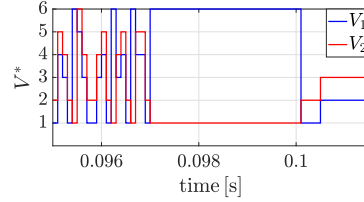


Figure 6.12: Optimum voltage vector selected.

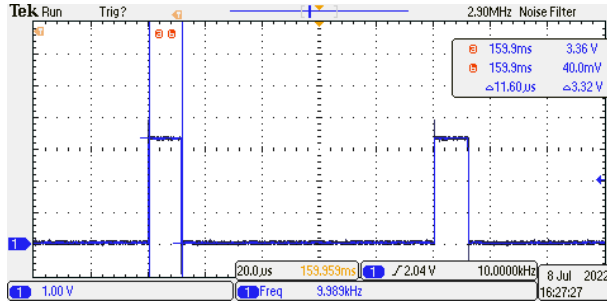


Figure 6.13: Turnaround time of the M-MPC implementation.

6.3 Chapter Conclusions

In this chapter, a detailed description of the introduced M-MPC has been described, and the corresponding flowchart is represented in Fig. 6.14. The geometrical formulation of the control problem has been tackled geometrically, enabling the inclusion of integral terms for enhanced robustness and accurate control. The target coordinate formulation permitted clearly distinguishing overmodulation and steady-state operations.

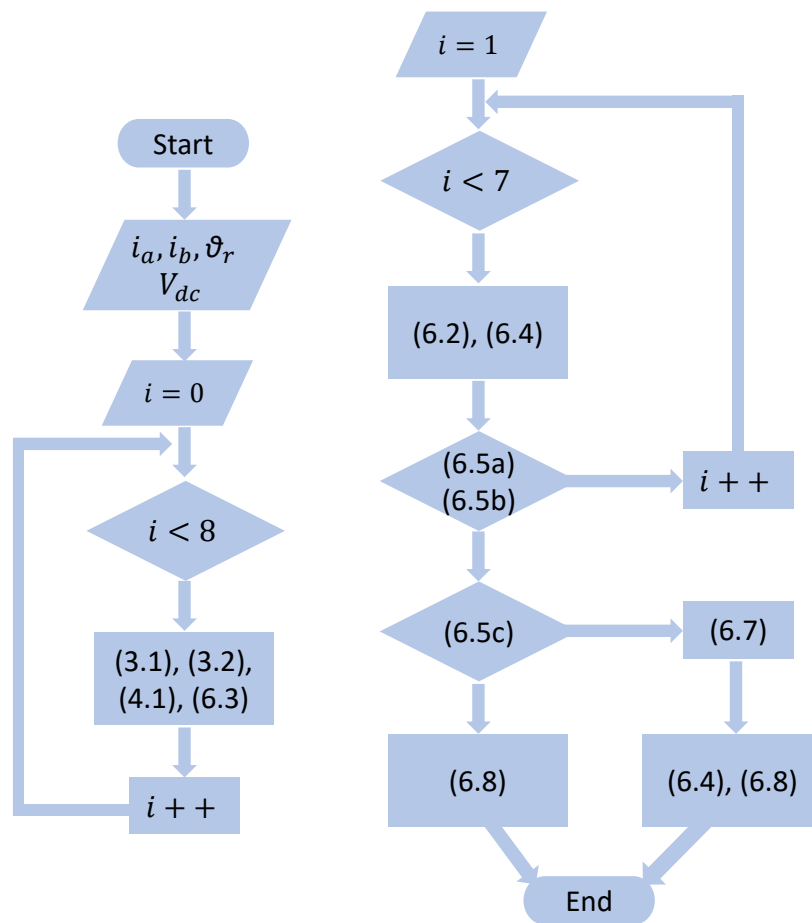


Figure 6.14: M-MPC flowchart.

Chapter 7

M-MPC Results

In this chapter, simulation and the experimental results for the M-MPC introduced in chapter 6 are shown for the same SyRel drive. The block diagram of the M-MPC method is presented in Fig. 6.1. It is assumed that the machine under test rotational speed was set by a PM speed-controlled, and the SyRel was current-controlled for operation below the base speed.

7.1 Simulation Results

In this section, simulation results show will show further details of the introduced control algorithm. First of all, the results of two sets of simulations in two different operating points are shown considering a perfect identified magnetic model as described in Sect. 3.3, and the integral of the error inclusion is neglected. Another set of simulations has been run to conduct a robustness analysis over a few of the most significant parameter variations over the identified magnetic model. It will be shown how the inclusion of the integral of the error tackles the model mismatches and compensate for them guaranteeing zero steady-state error. The same aspects have been

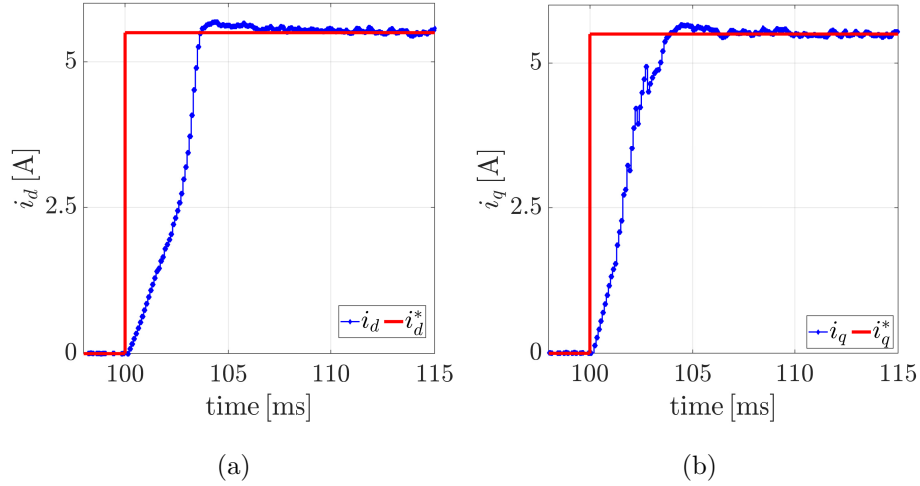


Figure 7.1: Simulation results of the d - q -current step response. (a) d -current tracking. (b) q -current tracking.

tested experimentally to validate the proposed control technique.

7.1.1 Current Control at constant speed

The implemented control strategy is studied in the current control mode for fixed-speed applications set by a prime mover. The characteristics of the SyRel are illustrated in the tab. A.1. The rotational speed was set to the rated speed $\omega_m = 1500$ rpm, the dc-link voltage was selected to $V_{dc} = 620$ V; the sampling frequency was set to $f_s = 10$ kHz, and the current references chosen to be tracked were the ones laying on current limit circle delimited by the rated current $i_d^* = 5.5$ A, and $i_q^* = 5.5$ A. Referring to Fig.7.1, the step response curves are highlighted, where the current references change from zero to 5.5 A simultaneously at the time instant $t = 0.1$ s.

The resulting hexagons for two different time instants, $t = 105.5$ ms and $t = 700$ ms, are depicted in the g_d, g_q plane of Figs. 6.3a and 6.8a. The former case illustrates the graphical duty cycle calculation at steady-state; the latter shows the controller behavior at the transient, where the reachable target calculated lays on the hexagon edge. In both cases, the

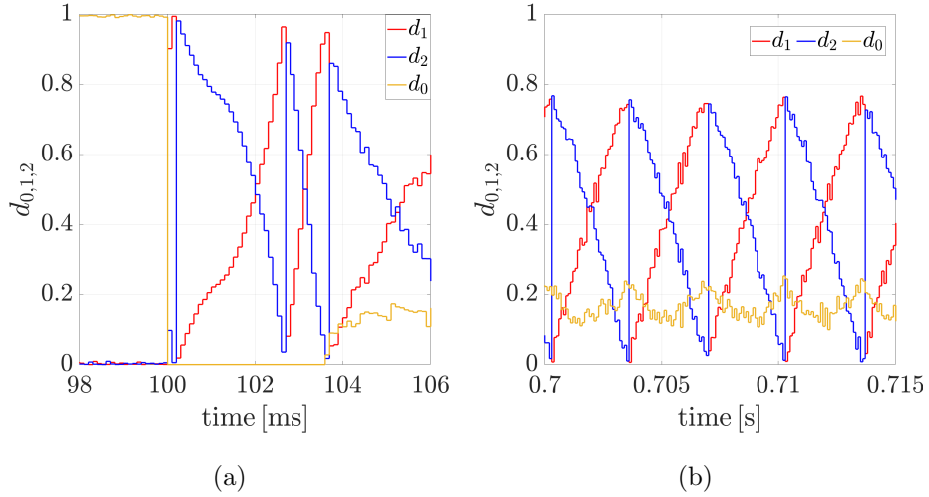


Figure 7.2: Duty cycles trend over time. (a) Transient operation. (b) Steady-state operation.

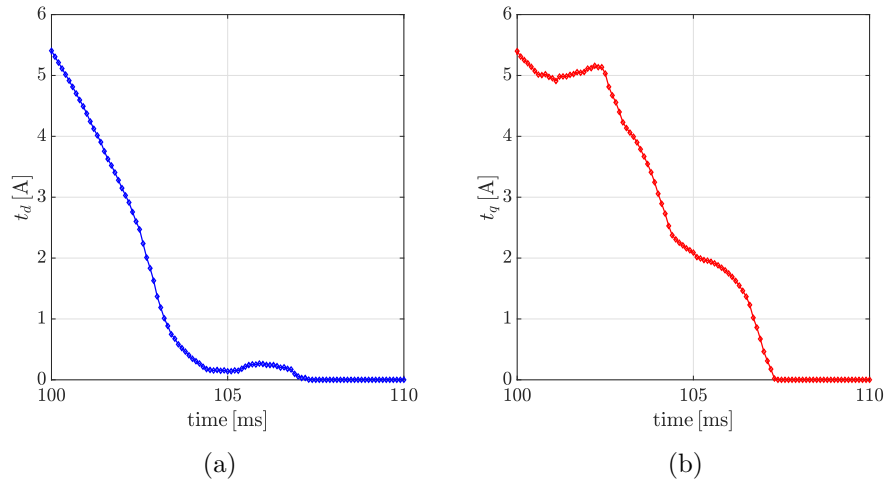


Figure 7.3: Target trend over time during transient. (a) d -component target. (b) q -component target.

orange and violet segments in Figs. 6.3b and 6.8b represent the calculated duty cycles, while the red dot indicates the target that has to be reached.

The duty cycles' time-domain trends are represented over several ms in Figs. 7.2a, 7.2b during transient and steady-state operation, respectively. Before the current command was triggered, how mostly the zero vectors were applied. After the command trigger, the two-voltage-vectors actuation is the control action selected by the controller during the transient, indeed the zero-duty component d_0 is zero up to $t \approx 104$ ms. Due to the rotation,

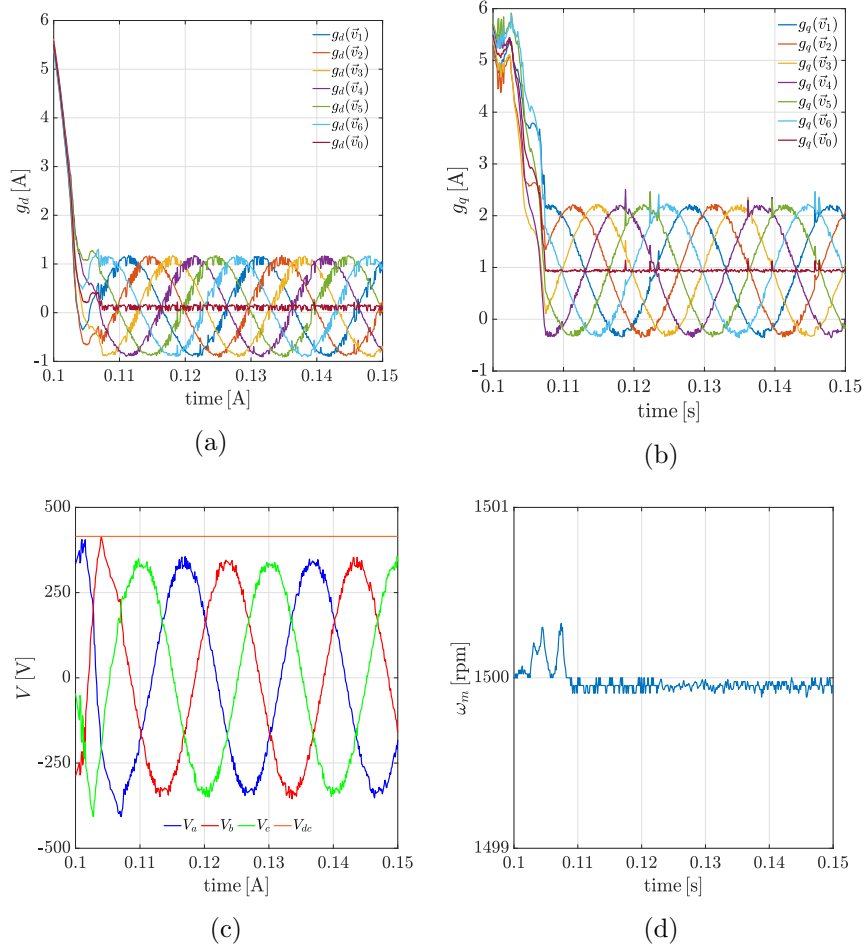


Figure 7.5: M-MPC Simulation results. (a) d -current predictions for each feasible voltage vector. (b) q -current predictions for each feasible voltage vector. (c) Phase-voltages. (d) Rotational speed.

7.5c, and the rotational speed is shown in Fig. 7.5d.

7.2 Experimental Results

The implemented control strategy was tested experimentally and the test bench configuration is described in Appendix A (see Fig. A.1).

The implemented control strategy was studied in the current-control mode for fixed-speed applications. Several operating points were tested. For all the tests described in the following, the rotational speed was set by

the prime mover, the dc-link voltage source was set to $V_{dc} = 300V$ by a dc power supply, and the sampling frequency of the control platform was set to $f_s = 10$ kHz. For the tests, two current measurements (16 bits resolution), the dc-link voltage (16 bits resolution), and the angle detected by an absolute encoder (18 bits resolution) are the available feedback signals aimed to compute the switching commands sent to the 2L-VSI through an optic signal. The compensation angle as described in (6.1) was considered as well as an LPF to smooth the speed ripple and achieve higher robustness [86].

To evaluate the goodness of the presented M-MPC, a comparison in terms of total harmonic distortion (THD) against the benchmark was conducted. The control reference scheme used for comparison was the one implemented in [89] based on PI controllers tuned with the pole-placement method, by setting the damping ratio ($\xi = 0.707$) and the controller bandwidth ($f_0 = 180$ Hz). The current THD definition is reported below:

$$\text{THD}_i = \frac{\sqrt{\sum_{j \neq 1} i_j^2}}{i_1} \quad (7.1)$$

where i_1 is the fundamental of the current waveform, and i_j is the j^{th} harmonic content.

7.2.1 Linear Modulation: Test 1

The first experimental test consists of tracking the d - q -current references while the rotational speed was fixed by the prime mover (i.e., $\omega_m = 900$ rpm, see Fig.7.6c). The resulting d - and q - current step response curves both with PI and M-MPC are shown in Figs. 7.6a, 7.6b. The line-to-line voltages V_{ab} , V_{bc} , V_{ca} , as well as the measured dc-link voltage obtained by employ-

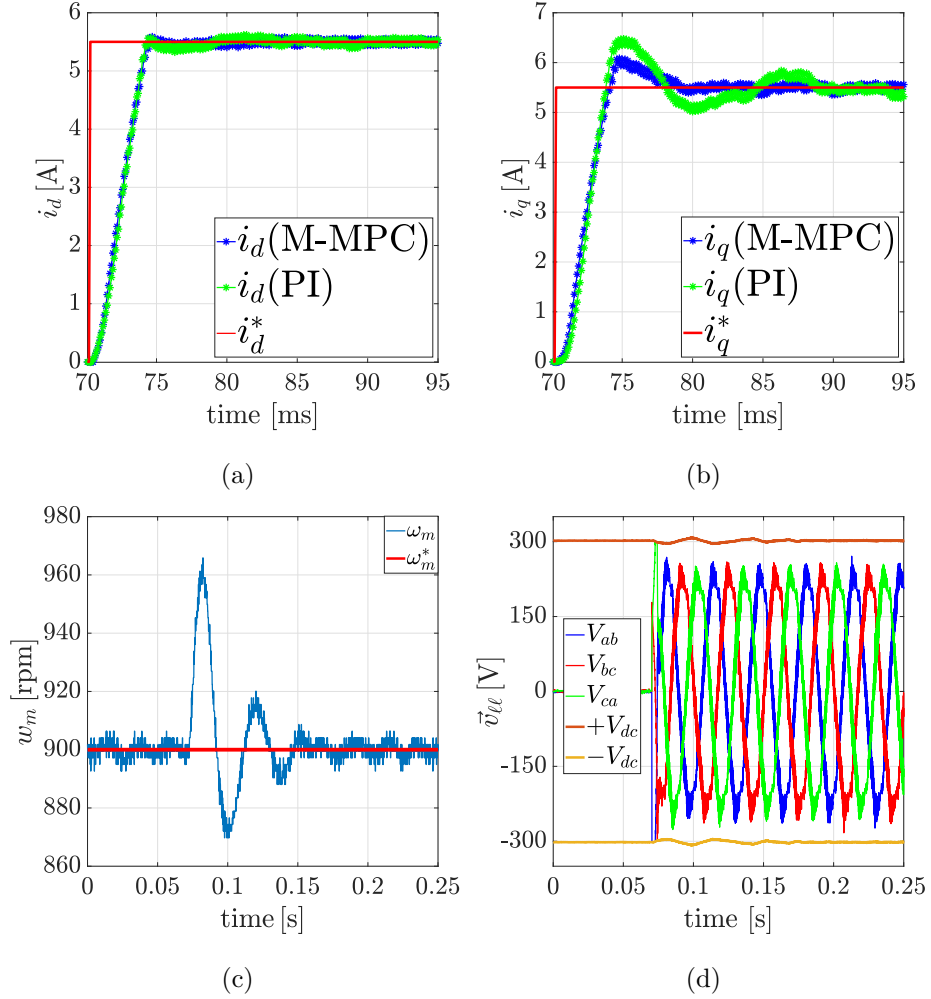


Figure 7.6: Experimental results of the d -, q -current step response at 900 rpm. (a) d -current step response M-MPC versus PI. (b) q -current step response M-MPC versus PI. (c) Rotational speed transient. (d) Line-to-line computed voltages.

ing the M-MPC are shown in Fig. 7.6d. It can be observed from the step response curves that a comparable rise time is achievable with both the controllers, with a faster settling time achieved by adopting the M-MPC, noticeable especially on the q -current component.

The duty cycle calculation was also shown during the transient and steady-state in Figs. 7.7a, 7.7b respectively, as well as the optimum voltage vectors \vec{v}^{opt1} , \vec{v}^{opt2} selection (see Figs. 7.7c, 7.7d). Referring to Fig. 7.7a, it can be observed how the zero duty d_0 was about zero until when the transient is extinguished when the zero duty is non-zero, and the null steady-state

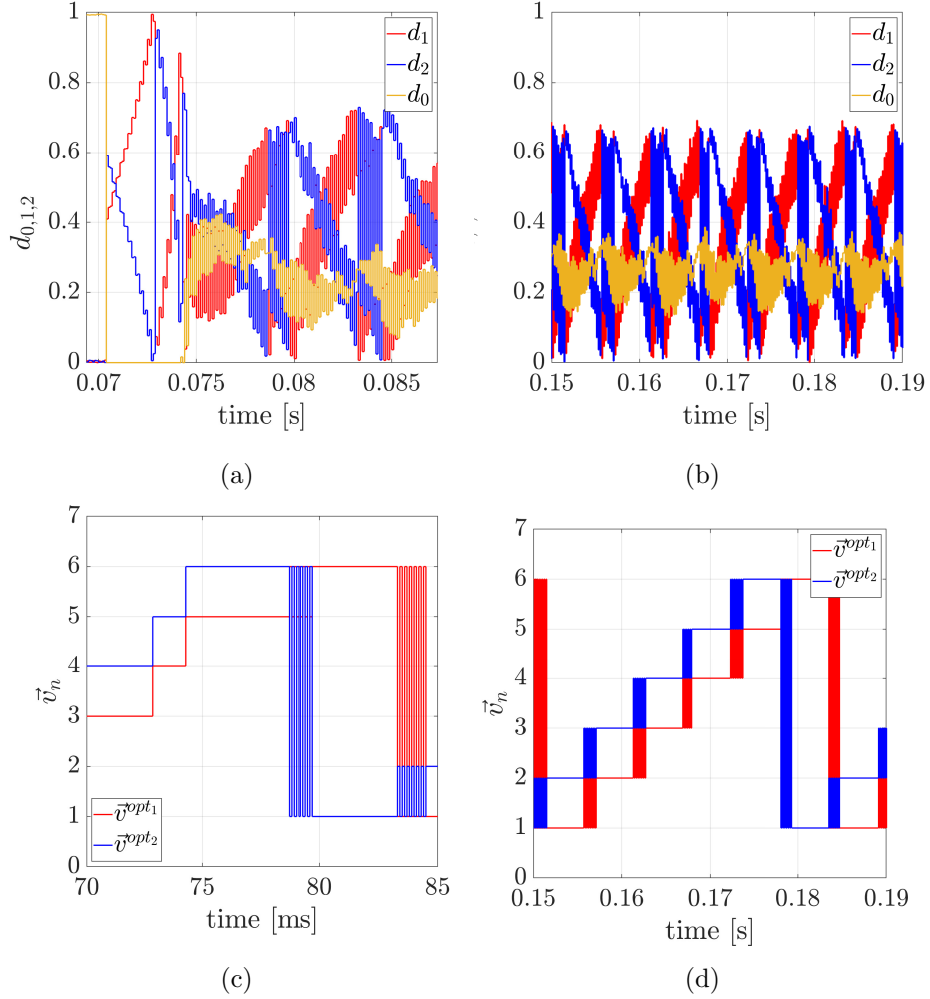


Figure 7.7: Duty cycles trend over time. (a) Transient operation. (b) Steady-state operation. (c) Optimum vectors selection during transient. (d) Optimum vectors selection during steady state.

error target, lying within the hexagon boundaries, is feasible. During the steady state interval, the duty cycles are also shown (see Fig.7.7b). Each time a new pair of adjacent vectors is applied, the d_1 component increases at the expense of the d_2 component.

The measured b -, c -phase current waveforms obtained by employing the M-MPC are shown in Fig.7.8a, whose harmonic spectra is reported in Fig. 7.8b. The measured b -, c -phase currents harmonic spectra achieved by PI controllers are shown in Fig. 7.8c. The resulting THD obtained with the M-MPC is about 50% lower than the one calculated employing PI controllers,

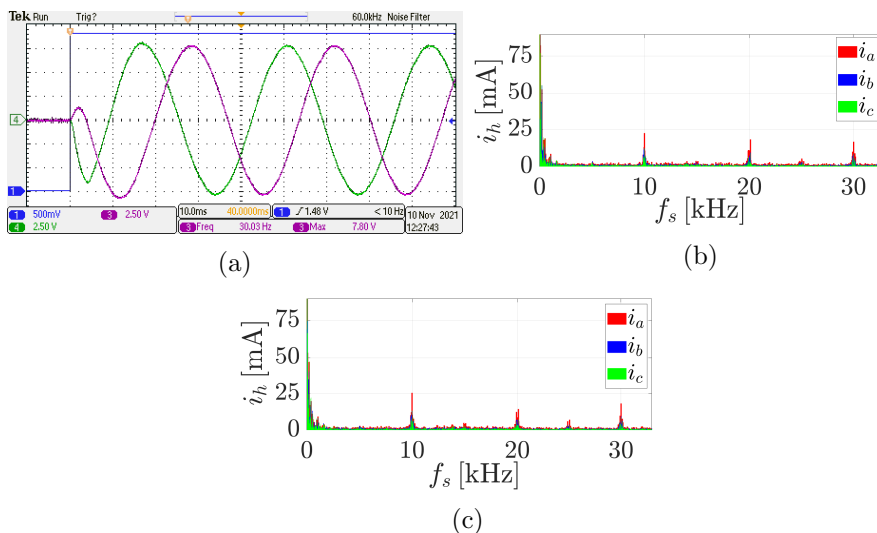


Figure 7.8: (a) M-MPC a -, b -, c -phase measures at 900 rpm. (b) b - c -phase currents harmonic spectra M-MPC (THD= 0.57%). (c) b - c -phase currents harmonic spectra PI (THD= 1.48%).

and faster dynamic performance is achievable.

7.2.2 Linear Modulation: Test 2

Another d - q -current step response test comparison was conducted for the same current references $i_d = 5.5$ A, $i_q = 5.5$ A, but at lower rotational speed ($\omega_m = 300$ rpm). As shown in Figs. 7.9a, 7.9b, the dynamic performance of M-MPC are slightly superior than PI controllers. The measured b - and c -phase currents are also shown in Fig. 7.10a with the harmonic spectra in Figs. 7.10b, and 7.10c respectively. Also in this case an improvement in the THD is obtained when the M-MPC is employed, precisely, a drop of about 60% can be obtained by choosing to implement the studied control algorithm.

Comparing simulation and experimental results (e.g., Figs. 7.2 and 7.7) higher duty cycle fluctuations can be noticed in the experimental results because they are affected by the noise in the measurements. In addition, differently from the simulation model, the current and the voltage sensors

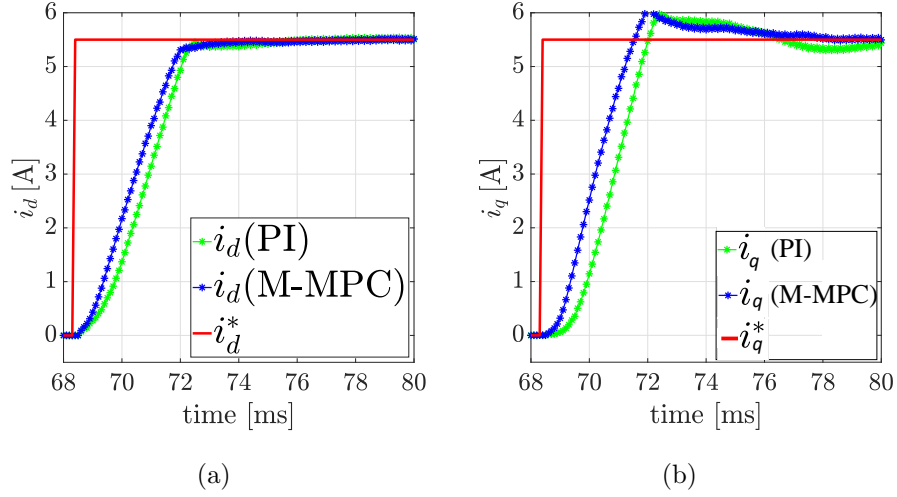


Figure 7.9: Experimental results of the d -, q -current step response at 300 rpm. (a) d -current step response M-MPC versus PI. (b) q -current step response M-MPC versus PI.

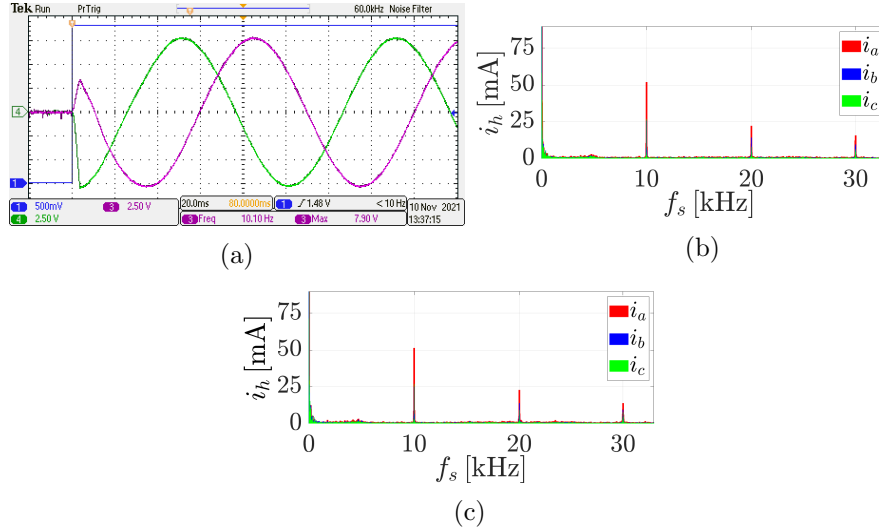


Figure 7.10: (a) M-MPC, b -, c -phase measures at 300 rpm. (b) a -, b -, c -phase currents harmonic spectra M-MPC (THD= 0.30%). (c) a -, b -, c -phase currents harmonic spectra PI (THD= 0.65%).

were acquired with 16 bits of accuracy. Furthermore, the position of the rotor used for the coordinate transformations was also characterized by a finite accuracy (i.e., 18-bit). In addition, the speed was calculated from the mechanical angle through a discrete differentiation leading to further variable fluctuations affecting the system predictions. All the practical aspects described above do not add any meaningful concept to the simulation results, besides the increased complexity. For this reason, they have not

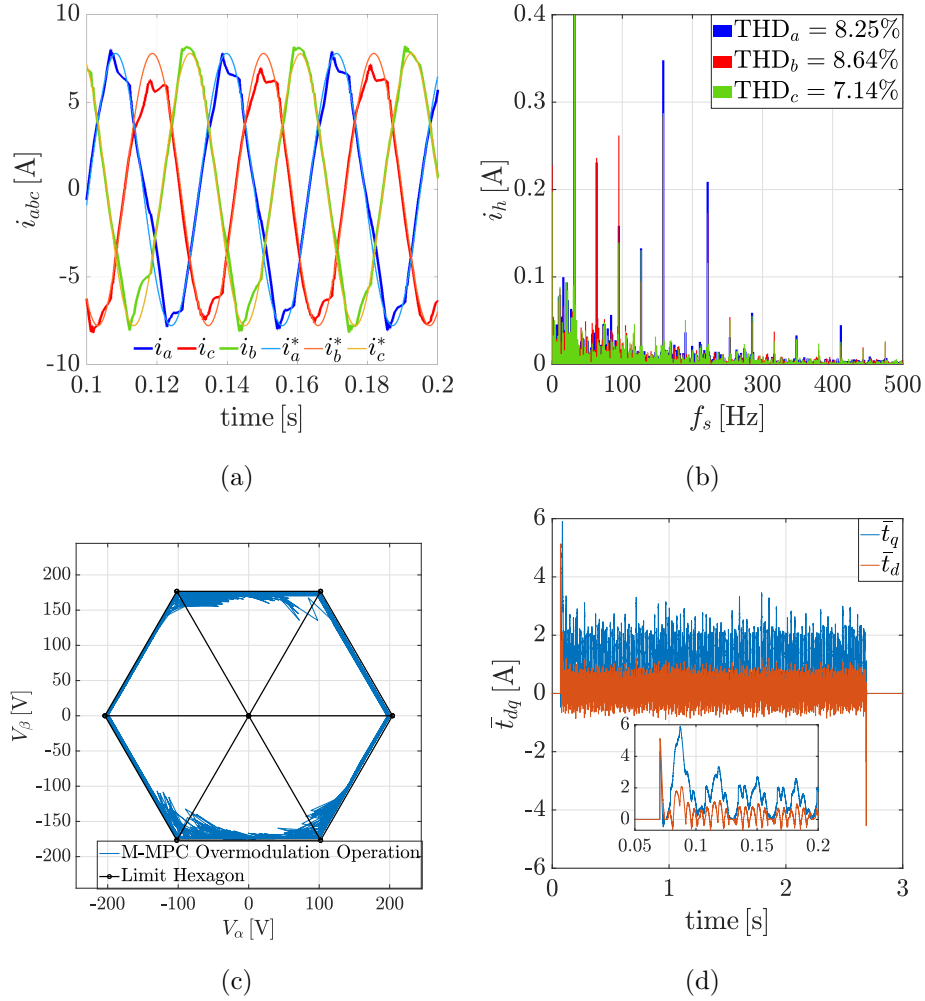


Figure 7.11: Overmodulation test results. (a) *abc*-current tracking. (b) *abc*-current harmonic spectra. (c) Voltage actuation hexagon. (d) Target coordinates evolution over time.

been modelled and the discrepancy between simulation and experimental results can be considered acceptable.

7.2.3 Overmodulation: Test 3

Another test was run to show the SyRel drive operating in the overmodulation region with the voltage command saturated. The test was carried out considering the same setup settings as for the previous tests (i.e., $V_{dc} = 300$ V, $i_d^* = i_q^* = 5.5$ A, $f_s = 10$ kHz). The PM fixed the rotational speed at 950 rpm, and the phase-current component tracking curves are

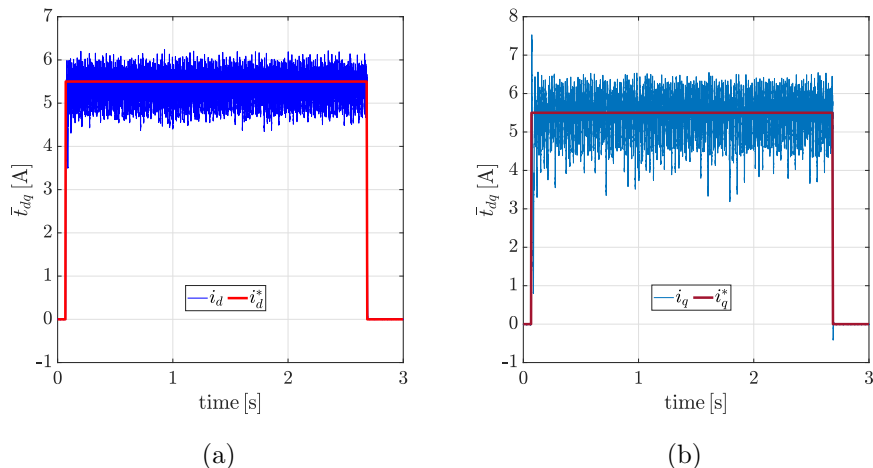


Figure 7.12: Experimental results of the d - q -current behavior in overmodulation with the proposed M-MPC method. (a) d -current tracking. (b) q -current tracking.

shown in Fig. 7.11a, and the corresponding harmonic spectra of the measured current are represented in Fig. 7.11b. It can be observed how the current distortion significantly increased compared to the former cases, given the saturation of the voltage command, and the lower number of voltage pulses. The voltage actuation hexagon in the stationary reference frame is shown in Fig. 7.11c, proving how the applied reference voltage vector over a mechanical period mostly lies on the edges of the hexagon. Looking at the introduced target coordinates evolution over time, shown in Fig. 7.11d, it can be deduced how mostly the two-voltage actuation is applied when the current commands are triggered. The target coordinates oscillation is due to the rotational speed and dc-link voltage fluctuations. The d - and q -current reference tracking are shown in Fig 7.12. The same high current distortion trend is noticeable in the synchronous reference frame. In control methods such as PI-based FOC and deadbeat, the output of the controller and the modulation stage are two decoupled entities acting independently from each other, i.e., in an uncoordinated manner. Thus, when the voltage synthesized by the modulator is different from the voltage commanded by standard controllers, the best possible dynamic performance is not guar-

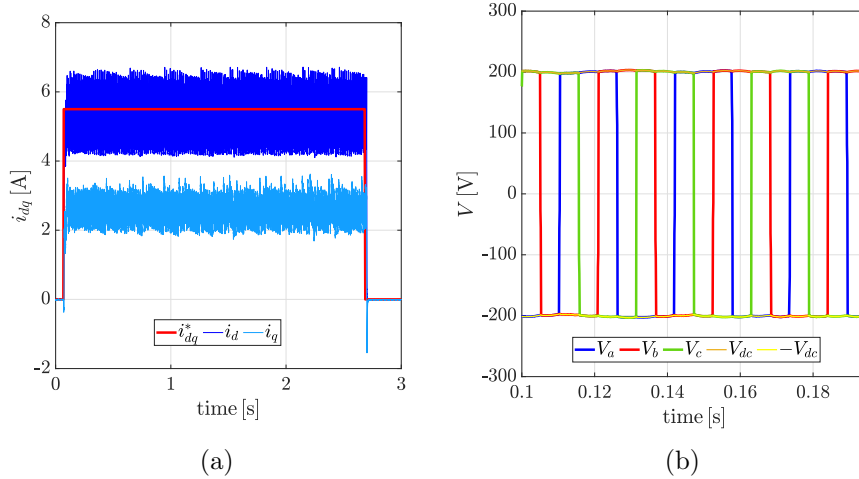


Figure 7.13: Experimental results with deadbeat control in linear modulation region. (a) dq -current tracking. (b) abc -reference voltage.

anted because the basic current transition phenomena are neglected. On the other hand, the proposed M-MPC enables the full exploitation of the available dc-link voltage, acknowledging the coordinated control and modulation achieved by means of the introduced target coordinates.

Under the same conditions, the SyRel drive was also tested by using the deadbeat control algorithm [18], where the system model is the same as the one used for the proposed M-MPC. The results are reported in Fig. 7.13a. It can be observed how the controller is not able to operate the drive at the desired operating point; the drive operates exclusively in six-step operation as can be seen in Fig. 7.13. Finally, the FOC based on PI controllers failed to track the references under the same conditions, as indicated by the results shown in Fig. 7.14.

7.2.4 Linear Modulation: Test 4

In this set of tests, a comparative analysis was conducted to take into account two further aspects. First of all, the third harmonic injection was considered downstream of the reference voltage vector calculation. In

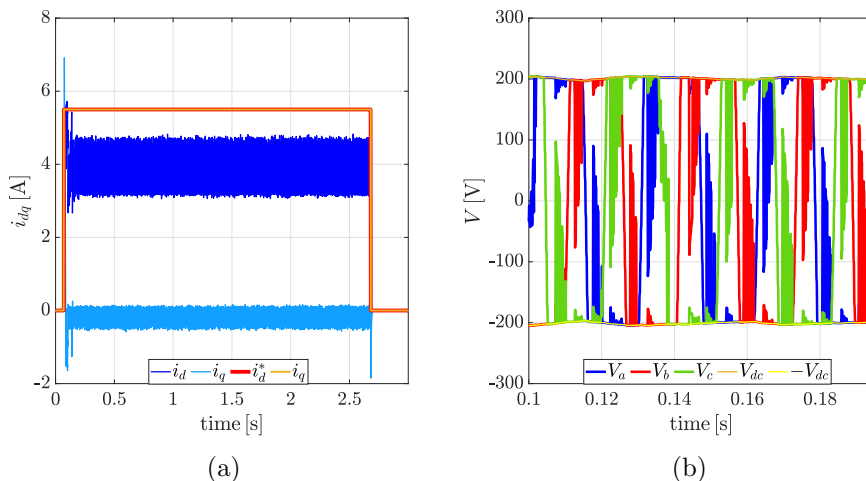


Figure 7.14: Experimental results with FOC control in linear modulation region. (a) dq -current tracking. (b) abc -reference voltage.

this way, the drive could be run at higher speeds for the same dc-link voltage level without saturating. The M-MPC experimental results are shown in Fig. 7.15. It consists of a current control mode at constant speed (i.e. $\omega_m = 950$) with the dc-link voltage set to $V_{dc} = 300$ V, and the sampling frequency set to $f_s = 10$ kHz. The measured three-phase current components are shown at steady-state in Fig. 7.15a and the corresponding harmonic spectra in Fig. 7.15b. In the same figure, the THD calculation for each phase-current component is also reported. In Fig. 7.15c, the phase reference voltages are shown as well as the upper and the lower limits given by the dc-link measurement. Differently from the previous results, a common-mode signal based on the third harmonic injection was considered. Finally, in Fig. 7.15d it is shown the d - and q -current components reference tracking. The d -current command was set to $i_d = 3.5$ A while the q -current reference was set to $i_q = 6.96$ A whose resulting magnitude corresponds to the rated current $I_n = 5.5$ A (RMS). The results achieved for the Deadbeat control are also shown in Fig. 7.16. In particular, Figs. 7.16a and 7.16b report the current waveform and the corresponding harmonic spectra for the Dead-beat control. The reference voltage are shown in Fig. 7.16c,

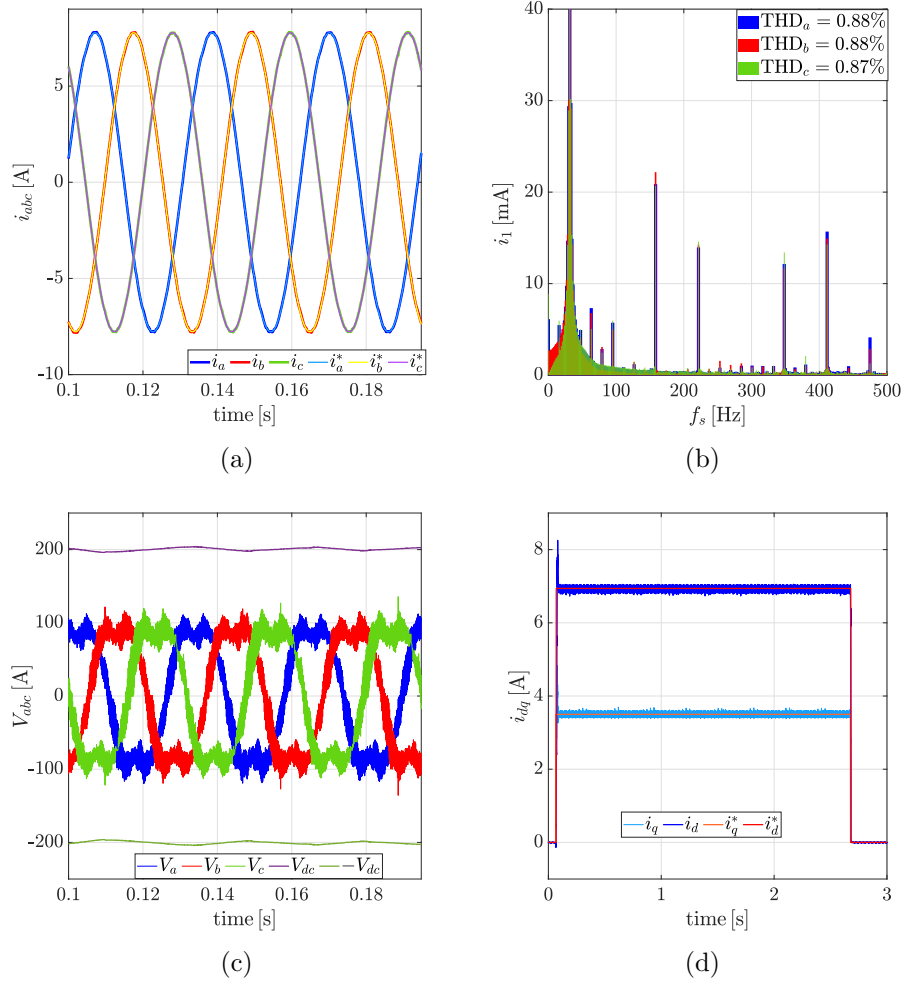


Figure 7.15: Experimental results with the proposed M-MPC method. (a) abc -current tracking. (b) abc -current harmonic spectra. (c) abc -reference voltage. (d) dq -current tracking reference.

and the dq -current tracking is depicted in Fig. 7.16d. The same test was performed for the PI-based FOC control and the results are shown in Figs. 7.17a, 7.17b, 7.17c and 7.17d. From the shown results can be deduced that the proposed controller is able to provide lower current distortions (about 15% less than the standard controllers) in the considered operating region.

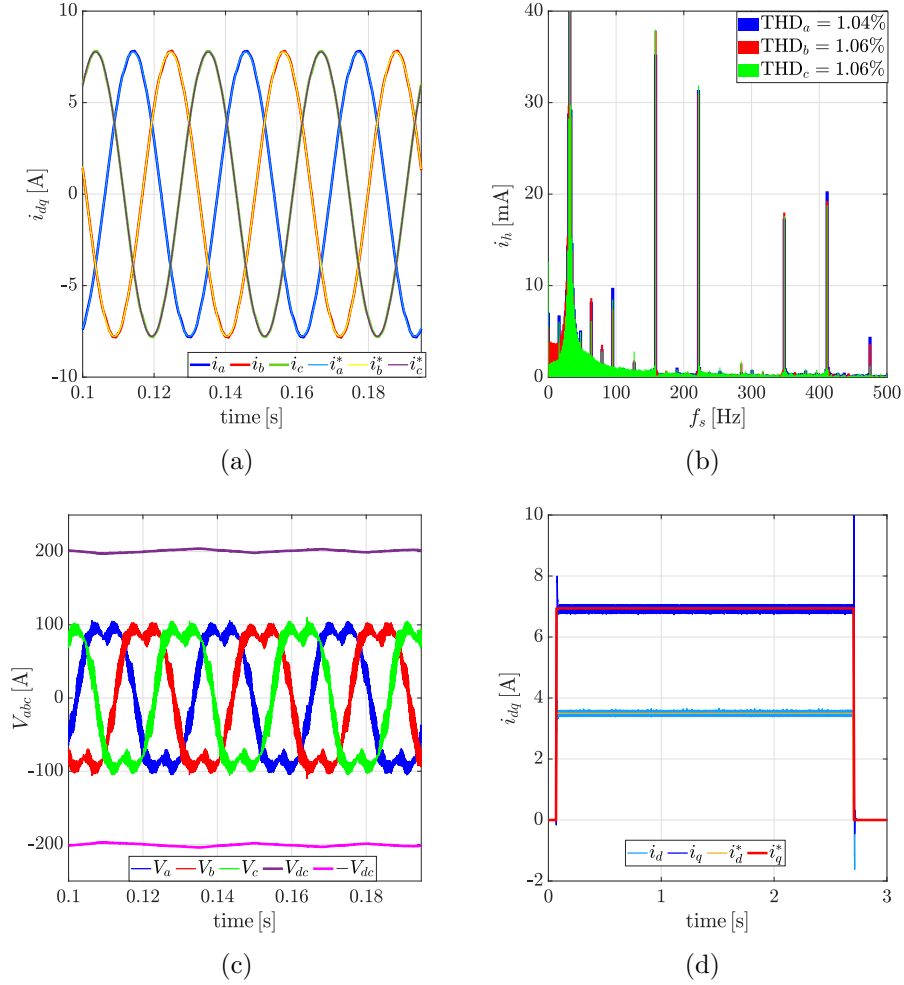


Figure 7.16: Experimental results. (a) deadbeat abc -current tracking. (b) deadbeat abc -current harmonic spectra. (c) deadbeat abc -reference voltage. (d) deadbeat dq -current tracking reference.

7.2.5 Integrals inclusion and Robustness Analysis

The integral action is the previous output plus the integral gain times the new error. Considering the previous output is the output of $2T_s$ ago plus the gain times the previous error, we can imagine that an integral action contains the accumulation of errors of each sampling period. The symbol m introduced in (6.2) is to express this accumulation action. It represents the number of the sample during the test and it starts from 0 at time zero and then increments during the whole experiment. It is initialized to zero at the beginning of each period (due to the 2π -periodicity of the pattern)

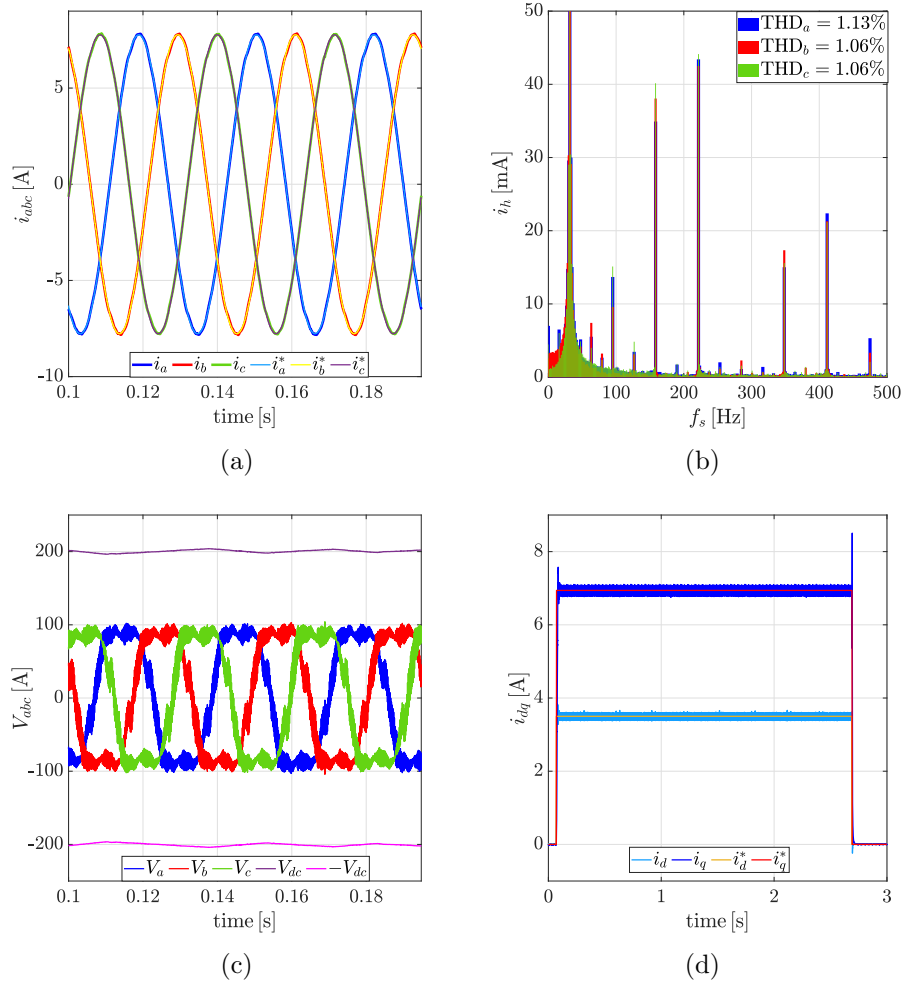


Figure 7.17: (a) FOC abc -current tracking. (b) FOC abc -current harmonic spectra. (c) FOC abc -reference voltage. (d) FOC dq -current tracking reference.

to avoid overflow problems occurring during prolonged operations. In other words, this symbol is not a parameter to tune. It is included to express the accumulation action of common integral action.

As for the tuning of the weights, it is done by trial and error in this thesis. In Fig. 7.18 are shown the effect of the weighting factors w_d and w_q on the dynamic performance after introducing a $+50\%$ error on both d - and q -flux components. The figure shows on the q axis how the introduced error without the integral action (i.e. $w_d=w_q = 0$) leads to a reference tracking error. By considering increasing values of the integral weights, the system converges to the reference value. Higher weights corrects the model

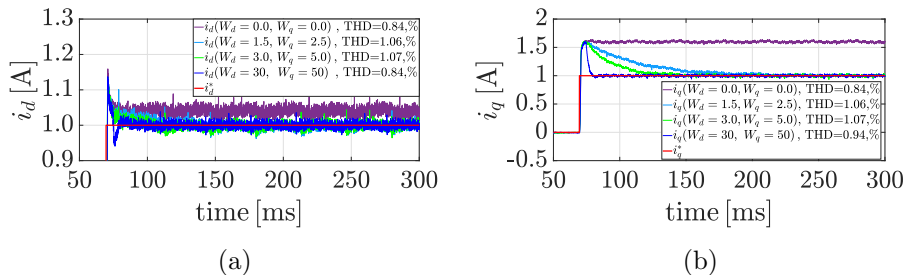


Figure 7.18: Dynamic current errors' correction for 50 % overestimated magnetic flux for various correction weights' pair. (a) d -current component. (b) q -current component.

inaccuracy faster.

The effectiveness of the inclusion of the integral terms in (6.2), will be assessed to prove how the controller responds to model mismatches in the prediction. As far as the variables in (3.5) are concerned, the incremental inductance matrix \mathbf{L} was not chosen to be included in the robustness analysis, since the sole effect of varying the incremental inductance matrix increases the current ripple, without affecting the reference tracking, as stated in [71]. The stator resistance influences the reference tracking, but its effect is more significant at low speed. Hence, errors of +50% on the d - and the q -flux components were introduced in the prediction calculations, and a set of tests was launched by varying the integral weighting factors w_d, w_q .

The achieved d - and q - step-response curves are shown in Figs. 7.18a and 7.18b, respectively. It can be noticed, especially from the q -current component, how the higher the weighting factor, the faster the system state converges to the references. Without the integral action ($w_d = 0, w_q = 0$), the system is not able to deal with the introduced model mismatch. The reason why the q -components show a higher impact on the reference tracking than the d -axis current is due to the difference of inductance components L_{dd}, L_{qq} inherent in SyRel.

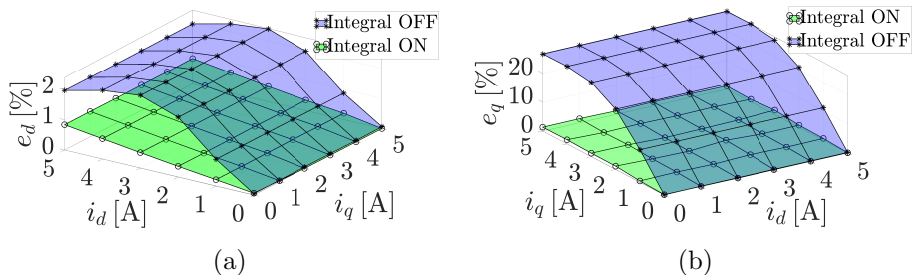


Figure 7.19: Steady-state errors with a 50% overestimated magnetic flux. (a) d -axis current error. (b) q -axis current error.

Another set of tests was run to prove how the inclusion of integral terms leads to lower steady-state error in the whole current operating domain at a fixed speed ($\omega_r = 900$ rpm). The d - and the q -current error are computed as root-mean-square (RMS) errors normalized with respect to the rated current I_n as

$$e_d[\%] = \frac{1}{N} \sqrt{\frac{\sum_k^N (i_d^* - i_d^k)^2}{I_n}} 100 \quad (7.2a)$$

$$e_q[\%] = \frac{1}{N} \sqrt{\frac{\sum_k^N (i_q^* - i_q^k)^2}{I_n}} 100 \quad (7.2b)$$

and the results are shown in Figs. 7.19a 7.19b.

It can be evinced that the inclusion of the integral terms effectively deals with the model inaccuracies. The errors observed in the case of disabling the integral terms are due to a lack of the converter non-linearities characteristics, and magnetic model mismatches. The q -axis error is larger than the d -axis due to the fact that the q -axis incremental inductance is smaller than the d -axis component, and variation in the q -flux components leads to wider current predictions' fluctuations.

7.3 Chapter Conclusions

In this chapter, simulation and experimental analysis have been conducted to validate the proposed M-MPC. Standard step response tests have been shown in both simulation and experimental results to highlight the introduced formulation of the duty cycles, the introduced concept of target coordinates, and the integral terms included in the evaluation function. Comparative analysis towards benchmark control algorithms such as the PI-based FOC and the deadbeat control methods have been performed. Higher steady-state performance as well as the dynamic response can be achieved with the proposed controller. Further comparisons in the over-modulation region have highlighted that the proposed controller uses the dc-link bus voltage better than its counterparts because of the introduced saturating mechanism relying on the target coordinates.

Chapter 8

Conclusions

In this thesis, two control approaches have been investigated aimed at improving the dynamic and the steady-state performance of a SyRel motor drive. The difficulty of dealing with a highly non-linear system has been tackled. In particular, the non-linear characteristics have been identified through a standard procedure for PMSM drives, and the results were included in the implemented control algorithms as look-up tables.

An improved FCS-MPC was implemented and tested showing how the performance of a non-linear motor can be significantly improved. The controller relied on the definition of a cost function consisting of three terms: reference tracking terms, integral terms, and a control effort term.

The drive was investigated and tested in current-control mode at a fixed speed set by the prime mover.

The proposed integral term into the cost function can compensate for any system non-idealities and unmodeled dynamics which would negatively affect the system performance while keeping low computational complexity. In particular, the flux vector model mismatches were introduced in the

system prediction to test the effectiveness of the introduced integral terms. Results showed that model inaccuracies can be successfully balanced. Furthermore, straightforward weighting factors selection can be followed. The general guidance for this tuning relies on how accurately the model is identified. Higher weights adjust the reference tracking offset more aggressively but if they are set too high, instability issues might appear. Lower weights compensate for the inaccuracies slower.

Lower output current distortion and granularity of switching are achieved enabling smoother operations with minimized power losses thanks to the inclusion of a control effort weighting factor within the cost function. Also, the control effort weighting factor tuning is tuned in a trial-and-error fashion.

An extensive test campaign endorses the proposed control approach assessing its validity for a wide variety of operating conditions. The system was tested in the whole current operating region and the performance variation showed that the higher-axis inductance is the most sensible axis for performance variations with the operating point. Operation on the MTPA should always be considered given the narrower d -axis current range where the drive will operate.

Given the non-constant switching frequency feature of the FCS-MPC, an innovative M-MPC was investigated. A novel duty cycle formulation was studied also to bypass the tuning difficulty of the cost function weighting factor. Simulation and experimental tests are carried out and the results proved the effectiveness of the proposed duty cycle computational approach, and how it can outperform standard controllers such as PI-based and deadbeat controllers achieving lower THD, and faster dynamic response. Also, in this case, integral terms have been included to deal with

model inaccuracies, addressing an inherent predictive controller drawback over some variable uncertainty, supported by a robustness analysis conducted via experimental tests. The achieved performance makes the proposed control technique an alternative solution for non-linear systems such as SyRM drives.

Some aspects of the proposed controllers need further analysis. For instance, the tuning procedure for the introduced integral of the error terms ideally should be based on procedures widely recognized, standardized, and applicable. The trial-and-error method is well-suited for the case study, but the optimum output design is not straightforward. These aspects should be considered for future investigation on this topic to simplify the design of these control methods.

Powerful recursive observers such as EKF in combination with the described control algorithms could be considered to avoid magnetic identification procedures.

The same FCS-MPC implementation on FPGA devices would enable higher granularity of switching. Furthermore, the FPGA computational power enables longer prediction horizons. Previous studies (see [44]) have shown how this aspect combined with the control effort term can enhance the steady-state performance further.

Another important issue not considered in this thesis but of high interest in SyRel motor drives is the low power factor. A few works on the topic have been recently published where it has proved the feasibility of dual-inverter topologies aimed at compensating the reactive power while extending the constant-torque curve. However, the additional complexity would make standard controller design even more troublesome. For this reason, the predictive controllers explained in this thesis can be adapted to enable

operations at low power factor and extended constant torque operations.

Appendices

Appendix A

Experimental Setup

In this appendix, the experimental setup, as well as the standard control strategies adopted to control the prime mover and the SyRel under tests, are briefly described.

The experimental rig (Fig. A.1) consists of a surface-mounted synchronous machine servo motor acting as a prime mover PM coupled to the SyRel and driven by a 2L-VSI industrial drive (ID). Similarly, the SyRel motor is driven by a SiC 2L-VSI prototype ([90]). The SiC 2L-VSI prototype employed to drive the SyRel was selected in order to guarantee safely operation at high switching frequencies especially when the FCS-MPC is performed.

The two drives share the same dc-links sourced by a dc-power supply. In such a way the energy flow recirculates from the PM to the SyRel and vice versa, with one of the machines acting as a motor and the other one as a generator, absorbing from the grid what is necessary to compensate the power losses. The SyRel motor has an absolute encoder (Tamagawa encoder) mounted on its shaft to detect the angular position signal needed to perform rotor-oriented control algorithms. For the same reason, also the

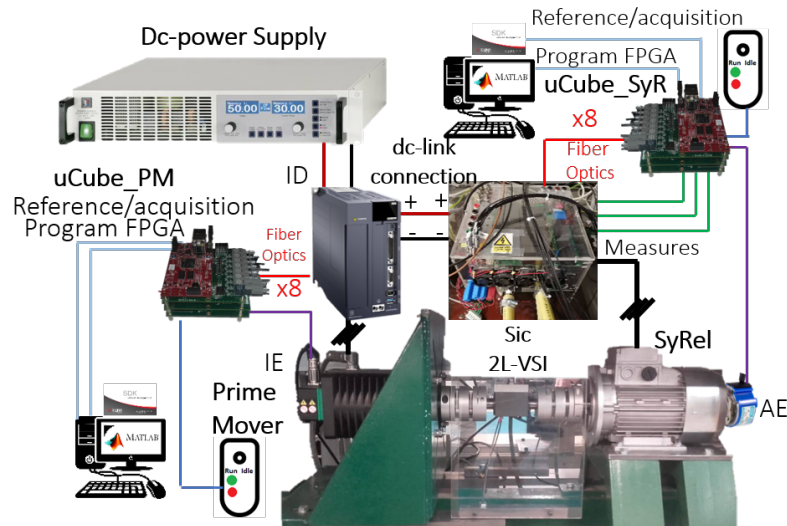


Figure A.1: Test bench configuration.

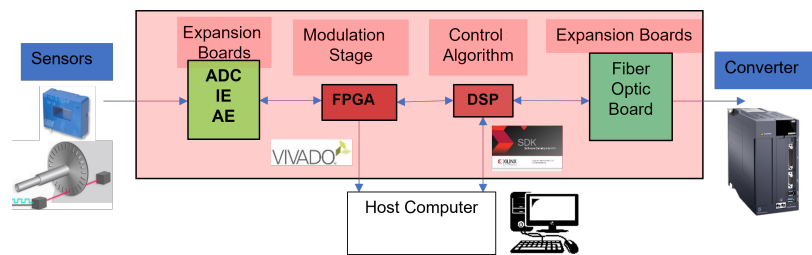


Figure A.2: Ucube control Platform.

PM servo drive incorporates an incremental encoder (IE) in its structure.

The control platform employed to control both PM and SyRel is the one introduced in [91] (Ucube) and it is based on a Microzed board from Avnet, a low-cost development board based on the Xilinx Zynq-7000 where a DSP is used in conjunction with a FPGA device. The FPGA is electrically interfaced with sensors and transceivers using a series of expansion boards: one is aimed to host 24 fiber optics channels to send the switching signal to the converter; a second board hosts 16 analog-to-digital-converters ADC, the third board is instead oriented to motor controlling applications and provides for a sin-cos resolver interface and absolute/incremental encoder interface.

A simplified scheme of the control platform used in this work is shown

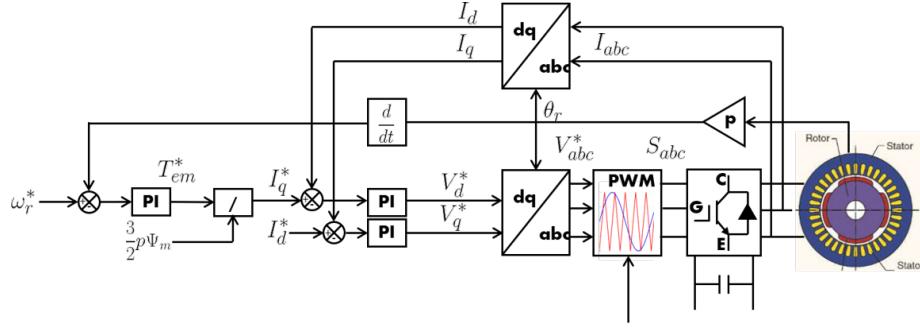


Figure A.3: PM speed control scheme.

in Fig. A.2. The FPGA is connected to Hall sensors through expansion boards aimed at converting the analog measurements (i.e., currents and voltages) to digital signals. Also, the incremental encoder (IE) and the absolute encoder (AE) signals are sent to the FPGA through expansion boards as input signals. The control algorithms have been implemented on the DSP whose output duty cycles are sent to the modulator implemented on the FPGA with a clock frequency of 200MHz. The duty cycles are then sent to the inverter through fiber optic signals to generate the actuating command for the drive. The signals are visualized and stored in Matlab in a circular buffer through a serial communication cable. The computed signals can be sent from DSP to FPGA and vice versa through real-time registers and configuration registers.

Next section is dedicated to the prime mover description, while the following section describes the control scheme for the SyRel motor.

A.1 Prime Mover Control

The block diagram to control the PM in speed control mode is represented in Fig. A.3. It is described by an outer speed loop whose torque output T_{PM}^* is entirely provided by the PM q -axis current $i_{q_{PM}}^*$, calculated through the torque constant depending on the number of pole pairs $p_{PM} = 2$ and

the permanent magnets flux $\psi_{PM} = 254.7$ Vs as

$$i_{qPM}^* = \frac{2T_{PM}^*}{p_{PM}p_{PM}}, \quad (\text{A.1})$$

while the d -axis current reference was set to zero. The PI speed controller gains are calculated by setting the natural frequency f_{PM} and the dumping ratio ξ_ω considering the pole placement method of a plant characterized by an inertia coefficient of $J_{PM} = 20.5$ kg cm² and a friction coefficient B_{PM} as follows:

$$K_{P_\omega} = (2\pi f_{PM} \xi_{PM} J_{PM}) - B_{PM} \quad (\text{A.2a})$$

$$K_{I_\omega} = (2\pi f_{PM} J_{PM})^2; \quad (\text{A.2b})$$

In the same way, the current controller gains are calculated considering the pole placement method of a first-order electrical system characterized by a stator resistance of $R_{PM} = 0.47$ Ω and an inductance $L_{PM} = 4.15$ mH. All the reported numeric values of the parameters of the PM were available in the motor manufacturer catalog.

A.2 SyRel FOC

The block diagram of the employed control algorithm is shown for a current control mode in Fig. A.4. Given the d and q current references i_d^* and i_q^* , as well as the measured d and q current components (i_d, i_q) , and the measured dc-link voltage V_{dc} , the PI controllers compute the d and q voltage references v_d^* , v_q^* , respectively. The Clarke and the Park transformation are used to compute the abc voltage references v_a^* , v_b^* and v_c^* by means of the measured rotor angle θ_r and the pole pairs p . A modulation stage based on

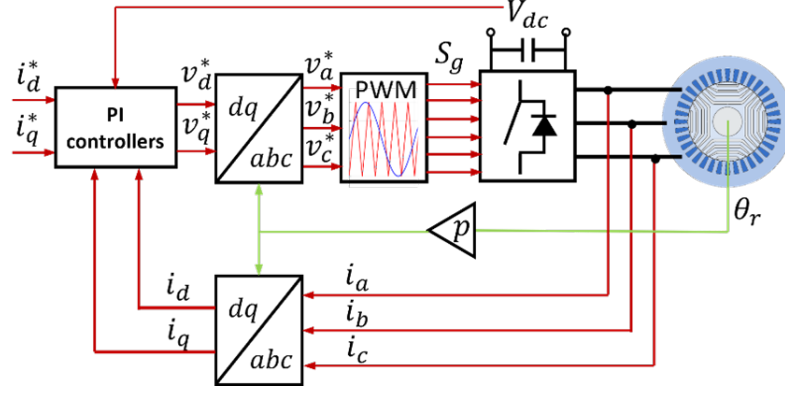


Figure A.4: Rotor-oriented FOC block diagram for SyRel motor.

Variable	Symbol	Value	Unit
Stator Resistance	R_s	3.15	Ω
Rated Torque	T_{em}	14	Nm
Rated Speed	ω_m	1500	rpm
Rated Power	P_n	2.2	kW
Rated Current	I_n	5.5	A
Rated Voltage	V_n	400	V
Pole Pairs	p	2	#

Table A.1: SyRel motor nameplate.

S-PWM synthesizes the desired voltage vector generating six gate signal S_g for the 2L-VSI power switches to control the system at the specified operating point. This control scheme was considered during the magnetic model identification procedure where the PI controller gains were tuned according to the pole placement method setting the natural frequency f_n and the dumping ratio ξ according to the following formula:

$$K_{P_d} = 2\pi f_n \xi L_d - R_s \quad , \quad K_{I_d} = (2\pi f_n L_d)^2 \quad (\text{A.3a})$$

$$K_{P_q} = 2\pi f_n \xi L_q - R_s \quad , \quad K_{I_q} = (2\pi f_n L_q)^2 \quad (\text{A.3b})$$

assuming the inductance calculated as graphically explained in (3.8) given the SyRel nameplate whose characteristics are reported in Table A.1) The closed-loop linear controller based on pole cancellation, i.e., by adopting the modulus optimum method guarantees the desired dynamic performance.

Bibliography

- [1] Hamidreza Heidari, Anton Rassõlkin, Ants Kallaste, Toomas Vaimann, Ekaterina Andriushchenko, Anouar Belahcen, and Dmitry V. Lukichev. A review of synchronous reluctance motor-drive advancements. *SUSTAINABILITY*, 13(2):1–37, January 2021.
- [2] A. Linder and R. Kennel. Model predictive control for electrical drives. In *2005 IEEE 36th Power Electronics Specialists Conference*, pages 1793–1799, 2005.
- [3] Ricardo P. Aguilera, Pablo Lezana, and Daniel E. Quevedo. Finite-control-set model predictive control with improved steady-state performance. *IEEE Transactions on Industrial Informatics*, 9(2):658–667, 2013.
- [4] Cristian F. Garcia, Cesar A. Silva, Jose R. Rodriguez, Pericle Zanchetta, and Shafiq A. Odhano. Modulated model-predictive control with optimized overmodulation. *IEEE Journal of Emerging and Selected Topics in Power Electronics*, 7(1):404–413, 2019.
- [5] Fortune Business Insight - Electric Motor Market. <https://www.fortunebusinessinsights.com/industry-reports/electric-motor-market-100752>.

- [6] Nicola Bianchi, Silverio Bolognani, Enrico Carraro, Mosè Castiello, and Emanuele Fornasiero. Electric vehicle traction based on synchronous reluctance motors. *IEEE Transactions on Industry Applications*, 52(6):4762–4769, 2016.
- [7] Shafiq Odhano Mauro Di Nardo Pericle Zanchetta Jacopo Riccio, Luca Rovere. Model-predictive control of open-end winding synchronous reluctance motor drives. In *2022 IEEE Energy Conversion Congress and Exposition (ECCE)*, 2022.
- [8] Ioana Nasui-Zah, Andreea-Mădălina Nicorici, and Claudia Martiş. Saturation and cross-saturation in synchronous reluctance machines. In *2018 International Conference and Exposition on Electrical And Power Engineering (EPE)*, pages 0347–0351, 2018.
- [9] Z. Q. Zhu, Dawei Liang, and Kan Liu. Online parameter estimation for permanent magnet synchronous machines: An overview. *IEEE Access*, 9:59059–59084, 2021.
- [10] S. A. Odhano, P. Giangrande, R. Bojoi, and C. Gerada. Self-commissioning of interior permanent magnet synchronous motor drives with high-frequency current injection. In *2013 IEEE Energy Conversion Congress and Exposition*, pages 3852–3859, 2013.
- [11] T. Senjyu, K. Kinjo, N. Urasaki, and K. Uezato. High efficiency control of synchronous reluctance motors using extended kalman filter. *IEEE Transactions on Industrial Electronics*, 50(4):726–732, 2003.
- [12] B. Nahid-Mobarakeh, F. Meibody-Tabar, and F.-M. Sargos. Mechanical sensorless control of pmsm with online estimation of stator resistance. *IEEE Transactions on Industry Applications*, 40(2):457–471, 2004.

- [13] Z.Q. Zhu, X. Zhu, P.D. Sun, and D. Howe. Estimation of winding resistance and pm flux-linkage in brushless ac machines by reduced-order extended kalman filter. In *2007 IEEE International Conference on Networking, Sensing and Control*, pages 740–745, 2007.
- [14] S. Ichikawa, M. Tomita, S. Doki, and S. Okuma. Sensorless control of permanent-magnet synchronous motors using online parameter identification based on system identification theory. *IEEE Transactions on Industrial Electronics*, 53(2):363–372, 2006.
- [15] Yukinori Inoue, Yasunori Kawaguchi, Shigeo Morimoto, and Masayuki Sanada. Performance improvement of sensorless ipmsm drives in low-speed region using online parameter identification. In *2009 IEEE Energy Conversion Congress and Exposition*, pages 1933–1938, 2009.
- [16] B. Stumberger, B. Kreca, and B. Hribernik. Determination of parameters of synchronous motor with permanent magnets from measurement of load conditions. *IEEE Transactions on Energy Conversion*, 14(4):1413–1416, 1999.
- [17] Anantaram Varatharajan, Paolo Pescetto, and Gianmario Pellegrino. Sensorless self-commissioning of synchronous reluctance machine with rotor self-locking mechanism. In *2019 IEEE Energy Conversion Congress and Exposition (ECCE)*, pages 812–817, 2019.
- [18] Marko Hinkkanen, Paolo Pescetto, Eemeli Molsa, Seppo Saarakkala, Gianmario Pellegrino, and Radu Bojoi. Sensorless self-commissioning of synchronous reluctance motors at standstill without rotor locking. *IEEE Transactions on Industry Applications*, PP:1–1, 12 2016.
- [19] Gianmario Pellegrino, Barbara Boazzo, and Thomas M. Jahns. Magnetic model self-identification for pm synchronous machine drives. In

- 2014 International Conference on Optimization of Electrical and Electronic Equipment (OPTIM)*, pages 252–260, 2014.
- [20] Z. Qu, T. Tuovinen, and M. Hinkkanen. Inclusion of magnetic saturation in dynamic models of synchronous reluctance motors. In *2012 XXth International Conference on Electrical Machines*, pages 994–1000, 2012.
- [21] Phuoc Hoa Truong, Damien Flieller, Ngac Ky Nguyen, Nguyen Bao Anh, and Nguyen Duc Hung. Inductance identification of synchronous reluctance motors using capacitor discharge method. In *2019 International Symposium on Electrical and Electronics Engineering (ISEE)*, pages 1–4, 2019.
- [22] Simon Wiedemann, Sebastian Hall, Ralph M. Kennel, and Mats Alaküla. Dynamic testing characterization of a synchronous reluctance machine. *IEEE Transactions on Industry Applications*, 54(2):1370–1378, 2018.
- [23] S. Odhano, M. Tang, A. Formentini, P. Zanchetta, and R. Bojoi. Identification of linear permanent magnet synchronous motor parameters and inverter non-linearity effects. In *2018 International Symposium on Power Electronics, Electrical Drives, Automation and Motion (SPEEDAM)*, pages 26–32, 2018.
- [24] K.M. Rahman and S. Hiti. Identification of machine parameters of a synchronous motor. In *38th IAS Annual Meeting on Conference Record of the Industry Applications Conference, 2003.*, volume 1, pages 409–415 vol.1, 2003.
- [25] Jong-Bin Im, Wonho Kim, Kwangsoo Kim, Chang-Sung Jin, Jae-Hak Choi, and Ju Lee. Inductance calculation method of synchronous reluc-

- tance motor including iron loss and cross magnetic saturation. *IEEE Transactions on Magnetics*, 45(6):2803–2806, 2009.
- [26] S. A. Odhano, P. Pescetto, H. A. A. Awan, M. Hinkkanen, G. Pellegrino, and R. Bojoi. Parameter identification and self-commissioning in ac motor drives: A technology status review. *IEEE Transactions on Power Electronics*, 34(4):3603–3614, 2019.
- [27] S. A. Odhano, R. Bojoi, S. G. Rosu, and A. Tenconi. Identification of the magnetic model of permanent magnet synchronous machines using dc-biased low frequency ac signal injection. In *2014 IEEE Energy Conversion Congress and Exposition (ECCE)*, pages 1722–1728, 2014.
- [28] L. Peretti, P. Sandulescu, and G. Zanuso. Self-commissioning of flux linkage curves of synchronous reluctance machines in quasi-standstill condition. *IET Electric Power Applications*, 9(9):642–651, 2015.
- [29] B. Stumberger, G. Stumberger, D. Dolinar, A. Hamler, and M. Trlep. Evaluation of saturation and cross-magnetization effects in interior permanent-magnet synchronous motor. *IEEE Transactions on Industry Applications*, 39(5):1264–1271, 2003.
- [30] S. Wiedemann and R. M. Kennel. Encoderless self-commissioning and identification of synchronous reluctance machines at standstill. In *2017 IEEE 26th International Symposium on Industrial Electronics (ISIE)*, pages 296–302, 2017.
- [31] Paolo Pescetto and Gianmario Pellegrino. Standstill determination of pm flux linkage based on minimum saliency tracking for pm-syr machines. In *2019 IEEE Energy Conversion Congress and Exposition (ECCE)*, pages 4888–4894, 2019.

- [32] R. Dutta and M.F. Rahman. A comparative analysis of two test methods of measuring d- and q-axes inductances of interior permanent-magnet machine. *IEEE Transactions on Magnetics*, 42(11):3712–3718, 2006.
- [33] Nicola Bedetti, Sandro Calligaro, and Roberto Petrella. Stand-still self-identification of flux characteristics for synchronous reluctance machines using novel saturation approximating function and multiple linear regression. *IEEE Transactions on Industry Applications*, 52(4):3083–3092, 2016.
- [34] Emeka Obe. Calculation of inductances and torque of an axially laminated synchronous reluctance motor. *Electric Power Applications, IET*, 4:783 – 792, 12 2010.
- [35] Arzhang Yousefi-Talouki and Gianmario Pellegrino. Sensorless direct flux vector control of synchronous reluctance motor drives in a wide speed range including standstill. pages 1167–1173, 09 2016.
- [36] Hafiz Asad Ali Awan, Marko Hinkkanen, Radu Bojoi, and Gianmario Pellegrino. Stator-flux-oriented control of synchronous motors: A systematic design procedure. *IEEE Transactions on Industry Applications*, 55(5):4811–4820, 2019.
- [37] Riccardo Antonello, Ludovico Ortombina, Fabio Tinazzi, and Mauro Zigliotto. Advanced current control of synchronous reluctance motors. In *2017 IEEE 12th International Conference on Power Electronics and Drive Systems (PEDS)*, pages 1,037–1,042, 2017.
- [38] Gilbert Hock Beng Foo and Xinan Zhang. Robust direct torque control of synchronous reluctance motor drives in the field-weakening region. *IEEE Transactions on Power Electronics*, 32(2):1289–1298, 2017.

- [39] Anshul Varshney and Bhim Singh. Direct torque controlled synchronous reluctance motor drive for pv array fed water pumping. In *2018 IEEMA Engineer Infinite Conference (eTechNxT)*, pages 1–6, 2018.
- [40] Roberto Morales-Caporal and Mario Pacas. A predictive torque control for the synchronous reluctance machine taking into account the magnetic cross saturation. *IEEE Transactions on Industrial Electronics*, 54(2):1161–1167, 2007.
- [41] Michael Saur, Francisco Ramos, Aday Perez, Dieter Gerling, and Robert D. Lorenz. Implementation of deadbeat-direct torque and flux control for synchronous reluctance machines to minimize loss each switching period. In *2016 IEEE Applied Power Electronics Conference and Exposition (APEC)*, pages 215–220, 2016.
- [42] Petros Karamanakos, Eyke Liegmann, Tobias Geyer, and Ralph Kennel. Model predictive control of power electronic systems: Methods, results, and challenges. *IEEE Open Journal of Industry Applications*, 1:95–114, 2020.
- [43] Chunyan Lai, Guodong Feng, Kaushik Mukherjee, and Narayan C. Kar. Investigations of the influence of pmsm parameter variations in optimal stator current design for torque ripple minimization. *IEEE Transactions on Energy Conversion*, 32(3):1052–1062, 2017.
- [44] Petros Karamanakos and Tobias Geyer. Guidelines for the design of finite control set model predictive controllers. *IEEE Transactions on Power Electronics*, 35(7):7434–7450, 2020.
- [45] Cheng-Kai Lin, Jen-te Yu, Yen-Shin Lai, and Hsing-Cheng Yu. Improved model-free predictive current control for synchronous reluc-

- tance motor drives. *IEEE Transactions on Industrial Electronics*, 63(6):3942–3953, 2016.
- [46] RenÉ Vargas, Ulrich Ammann, and JosÉ Rodríguez. Predictive approach to increase efficiency and reduce switching losses on matrix converters. *IEEE Transactions on Power Electronics*, 24(4):894–902, 2009.
- [47] Gionata Cimini, Daniele Bernardini, Alberto Bemporad, and Stephen Levijoki. Online model predictive torque control for permanent magnet synchronous motors. In *2015 IEEE International Conference on Industrial Technology (ICIT)*, pages 2308–2313, 2015.
- [48] L. Ortombina, E. Liegmann, P. Karamanakos, F. Tinazzi, M. Zigliotto, and R. Kennel. Constrained long-horizon direct model predictive control for synchronous reluctance motor drives. In *2018 IEEE 19th Workshop on Control and Modeling for Power Electronics (COMPEL)*, pages 1–8, 2018.
- [49] Jose Rodriguez, Marian P. Kazmierkowski, Jose R. Espinoza, Pericle Zanchetta, Haitham Abu-Rub, Hector A. Young, and Christian A. Rojas. State of the art of finite control set model predictive control in power electronics. *IEEE Transactions on Industrial Informatics*, 9(2):1003–1016, 2013.
- [50] Sören Hanke, Sebastian Peitz, Oliver Wallscheid, Joachim Böcker, and Michael Dellnitz. Finite-control-set model predictive control for a permanent magnet synchronous motor application with online least squares system identification. In *2019 IEEE International Symposium on Predictive Control of Electrical Drives and Power Electronics (PRECEDE)*, pages 1–6, 2019.

- [51] Andrea Favato, Paolo Gherardo Carlet, Francesco Toso, and Silverio Bolognani. A model predictive control for synchronous motor drive with integral action. In *IECON 2018 - 44th Annual Conference of the IEEE Industrial Electronics Society*, pages 325–330, 2018.
- [52] C. Scognamillo, A. P. Catalano, A. Borghese, M. Riccio, V. d’Alessandro, G. Breglio, A. Irace, R. N. Tripathi, A. Castellazzi, and L. Codecasa. Electrothermal modeling, simulation, and electromagnetic characterization of a 3.3 kV SiC mosfet power module. In *2021 33rd International Symposium on Power Semiconductor Devices and ICs (ISPSD)*, pages 123–126, 2021.
- [53] Alessandro Borghese, Antonio Pio Catalano, Michele Riccio, Lorenzo Codecasa, Asad Fayyaz, Vincenzo d’Alessandro, Alberto Castellazzi, Luca Maresca, Giovanni Breglio, and Andrea Irace. An efficient simulation methodology to quantify the impact of parameter fluctuations on the electrothermal behavior of multichip SiC power modules. In *Silicon Carbide and Related Materials 2018*, volume 963 of *Materials Science Forum*, pages 855–858. Trans Tech Publications Ltd, 9 2019.
- [54] Mingchen Gu, Peng Xu, Li Zhang, and Kai Sun. A sic-based t-type three-phase three-level gridtied inverter. In *2015 IEEE 10th Conference on Industrial Electronics and Applications (ICIEA)*, pages 1116–1121, 2015.
- [55] Ludovico Ortombina, Petros Karamanakos, and Mauro Zigliotto. Robustness analysis of long-horizon direct model predictive control: Induction motor drives. In *2020 IEEE 21st Workshop on Control and Modeling for Power Electronics (COMPEL)*, pages 1–8, 2020.
- [56] E. Fuentes, C. A. Silva, and R. M. Kennel. Mpc implementation of a quasi-time-optimal speed control for a PMSM drive, with inner

- modulated-fs-mpc torque control. *IEEE Transactions on Industrial Electronics*, 63(6):3897–3905, June 2016.
- [57] J. Riccio, S. A. Odhano, and P. Zanchetta. Sensorless and modulated model-predictive control for a doubly fed induction machine. In *2019 21st European Conference on Power Electronics and Applications (EPE '19 ECCE Europe)*, pages P.1–P.10, Sep. 2019.
- [58] L. Tarisciotti, J. Lei, A. Formentini, A. Trentin, P. Zanchetta, P. Wheeler, and M. Rivera. Modulated predictive control for indirect matrix converter. *IEEE Transactions on Industry Applications*, 53(5):4644–4654, 2017.
- [59] Behnam Nikmaram, Alireza Davari, Peyman Naderi, Jose Rodriguez, and Cristian Garcia. Simplified modulated model predictive control of synchronous reluctance motor. In *2020 11th Power Electronics, Drive Systems, and Technologies Conference (PEDSTC)*, pages 1–6, 2020.
- [60] Crestian Almazan Agustin, Jyun-Ting Wang, and Cheng-Kai Lin. A modulated model predictive current controller for four-switch three-phase inverter-fed SynRMs. *2019 IEEE 4th International Future Energy Electronics Conference (IFEEEC)*, pages 1–5, 2019.
- [61] Paolo Gherardo Carlet, Andrea Favato, Saverio Bolognani, and Florian Dörfler. Data-driven continuous-set predictive current control for synchronous motor drives. *IEEE Transactions on Power Electronics*, 37(6):6637–6646, 2022.
- [62] Andrea Favato, Paolo Gherardo Carlet, Francesco Toso, Riccardo Torchio, and Silverio Bolognani. Integral model predictive current control for synchronous motor drives. *IEEE Transactions on Power Electronics*, 36(11):13293–13303, 2021.

- [63] Francesco Toso, Andrea Favato, Riccardo Torchio, Piergiorgio Alotto, and Silverio Bolognani. Continuous control set model predictive current control of a microgrid-connected pwm inverter. *IEEE Transactions on Power Systems*, 36(1):415–425, 2021.
- [64] Paolo Gherardo Carlet, Francesco Toso, Andrea Favato, and Silverio Bolognani. A speed and current cascade continuous control set model predictive control architecture for synchronous motor drives. In *2019 IEEE Energy Conversion Congress and Exposition (ECCE)*, pages 5682–5688, 2019.
- [65] Andrea Favato, Francesco Toso, Paolo Gherardo Carlet, Matteo Carbonieri, and Silverio Bolognani. Fast moving horizon estimator for induction motor sensorless control. In *2019 IEEE 10th International Symposium on Sensorless Control for Electrical Drives (SLED)*, pages 1–6, 2019.
- [66] Paolo Gherardo Carlet, Andrea Favato, Francesco Toso, and Silverio Bolognani. Sensorless control of interior permanent magnet motor using a moving horizon estimator based on a linearized motor model. In *2019 IEEE 10th International Symposium on Sensorless Control for Electrical Drives (SLED)*, pages 1–6, 2019.
- [67] Xiaoguang Zhang, Liang Zhang, and Yongchang Zhang. Model predictive current control for pmsm drives with parameter robustness improvement. *IEEE Transactions on Power Electronics*, 34(2):1645–1657, 2019.
- [68] Xin Yuan, Shuo Zhang, and Chengning Zhang. Nonparametric predictive current control for pmsm. *IEEE Transactions on Power Electronics*, 35(9):9332–9341, 2020.

- [69] Ismaele De Martin, Dario Pasqualotto, Fabio Tinazzi, and Mauro Zigliotto. Model-free predictive current control of synchronous reluctance motor drives for pump applications. *Machines*, 9:217, 09 2021.
- [70] Hamidreza Heidari, Anton Rassölkin, Ants Kallaste, Toomas Vaimann, Ekaterina Andriushchenko, Anouar Belahcen, and Dmitry V. Lukichev. A review of synchronous reluctance motor-drive advancements. *Sustainability*, 13(2), 2021.
- [71] Hazem Hadla and Sérgio Cruz. Predictive stator flux and load angle control of synchronous reluctance motor drives operating in a wide speed range. *IEEE Transactions on Industrial Electronics*, 64(9):6950–6959, 2017.
- [72] Ehsan Daryabeigi, Ahmad Mirzaei, Hossein Abootorabi Zarchi, and Sadegh Vaez-Zadeh. Deviation model-based control of synchronous reluctance motor drives with reduced parameter dependency. *IEEE Transactions on Power Electronics*, 34(7):6697–6705, 2019.
- [73] Ehsan Daryabeigi, Ahmad Mirzaei, Hossein Abootorabi Zarchi, and Sadegh Vaez-zadeh. Deviation control in comparison with dtc and foc for synrm drives. In *2019 10th International Power Electronics, Drive Systems and Technologies Conference (PEDSTC)*, pages 713–717, 2019.
- [74] Salahuddin Abdul Rahman, Mohamed Zribi, and Nejib Smaoui. Synchronization of synchronous reluctance motors using the discrete sliding mode control technique. *Mathematical Problems in Engineering*, 2019:1–13, 12 2019.
- [75] Faa-Jeng Lin, Shih-Gang Chen, Ming-Shi Huang, Chia-Hui Liang, and Chen-Hao Liao. Adaptive complementary sliding mode control for

- synchronous reluctance motor with direct-axis current control. *IEEE Transactions on Industrial Electronics*, 69(1):141–150, 2022.
- [76] T.S. Radwan, Essam Eddin Rashad, M.N. Uddin, and M.A. Rahman. Fuzzy-low-based controller for synchronous reluctance motor. volume 3, pages 1731 – 1735 Vol.3, 06 2004.
- [77] E. Armando, R. I. Bojoi, P. Guglielmi, G. Pellegrino, and M. Pastorelli. Experimental identification of the magnetic model of synchronous machines. *IEEE Transactions on Industry Applications*, 49(5):2116–2125, 2013.
- [78] Anantaram Varatharajan, Sérgio Cruz, Hazem Hadla, and Fernando Briz. Predictive torque control of synrm drives with online mtpa trajectory tracking and inductances estimation. In *2017 IEEE International Electric Machines and Drives Conference (IEMDC)*, pages 1–7, 2017.
- [79] Tobias Geyer. *Model Predictive Control of High Power Converters and Industrial Drives*. 09 2016.
- [80] Petros Karamanakos, Tobias Geyer, and Ralph Kennel. On the choice of norm in finite control set model predictive control. *IEEE Transactions on Power Electronics*, 33(8):7105–7117, 2018.
- [81] Tobias Geyer. Algebraic tuning guidelines for model predictive torque and flux control. *IEEE Transactions on Industry Applications*, 54(5):4464–4475, 2018.
- [82] P. Karamanakos, E. Liegmann, T. Geyer, and R. Kennel. Model predictive control of power electronic systems: Methods, results, and challenges. *IEEE Open Journal of Industry Applications*, 1:95–114, 2020.

- [83] Bartolomeo Stellato, Tobias Geyer, and Paul J. Goulart. High-speed finite control set model predictive control for power electronics. *IEEE Transactions on Power Electronics*, 32(5):4007–4020, 2017.
- [84] Samir Kouro, Patricio Cortes, RenÉ Vargas, Ulrich Ammann, and JosÉ Rodriguez. Model predictive control—a simple and powerful method to control power converters. *IEEE Transactions on Industrial Electronics*, 56(6):1826–1838, 2009.
- [85] Jul-Ki Seok, Joohn-Sheok Kim, and Seung-Ki Sul. Overmodulation strategy for high-performance torque control. *IEEE Transactions on Power Electronics*, 13(4):786–792, 1998.
- [86] Armando Bellini, Stefano Bifaretti, and Stefano Costantini. A digital speed filter for motion control drives with a low resolution position encoder. *Automatika*, 44:67–74, 2003.
- [87] Jeevan Adhikari and S K Panda. Angle compensation based rotor position estimation for sensorless vector control of the permanent magnet synchronous motor. In *2017 IEEE Applied Power Electronics Conference and Exposition (APEC)*, pages 1906–1913, 2017.
- [88] Patricio Cortes, Samir Kouro, Bruno La Rocca, Rene Vargas, Jose Rodriguez, Jose I. Leon, Sergio Vazquez, and Leopoldo G. Franquelo. Guidelines for weighting factors design in model predictive control of power converters and drives. In *2009 IEEE International Conference on Industrial Technology*, pages 1–7, 2009.
- [89] S.M. Ferdous, Pablo Garcia, Mohammad Abdul Moin Oninda, and Md. Ashraful Hoque. Mtpa and field weakening control of synchronous reluctance motor. In *2016 9th International Conference on Electrical and Computer Engineering (ICECE)*, pages 598–601, 2016.

- [90] Giovanni Lo Calzo, Pericle Zanchetta, Chris Gerada, Alberto Gaeta, and Fabio Crescimbin. Converter topologies comparison for more electric aircrafts high speed starter/generator application. In *2015 IEEE Energy Conversion Congress and Exposition (ECCE)*, pages 3659–3666, 2015.
- [91] A. Galassini, G. Lo Calzo, A. Formentini, C. Gerada, P. Zanchetta, and A. Costabeber. uCube: Control platform for power electronics. In *2017 IEEE Workshop on Electrical Machines Design, Control and Diagnosis (WEMDCD)*, pages 216–221, 2017.